A cryogenic Strontium lattice clock

Von der QUEST-Leibniz-Forschungsschule der
Gottfried Wilhelm Leibniz Universität Hannover
zur Erlangung des Grades

Doktor der Naturwissenschaften
Dr. rer. nat.

genehmigte Dissertation
von

Dipl.-Ing. (FH) Roman Schwarz

2022

Referent	PD Dr. Christian Lisdat Physikalisch-Technische Bundesanstalt
Korreferent	Prof. Dr. Wolfgang Ertmer Leibniz Universität Hannover
	Prof. Dr. Stephan Schiller Heinrich-Heine-Universität Düsseldorf
Tag der Disputation	18.03.2022

Abstract

Optical clocks have moved to the forefront of frequency metrology. Their outstanding performances enable the exploration of new fields of research such as the search for dark matter and dark energy [1, 2], temporal drifts of the fine structure constant α [3–5], violations of the Einstein equivalence principle (EEP) [6], and new applications such as chronometric leveling [7]. State-of-the-art optical clocks outperform the current realization of the SI-unit "Second" by the ^{133}cesium fountain clocks, by two orders magnitude or more in instability and accuracy which triggers a discussion on a re-definition of the second. In 2016 the Consultative Committee for Time and Frequency (CCTF) of the International Bureau of Weights and Measures (BIPM) released a roadmap towards a re-definition of the SI second[1]. One of the requests is the characterization of the systematic uncertainty of at least three independent clocks at the level of 10^{-18}. In this work, PTB's new cryogenic strontium lattice clock, Sr3, operating on the $^1S_0 - {}^3P_0$ clock transition in neutral ^{87}Sr is described. Its systematic uncertainty has is evaluated to $2.7 \cdot 10^{-18}$ in fractional frequency units. This represents an improvement of more than a factor of 5 compared to its predecessor system Sr1 [8]. In Sr1 the dominant contribution of frequency uncertainty was about $1.4 \cdot 10^{-17}$ from the uncertainty of the black-body radiation (BBR) frequency shift. It arose from temperature gradients across the in-vacuum magnetic field coils that are placed close to the atoms. Reducing the gradients was not possible which ultimately limited the systems achievable systematic uncertainty. Sr3 features an in-vacuum dual-layer environment, the cryostat, that provides a very homogeneous temperature distribution for the atoms. This translates to a lower BBR frequency shift uncertainty as Sr1 at room temperature operation. The corresponding total systematic uncertainty for room temperature operation was evaluated to about $3.5 \cdot 10^{-18}$. Furthermore Sr3 features a closed-cycle pulse tube cooler that allows to operate the cryostat at any temperature ranging from room temperature to about 80 K to further reduce the BBR frequency shift and uncertainty where the systematic uncertainty reaches the value of $2.7 \cdot 10^{-18}$ as mentioned above.

Sr3 also features an arrangement of electrodes that allow the characterization of the dc-Stark frequency shift in three dimensional space. In this work the characterization of the electrode arrangement is described and the determination of the dc Stark shift. In Sr1 the this capability was limited to one direction that was pointing along the quantization magnetic field axis.

During clock operation of Sr1, several high-accuracy comparisons to other atomic clocks have been performed. This includes many absolute frequency measurements yielding in a new record uncertainty in the transition frequency. An absolute frequency of Sr1 of $\nu_{\mathrm{Sr1}} = 429\,228\,004\,229\,873.00(7)$Hz [8] was measured that is in agreement withe the one measured of Sr3 of $\nu_{\mathrm{Sr3}} = 429\,228\,004\,229\,872.94(19)$Hz. The statistical uncertainty the

[1] https://www.bipm.org/documents/20126/35554967/CCTF-roadmap.jpg/6338cf4c-59d6-d8ee-6cc5-eb390715b900

measurements was significantly improved by using a H-Maser as a flywheel oscillator to either extend the dataset or to bridge downtimes of the Sr-clocks [9].

Optical frequency ratio measurements between either of the two strontium clocks and the on-campus $^{171}Yb^{+}$ single-ion clock have been carried out [10] for direct determination of their frequency ratio beyond the limitation of the primary frequency standards represented by Cs fountain clocks. The ratio measurements involving Sr1 span over a period of more than seven years and more than half a year with Sr3. The measurements have also revealed that the frequency ratio of the clocks, are reproducible within their uncertainties on short time scales but exhibits unexpected large scatter in the long term. The observed variations are on the order of several 10^{-17} which is beyond any of the clocks reported systematic uncertainty. Despite an excessive search no uncontrolled frequency shifts were found.

In the near future the in-vacuum cryostat is supposed to be updated with rotatable shutters. They will allow to minimize the BBR shift uncertainty during cryogenic operation. Prospectively a BBR shift uncertainty at the low 10^{-19} level can be expected which paves the way for the system to reach a total systematic uncertainty of below $1 \cdot 10^{-18}$.

Keywords: Strontium lattice clock, frequency standard, blackbody radiation frequency shift

Publications

Roman Schwarz, Sören Dörscher, Ali Al-Masoudi, Stefan Vogt, Ye Li, Christian Lisdat
A compact and robust cooling laser system for an optical strontium lattice clock *Review of Scientific Instruments* 90, No. 2, 023109 (2019)

Stefano Origlia, Mysore Srinivas Pramod, Stephan Schiller, Yeshpal Singh, Kai Bongs, **Roman Schwarz**, Ali Al-Masoudi, Sören Dörscher, Sofia Herbers, Sebastian Häfner, Uwe Sterr, Christian Lisdat
Towards an optical clock for space: Compact, high-performance optical lattice clock based on bosonic atoms *Physical Review A* 98, 053443 (2018)

Sören Dörscher, **Roman Schwarz**, Ali Al-Masoudi, Stefan Falke, Uwe Sterr, Christian Lisdat
Lattice-induced photon scattering in an optical lattice clock *Physical Review A* 97, 063419 (2018)

Moustafa Abdel-Hafiz, Piotr Ablewski, Ali Al-Masoudi, Héctor Álvarez Martínez, Petr Balling, Geoffrey Barwood, Erik Benkler, Marcin Bober, Mateusz Borkowski, William Bowden, Roman Ciuryło, Hubert Cybulski, Alexandre Didier, Miroslav Doležal, Sören Dörscher, Stephan Falke, Rachel M. Godun, Ramiz Hamid, Ian R. Hill, Richard Hobson, Nils Huntemann,Yann Le Coq, Rodolphe Le Targat, Thomas Legero, Thomas Lindvall, Christian Lisdat, Jérôme Lodewyck, Helen S. Margolis, Tanja E. Mehlstäubler, Ekkehard Peik, Lennart Pelzer, Marco Pizzocaro, Benjamin Rauf, Antoine Rolland, Nils Scharnhorst, Marco Schioppo, Piet O. Schmidt, **Roman Schwarz**, Çağrı Şenel, Nicolas Spethmann, Uwe Sterr, Christian Tamm, Jan W. Thomsen, Alvise Vianello, Michał Zawada
Guidelines for developing optical clocks with 10^{-18} *fractional frequency uncertainty* (2019)

Benjamin M. Roberts, Pacome Delva, Ali Al-Masoudi, Anne Amy-Klein, C. Baerentsen, C. F. A. Baynham, Erik Benkler, Slawomir Bilicki, Sebastien Bize, William Bowden, J. Calvert, Valentin Cambier, Etienne Cantin, Elizabeth Anne Curtis, Soren Dorscher, Maxime Favier, Florian Frank, Patrick Gill, R. M. Godun, Gesine Grosche, Changlei Guo, Aurelien Hees, Ian Robert Hill, Richard Hobson, Nils Huntemann, J. Kronjager, Sebastian Koke, Alexander Kuhl, Richard Lange, Thomas Legero, Burghard Lipphardt, Christian Lisdat, Jerome Lodewyck, Olivier Lopez, Helen S. Margolis, H. Alvarez-Martinez, Frederic Meynadier, Filip Ozimek, Ekkehard Peik, P-E Pottie, Nicolas Quintin, Christian Sanner, Luigi De Sarlo, Marco Schioppo, **Roman Schwarz**, Alissa Silva, Uwe Sterr, Christian Tamm, Rodolphe Le Targat, Philip Tuckey, Gregoire Vallet, Thomas Waterholter, Dan Xu, Peter Wolf
Search for transient variations of the fine structure constant and dark matter using fiber-linked optical atomic clocks *New Journal of Physics*, 22, 093010 (2020)

Roman Schwarz, Sören Dörscher, Ali Al-Masoudi, Erik Benkler, Thomas Legero, Uwe Sterr, Stefan Weyers, Johannes Rahm, Burghard Lipphardt, Christian Lisdat
Long term measurement of the ^{87}Sr clock frequency at the limit of primary Cs clocks *Physical Review Research*, 2, 033242 (2020)

Sören Dörscher, Ali Al-Masoudi, Marcin Bober, **Roman Schwarz**, Richard Hobson, Uwe Sterr, Christian Lisdat
Dynamic decoupling of laser phase noise in compound atomic clocks *Communications Physics*, 3 185 (2020)

Sören Dörscher, Nils Huntemann, **Roman Schwarz**, Richard Lange, Erik Benkler, Burghard Lipphardt, Uwe Sterr, Ekkehard Peik, Christian Lisdat
Optical frequency ratio of a $^{171}Yb^{+}$ single-ion clock and a ^{87}Sr lattice clock *Metrologia*, 58, 015005 (2021)

Marco Schioppo, Jochen Kronjäger, Alissa Silva, Riley Ilieva, Jake Paterson, Charles Baynham, William Bowden, Ian Hill, Richard Hobson, Alvise Vianello, Miguel Dovale Álvarez, Ross Williams, Giuseppe Marra, Helen Margolis, Anne AMY, Olivier Lopez, Etienne Cantin, Héctor Álvarez-Martínez, Rodolphe Le Targat, Paul-Eric Pottie, Nicolas Quintin, Thomas Legero, Sebastian Häfner, Uwe Sterr, **Roman Schwarz**, Sören Dörscher, Christian Lisdat, Sebastian Koke, Alexander Kuhl, Thomas Waterholter, Erik Benkler, Gesine Grosche
Comparing ultrastable lasers at 7×10^{-17} fractional frequency instability through a 2220 km *optical fibre network* *Nature Communications*, Vol. 12, No. 1, p. 2402 (2021)

Contents

1. Introduction

Science, the final frontier. Here I report on recent activities in the field of optical lattice clocks. An ever ongoing mission to explore the boundaries of physics and create knowledge. To seek out strange effects and describe new fields of research. To boldly measure what has not been measured before.

In 1955, the first atomic frequency standard based on cesium was presented [11]. A specific atomic transition represent a universal frequency reference for the same species since they are all identical. This makes clocks based on atomic transitions excellent candidates for the definition of the SI unit second. Roughly a decade later, in 1967 the definition of the SI second was changed from the ephemeris time to the microwave transition in ^{133}Cs. Here the transition between the two hyperfine ground state levels $(6s)^2\mathrm{S}_{1/2},\ F = 3 - F' = 4$ had been defined to 9 192 631 770 periods per second. Since then the performance of Cs clocks has greatly improved over the last decades now demonstrating a systematic uncertainty of app. $1 \cdot 10^{-16}$ [12,13]. Today, PTB is operating four primary frequency standards based on the cesium fountain clocks CSF1 and CFS2 and two beam clocks CS1 and CS2 that contribute regular to the International Atomic Time (TAI).

Comparing the systematic uncertainty of those systems to clocks that rely on optical transitions the performance of the best cesium fountain clocks is surpassed by two orders of magnitude as seen in Fig. 1.1. Indeed, this sparks a discussion on a redefinition of the SI unit second once again. In 2006, the International Bureau of Weights and Measures (BIPM) introduces a list of frequencies recommended for secondary representations of the Second including the rubidium microwave transition and several optical transitions such as the $^1\mathrm{S}_0 - {}^3\mathrm{P}_0$ transition in neutral ^{87}Sr. In 2018 its resonance frequency was recommended to 429 228 004 229 873.0(2) Hz [14].

Compared to cesium fountain clocks, optical clocks achieve significant larger Q factors which is $Q = \frac{\nu_0}{\Delta\nu_{FWHM}}$ its absolute transition frequency divided by the full with at half maximum (FWHM) linewidth. The Allan deviation that describes a clocks instability is proportional to $1/Q$ hence a greater Q-facter grants greater stability of the frequency measurement. As an example, the averaging time required for a cesium fountain clock to reach a statistical uncertainty of $2 \cdot 10^{-16}$ [13] is about 3 hours, for a typical optical lattice clock it is just a matter of minutes to reach a statistical uncertainty in the 10^{-17} range.

Together with instability, a clocks accuracy represents, the most important property in the performance of a frequency standard. In atomic clocks, the environment surrounding the atoms can shift the atoms clock transition frequency. Characterization of the frequency shifts is crucial to determine the clocks total frequency shift and uncertainty. All known frequency shift contributions are listed in the clocks uncertainty budget.

High performance frequency standards are required in numerous fields of research and applications such as the search for new physics beyond the standard model, relativistic geodesy, timekeeping or global positioning.

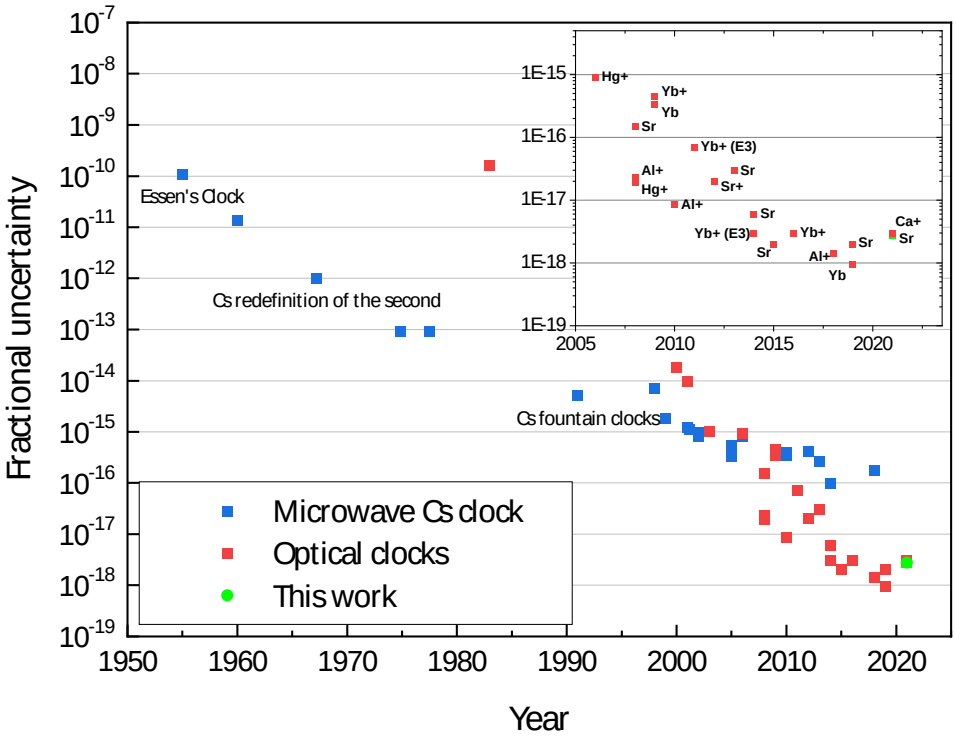

Figure 1.1.: Evolution of accuracy of optical clocks vs. microwave clocks. Recently the uncertainty of optical clocks surpassed those of microwave standards by two orders of magnitude raising discussion on a redefinition of the SI-unit Second. Sources can be found in the appendix in Tab. A.2.

1.1. Outline of the thesis

This manuscript is subject of the description and characterization of the new lattice clock based on neutral ^{87}Sr denoted as Sr3. The new apparatus aimed for a significant reduction of the black-body radiation (BBR) induced frequency shift, which poses the leading uncertainty contribution in room temperature operated Sr lattice clocks. This is achieved by two main features. First, a good thermal homogeneity and, secondly its capability of operating at cryogenic temperatures. Apart from the characterization of Sr3, several measurement results performed with Sr1 are also included in this manuscript. This applies to the results discussed in Chapter 5. The measurements of the absolute frequency and the frequency ratio measurements (chapter 6 and 7) include results mainly obtained with Sr1 but also first results that were obtained with Sr3.

Chapter 2, principle of an optical lattice clock

Chapter 2 describes the principle of clock operation and techniques required such as laser cooling, the principle of a magneto optical trap (MOT) and trapping in an optical lattice. Further measurement techniques to gain information on atomic properties such as their temperature are discussed. The chapter continues with the main characteristics of an optical clock, its accuracy and stability. A description of systematic effects that cause frequency shifts on the clock transition is given as well as a brief overview on the factors that influence clock stability.

Chapter 3, the new cryogenic Sr lattice clock Sr3

The setup of the new Sr3 system and the first characterization measurements performed with it are described in this chapter. It gives an overview on the new vacuum system, optical beam delivery and several other components required to operate the clock. The chapter continues with focus on the key components that minimizes the BBR frequency shift uncertainty such as the cryostat dual layer design, the temperature acquisition and its feature to be operated at cryogenics temperatures. Furthermore, the influence of the missing atomic beam shutters and the hot atomic oven on the BBR shift uncertainty

is discussed. An additional new feature that its predecessor Sr1 was lacking is the three dimensional characterization of the residual electric field causing a dc Stark frequency shift. The determination of the residual electric fields magnitude and the frequency shift experienced by the atoms is described as well as a detailed derivation of the uncertainty thereof. The chapter finalizes with in the presentation of the evaluation of the relevant systematic effects and ends in a preliminary uncertainty budget of Sr3.

Chapter 4, robust laser breadboards

To reduce complexity and improve reliability of the optical beam delivery system for efficient operation of the red MOT in ^{87}Sr, a simplified and more robust approach of generating the required frequencies is presented in this chapter. The relevant transition frequencies are now addressed by sideband generation in a fiber coupled electro-optic modulator (EOM) and amplified by a tapered amplifier (TA). The overall optical system is less complex, more compact and extremely robust compared to the previous system.

Chapter 5, lattice induced photon scattering

The interrogating laser systems become more and more stable thanks to the evolution the pre-stablizing optical resonators enabling longer interrogation times with the atomic reference. This raises the question of effects limiting in the duration of the probing time. In this chapter the investigation of photon scattering due to the optical lattice is described that opens a loss mechanism for atoms prepared in the $^3P_0$ upper clock state to end up in the $^1S_0$ ground state. Its effect and possible limitations on lattice clocks are investigated. From the characterization measurements inferred the lifetime of the $^3P_0$ state.

Chapter 6, absolute frequency measurement

This chapter describes the measurement of the $^1S_0 - ^3P_0$ absolute transition frequency. Over a time of three years a series of 43 individual measurements have been performed between between Sr1 and our local primary cesium fountain clocks CSF1 and CSF2. The

measured transition frequency is accurate to the limit ot he current realization of the unit hertz with a fractional uncertainty of $1.5 \cdot 10^{-16}$. To date this poses the most accurate determination of the clock transition frequency of neutral ^{87}Sr. Additionally, first results of similar measurements between the fountain clocks and the new Sr3 clock are presented.

Chapter 7, Yb^+/Sr optical frequency ratio

Direct comparisons of optical frequency ratios allow to surpass the limitation of the current realization of the unit hertz. In this chapter long term measurements of the frequency ratio of PTB's ^{87}Sr1 lattice clock and $^{171}Yb^+$ single ion clock are described. First preliminary frequency ratio measurements between Sr3 and the Yb^+ clock are presented in addition.

Chapter 8, Summary and outlook

The manuscript finalizes by giving a summary of the work and main improvements but also addresses current issues e.g. on the theoretical lattice lightshift model that presently suffers from a contradiction on the coefficients treating higher order shift contributions. With an outlook on how the systematic uncertainty of Sr3 can be improved further in the future the manuscript ends.

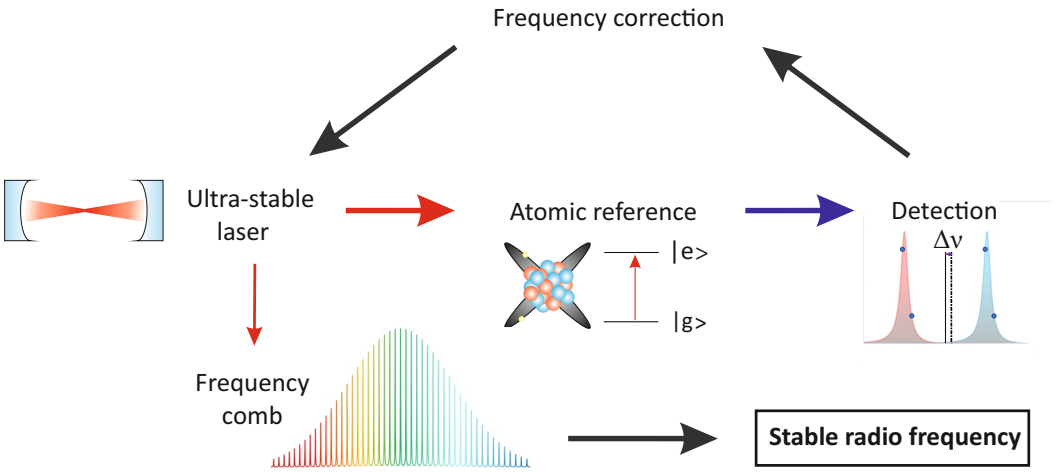

Figure 1.2.: Principle of optical clock operation. The interrogation laser system is pre-stabilized to an ultra stable reference cavity. It probes the atomic clock transition and its frequency is corrected towards resonance by an electronic feedback loop. A frequency output, stabilized to an atomic reference is achieved. Via an optical frequency comb the optical frequency can be scaled down into the radio frequency domain which allows processing by RF-electronics.

1.2. Principle of an optical atomic clock

An ordinary wristwatch is one of the most widespread clocks. Its operating principle is to count the periods of its internal quartz oscillator that operates typically at a frequency of 32 768 Hz. Then the displayed time is incremented by one second. The quality factor (Q factor) of oscillator is given by the ratio of the transition frequency ν_0 to the line width $\Delta\nu$. Quartz oscillators in watches typically reach Q = 10^4 and a frequency uncertainty of about $1 \cdot 10^{-5}$ in fractional frequency units. The same operating principle holds true for atomic clocks. Cs-fountain clocks reach Q factors of up to $Q_{CSF} \approx 10^{10}$. They are excellent oscillators for applications such as timekeeping. Optical clocks reach lower fractional uncertainties in part due to their higher transition frequencies. They can reach Q factors of more than $Q_{OC} = 10^{14}$ which is one reason why these clocks are in discussion of realizing a future definition of the second.

To probe the atomic transition a pre-stabilized interrogation laser system is typically required to make use of narrow atomic transitions. Tuneable extended cavity diode lasers

(ECDL) have become favorable since they are cheap and can be manufactured to match nearly every atomic transition frequency[2]. A common way of pre-stabilization is locking the laser's output frequency to a stable reference cavity with the Pound–Drever–Hall [15] technique. Modern cavities are based on spacer material made from ultra low expansion glass (ULE) [16] or crystalline silicon [17]. The pre-stabilized laser interrogates an atomic ensemble that has undergone several steps of preparation. In the case of an optical lattice clock based on ^{87}Sr, the ensemble requires two stages of laser cooling (Sec. 2.1) in magneto optical traps with subsequent trapping in the optical lattice (Sec. 2.2) followed by a state preparation. For spectroscopy, a Rabi π-pulse interacts with the atoms and subsequent state detection (Sec. 2.5) determines the ensembles excitation probability. From that an error signal is derived and fed back to the control loop to correct the clock laser frequency towards the atomic resonance. This loop locks the interrogating laser to the universal transition frequency of the atom which makes the setup represent an optical frequency standard.

Unfortunately, the oscillations of optical frequencies are too fast to be processed by state of the art electronic devices. Therefore, they are converted into the microwave regime via an optical frequency comb. The result is stable radio frequency (RF) output traceable to a universal atomic reference. Frequency combs can also be used to bridge large gaps in frequency e.g. between pre-stabilization systems at wavelengths other than the required interrogating laser wavelength (Sec. 3.3). For example, it allows stability transfer from the ultrastable cryogenic silicon resonator at 1542 nm to the strontium clock laser at 698 nm. Here the comb acts as a transfer oscillator [18,19] where its noise is rejected. The most relevant properties describing clock performance are their systematic uncertainty and instability[3]. The systematic uncertainty describes how well the systematic frequency shifts $\Delta\nu_{sys}$ from the unperturbed clock transition frequency ν_0 are known. The output frequency of a clock ν_{clock} can be described by

$$\nu_{clock}(t) = \nu_0 + \Delta\nu_{sys} + \Delta\nu(t) \tag{1.1}$$

Systematic frequency shifts $\Delta\nu_{sys}$ can be caused by many effects such as the black-body

[2] In some cases laser diodes cannot provide atomic resonance frequencies directly e.g. when the transition is in the UV which requires frequency conversion.

[3] In this manuscript, the uncertainties from Type A and B evaluations [20] are referred to as statistical and systematic uncertainties, respectively.

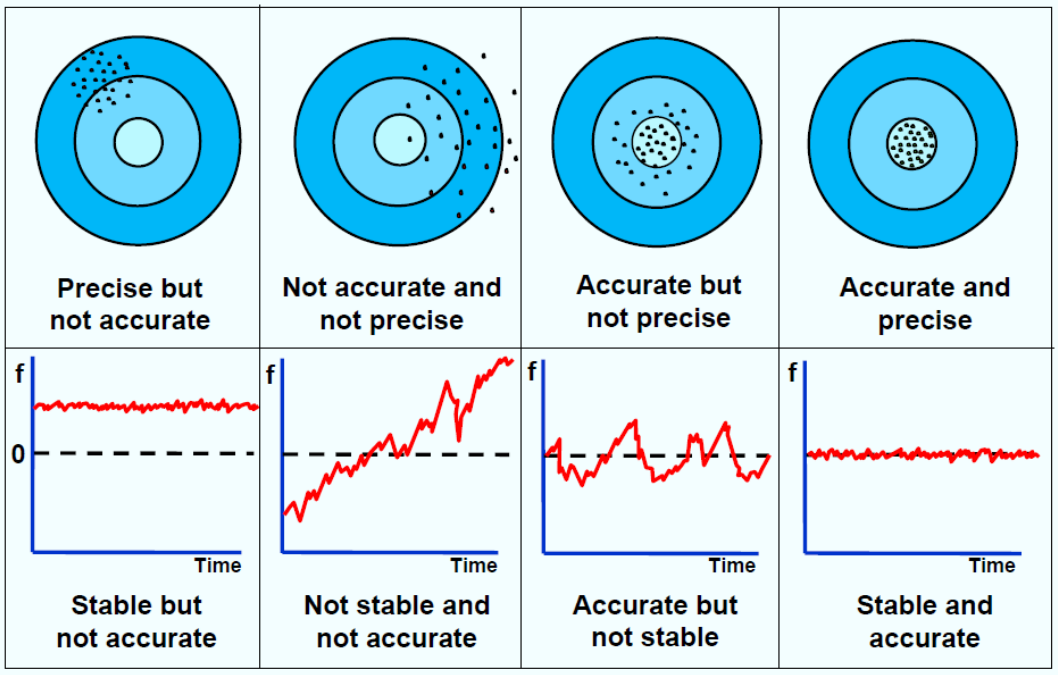

Figure 1.3.: The main properties of an oscillator are described by its accuracy and instability (also referred to as precision) of an oscillator. Desirable is an accurate and stable output frequency. Graph taken from [23].

radiation (BBR), residual electric fields, stray magnetic fields and others described in Sec. 2.6. The performed measurements to characterize the total frequency shift and uncertainty of Sr3 are found in Sec. 3.5. The frequency corrections due to all known systematic effects applied to the transition frequency are listed in the clocks uncertainty budget. The uncertainty budget is a clocks unique data-sheet which is essential for the interpretation of its frequency output and when comparing its transition frequency to other clocks e.g. by frequency ratio measurements as described in Sec. 7. The statistical noise $\Delta\nu(t)$ of a measurement is typically reduced by averaging, where Allan deviation (ADEV) [21, 22] is used to inspect the noise characteristics and estimate the statistical uncertainty. For white frequency noise, which is common in atomic clocks, the ADEV is proportional to $1/\sqrt{\tau}$ where τ is the time of averaging. The output of a clock is desired to be stable and accurate. In Fig. 1.3 the differences of the two properties can be seen taken an example by a marksman and his or her shooting results on a target.

Isotope	Natural abundance	Nuclear Spin
^{84}Sr	0.56 %	0
^{86}Sr	9.86 %	0
^{87}Sr	7.00 %	9/2
^{88}Sr	82.58 %	0

Table 1.1.: Natural abundance of stable Sr isotopes

1.3. Strontium as clock atom

The first element proposed by Hidetoshi Katori for operation in an optical lattice clock was the alkaline-earth element strontium [24]. Till now it has become the most used element in optical atomic clocks. Among the alkaline-earth and alkaline-earth-like elements their electronic configuration is similar to each other and so are their atomic properties which is one of the reasons why also magnesium and calcium are potential species for use in optical clocks. All alkaline-earth elements have a closed outer electron shell. The two valence electrons in strontium, form the outer $5s^2$ closed shell that allow singlet and triplet spin states. Three of the four stable isotopes of strontium (Tab. 1.1) are bosons and one is a fermion. ^{87}Sr and ^{88}Sr are commonly used in optical clocks. This work concentrates on ^{87}Sr with its relevant energy levels and optical transitions depicted in Fig. 1.4.

The $(5s^2)\ ^1\mathrm{S}_0 - (5s5p)\ ^1\mathrm{P}_1$ singlet transition at 461 nm is used for Zeeman slowing and the first cooling stage (Sec. 2.1). The $^1\mathrm{S}_0 - {}^3\mathrm{P}_1$ intercombination transition at 689 nm is spin forbidden according to the dipole selection rules. But spin-orbit coupling causes a finite linewidth of app. 7.5 kHz. The clock transition at 698 nm, however, is doubly forbidden due to $\Delta S = 1$ and $J = 0 - J' = 0$. Hyperfine interaction couples the nuclear spin I and the total electronic angular momentum J, where the total angular momentum quantum number $F \neq 0$ for the relevant clock states in ^{87}Sr. The $^3\mathrm{P}_0$ state experiences a small admixture from the fine structure $^3\mathrm{P}_1$ state which results in a non-zero dipole matrix element for the $^1\mathrm{S}_0 - {}^3\mathrm{P}_0$ transition. Its line width was recently measured by [25] to a value of 1.35 (3) mHz. Additionally, the $^3\mathrm{P}_0$ ($F = 9/2$) state splits into ten magnetic substates ($m_F = -9/2... + 9/2$).

In contrast, ^{88}Sr is lacking nuclear spin which remains the clock transition completely forbidden. Nevertheless there are techniques to induce the required mixing e.g.

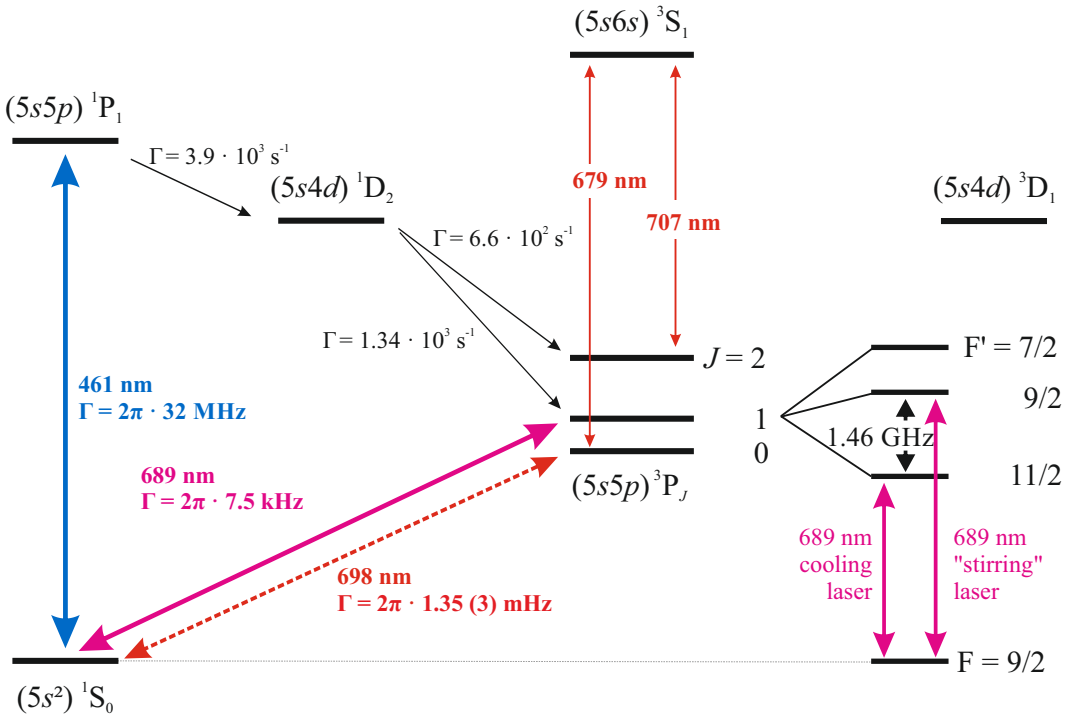

Figure 1.4.: Energy level diagram in strontium. Shown are the relevant transitions for cooling, repumping and clock operation with their associated wavelengths and linewidths. Spectral data is taken from [26]. The most accurate lifetime measurement of the clock transition today was published by [25].

by an external magnetic field [27]. Although it is challenging to control the probe light-shift uncertainty, a ^{88}Sr lattice clock with a systematic uncertainty of $2 \cdot 10^{-17}$ has been demonstrated recently [28].

2. Strontium optical lattice clock

Strontium is the most widespread clock atom used in an optical lattice clock. As seen already, the transitions relevant for clock operation (cooling, trapping etc.) are available in commercial, cost efficient diode lasers or Titanium Sapphire (Ti:Sa) lasers. The following chapter will describe relevant procedures for preparing the atoms for spectroscopy and gives a detailed introduction on characterization methods on atomic properties such as sideband spectroscopy. Furthermore the systematic effects perturbing the clock transition frequency are discussed. The chapter closes in describing another important property of a clock, its stability.

2.1. Laser cooling and MOT operation

Spectroscopy of a free atom is subject to the Doppler effect and photon recoil due to the atomic motion and momentum of the photon. This causes a frequency shift proportional to the velocity of the atom, which may lead to spectral broadening in combination with the velocity distribution of the atomic ensemble, and the recoil frequency shift. Due to the frequency dependence, one must overcome these effects in order to benefit from the higher frequency of an optical transition in an atomic clock. In single ion clocks this has been done by a strong confining potential for decades. For neutral atoms, the concept of optical lattice clocks was first proposed by the group of Katori in Tokyo [24], recognizing the existence of so called "magic wavelength" at which the effect of the strongly confining optical potential on the clock transition frequency cancels. An optical lattice is hereby approximating a harmonic potential formed by a standing wave pattern. If the confinement of the atom is strong enough so that its spacial extend is smaller than the wavelenght of the spectroscopy laser they are trapped in the so-called Lamb-Dicke regime (Sec. 2.4). Here, the atoms internal states and its motional states are sufficiently

decoupled from each other. The increase in momentum when absorbing a photon (e.g. from the clock laser) does not apply to the atoms but is absorbed from the lattice. Changes of the motional quantum number are strongly suppressed. The narrow linewidth of the $^1S_0 - {}^3P_0$ clock transition in strontium gives access to resolve the first order sidebands from the carrier transition. Sideband spectroscopy (Sec. 2.3) is a powerful tool to gather information on the residual atomic motion which is required for the evaluation of the lattice lightshift (Sec. 2.6.3).

To make use of such favorable conditions in an optical lattice trap the atoms need to be cooled and trapped into the optical lattice first. The next sections will introduce the relevant steps from a free atom to laser cooling and trapping in a potential created by an optical lattice.

2.1.1. Zeeman slowing

As source of atoms an atomic oven is commonly used at a temperature of typically several hundred °C. It produces a beam of hot atoms of temperature T with corresponding velocity v_0. The most probable velocity in a Maxwell-Boltzmann distribution is

$$v_0(T) = \sqrt{\frac{3k_BT}{m}} \tag{2.1}$$

with k_B the Boltzmann constant and m the atomic mass. Typically, v_0 is in the order of several hundred of m/s which is well above the velocity capture range of a magneto-optical trap (MOT) in common Sr lattice clocks. To efficiently capture atoms in the first stage MOT they must be decelerated. A common way of doing so is by making use of the radiation pressure force an atom experiences when absorbing a photon. Absorbing a photon from a resonant laser beam counter propagating to the atoms' motion transfers the photon moment of $\hbar k$ to the atom. The subsequent spontaneous emissions is completely random in direction which on average transfers momentum to the atom opposite to its traveling direction leading to a deceleration. After a certain deceleration the atoms will be no longer in resonance with the laser beam, that is typically kept constant in its frequency, due to the reduction of the Doppler effect. An external magnetic field that introduces a frequency shift due to the Zeeman effect can be tailored such that the Doppler frequency shift is compensated. This enables to fulfill the resonance condition over distances of

commonly a few tens of cm. Such an arrangement is called Zeeman slower. It offers efficient deceleration to final velocities at the MOT's capture velocity. A Zeeman slower is a well established tool in strontium lattice clocks [28–30].

The force experienced by the atoms can be written as in [31]

$$\vec{F} = \hbar \vec{k} \gamma_p \tag{2.2}$$

with $\vec{k}$ the wave vector of the incident light and γ_p the total scattering rate that is equal to

$$\gamma_p = \frac{s_0 \Gamma/2}{1 + s_0 + \left[2\left(\Delta_L + \omega_D\right)/\Gamma\right]^2} \tag{2.3}$$

Here Γ is the transition linewidth, Δ_L the laser frequency detuning from resonance at rest, ω_D the Doppler frequency shift. The saturation parameter $s_0 = I/I_s$ is given by the ratio of the light beam intensity I to the transitions saturation intensity I_s. For the ${}^1\mathrm{S}_0 - {}^1\mathrm{P}_1$ transition where the slower is operated $I_s \approx 43\,\mathrm{mW/cm^2}$. The transitions large scattering rate of approx. $2 \cdot 10^8\ \mathrm{s}^{-1}$ allows efficient deceleration over a length of typical just a few tens of cm.

The velocity dependent frequency shift due to the linear Zeeman effect in a magnetic field $B(z)$ is given by

$$\Delta_{\mathrm{eff}}(z) = \Delta_L + kv(z) - \mu' B(z)/\hbar \tag{2.4}$$

with $\mu' B(z)$ the position dependent linear Zeeman frequency shift, $\mu' = (g_e m_e - g_g m_g)\mu_B$ the transition's magnetic moment with $g_{e,g}$, the Landé g-factors of ground and excited state, $m_{e,g}$ the magnetic quantum numbers and μ_B the Bohr magneton. For a constant laser frequency detuning Δ_L the magnetic field and the atoms velocity are related by

$$\mu' B(z)/\hbar = kv(z) + \mu' B_{\mathrm{off}}/\hbar \tag{2.5}$$

The generation of the Doppler shift compensating magnetic field is commonly created by a tapered solenoid or by commercially available permanent magnets [29, 30, 32, 33].

In general two different magnetic field orientations relative to the atomic beam are possible. A longitudinal magnetic field orientation requires circular polarized light of the laser beam, whereas the transverse one requires linear polarization aligned orthogonal to the magnetic field direction. The linear polarization of a transverse Zeeman slower is decomposed into $\sigma^{\pm}$ light where only one of the two circularities can be resonant. This means a 50% loss of optical power and poses a significant drawback when optical power is limited. In Sr3 a longitudinal configuration is used which is coil based. It is descried in Sec. 3.1.6.

2.1.2. Trapping in a magneto-optical trap (MOT)

To further cool the atoms they are trapped in the first of two stages of a magneto-optical trap (MOT). The first stage is operated at the $^1S_0 - {}^1P_1$ singlet transition at around 461 nm. Subsequent the atoms are further cooled by the second stage operated on the $^1S_0 - {}^3P_1$ transition at around 689 nm.

The lowest achievable temperature[4] is given by the Doppler limit

$$T_{Doppler} = \frac{\hbar\Gamma}{2k_B} \tag{2.6}$$

so it becomes obvious that cooling on narrow transitions leads to lower achievable temperatures. The first stage MOT operated on the $^1S_0 - {}^1P_1$ transition (commonly referred to as the blue MOT) captures the atoms decelerated by the Zeeman slower and cools them to a temperature in the low mK range. The principle of a MOT is well known and described in various sources such as [31]. A detailed description on the MOT dynamics is beyond the scope of this work. Nevertheless it will briefly be discussed the particular case of ^{87}Sr where necessary. The $^1S_0 - {}^1P_1$ transition is not a perfectly closed cycle transition due to a loss channel into the long living $^3P_2$ state of the triplet system (Fig. 1.4). To regain these atoms for the cooling cycle two repumpers continuously redistribute the population by addressing the $^3P_2 - {}^3S_1$ and $^3P_0 - {}^3S_1$ transition. This

[4] There are techniques to cool the atoms below the Doppler limit but are not applied in Sr3 which is why a description of them is beyond the scope of this work.

enables the atoms to reach the $^1S_0$ ground state via the $^1\mathrm{S}_0 - {}^3\mathrm{P}_1$ transition and enhances the blue MOT lifetime and the number of atoms captured up to a factor of ten.

The second stage MOT operated on the narrow $^1\mathrm{S}_0, F = 9/2 - {}^3\mathrm{P}_1, F' = 11/2$ intercombination line at 689 nm reduces the temperature of the atoms even further to typically a few µK. In the particular case of ^{87}Sr it is separated into the so called "broadband" and "single-frequency phase" for maximum trapping efficiency into the optical lattice.

The velocity of the atoms after cooling them in the blue MOT still causes a frequency broadening of the transition due to the Doppler effect of about 1 MHz. In contrast, the $^1\mathrm{S}_0 - {}^3\mathrm{P}_1$ transition only has a linewidth of about 7.5 kHz. To cover the Doppler broadened spectrum during the broadband phase, the frequency of the 689 nm laser is modulated with a modulation frequency of about 1 MHz and a modulation depth of approx. 40 kHz.

In the single frequency phase, the frequency modulation is switched off, also the optical power is reduced. Another specialty of the red MOT in ^{87}Sr is the additional laser resonant with the $^1\mathrm{S}_0, F = 9/2 - {}^3\mathrm{P}_1, F' = 9/2$ transition that is superimposed to the MOT beams [34]. Due to the large difference of the Landé g-factor of ground and excited state the cooling laser cannot address all m_F sublevels. Due to the MOTs spatial dynamics of the m_F sublevels atoms will at some time end in a non-resonant state and can escape from the trap. The population dynamics among the m_F magnetic sublevels of the closed cycle cooling transition is well described in [35] and not discussed here in detail. The stirring laser continuously redistributes the population among the sublevels such that atoms do not remain in in-addressable states. The stirring laser concept was developed in [36]. It is to mentioned that the $^3\mathrm{P}_1, F' = 9/2 - F' = 11/2$ frequency splitting is approx. 1.46 GHz which can be challenging to bridge. One way is based on an amplified external cavity diode laser (ECDL) and the creation of sideband in an electro-optical phase modulater (EOM) near the $F' = 9/2 - F' = 11/2$ frequency splitting is described in this work in Chapter 4.

2.2. Trapping in the optical lattice

The optical lattice is an optical standing wave. Due to the ac-Stark effect the atoms experience a series of potential wells with a spacing of $\lambda_{lat}/2$ which is half the lattice

wavelength. Depending on the lattice wavelength the polarizability of the clock states is either positive (often referred to as red detuned) or negative (blue detuned). The atoms are trapped at the anti nodes of the standing wave in a red detuned lattice and in the nodes in a blue detuned lattice. This work will focus on the description of a red detuned lattice. More information on blue detuned lattices can found in [37, 38]. After the two stage cooling process the atoms reached a temperature of typically a few µK. The potential the lattice creates in our experiment is typically in the order of $U/k_B = 25\,\mu\text{K}$. Atoms with a lower temperature cannot leave the potential and are trapped.

Following the description by [39], the optical dipole potential near the lattice waist of a vertical lattice propagating along the z-axis is typically given by

$$U(z,r) = -U_0 \cos^2(kz) e^{-2\rho^2/w_0^2} \tag{2.7}$$

where $\rho = \sqrt{x^2+y^2}$ denotes the distance from the optical axis and w_0 its $1/e^2$ waist radius.

The lattice potential depth U_0 in Eq. 2.7 is typically given in units of the lattice recoil energy $E_{\text{rec}} = h\nu_{\text{rec}} = h^2/2m\lambda_{lat}^2$. It describes the recoil energy that the atoms experiences when absorbing one photon of the lattice light. For ^{87}Sr and a lattice operated near the magic wavelength of $\lambda_{lat} = 813\,\text{nm}$ and $\nu_{rec} \approx 3.47\,\text{kHz}$.

To describe the potential including the effect of gravity which is more realistic for an experiment placed on Earth, the potential described by Eq. 2.7 is modified with the term $mgz\cos(\theta)$ leading to

$$U(z,r) = -U_0 \cos^2(kz) e^{-2\rho^2/w_0^2} + mgz\cos(\theta) \tag{2.8}$$

Here m is the mass of the particle ($m(^{87}\text{Sr}) = 1.44 \cdot 10^{-25}$ kg), g the gravitational acceleration of $\approx 9.81\,\text{m/s}^2$ and θ the angle enclosed by gravity and the optical axis. For a vertical lattice, the gravitational energy shift is $\Delta\nu_{grav} = mg\lambda_{lat}/2h = 869\,\text{Hz}$ which breaks the potentials translational symmetry and strongly suppressing intersite tunneling [40]. More information about the tunneling effect can be found in Sec. 3.5.10.

There is no analytic solution to the Schrödinger equation with the potential from Eq. 2.7, which is not separable into independent radial and axial trapping potentials.

As discussed in [39] an approximation of the spatial dependent potential, provides an expression that allows the description of the energy spectrum of the atoms axial and radial states of motion. The axial potential is approximated in a single lattice site as a one-dimensional harmonic oscillator and the radial potential as a two-dimensional harmonic oscillator.

The respective axial and radial trap frequencies are [39]

$$\nu_z = 2\nu_{rec}\sqrt{\frac{U_0}{h\nu_{rec}}} \tag{2.9}$$

$$\nu_r = \sqrt{\frac{U_0}{m\pi^2 w_0^2}} \tag{2.10}$$

Including the first anharmonic terms of the trapping potential, eigenenergies in first order perturbation theory are given by Eq. (3) in [39].

The number of bound axial N_z and radial N_r states is best by solving the band structure of the one dimensional potential along the z direction. As seen in Fig. 2.1 the sideband transition is broadened towards the carrier indicating that the atoms have different sideband frequency which is due to the coupling of the axial and radial degrees of freedom. The weak radial confinement of the 1-D lattice allows radial state occupancy to very high numbers compared to the axial ones. But the trapping potential reduces with increasing radial excitation leading to an asymmetric lineshape of the sideband.

When the lattice beam waist ω_0 is known, ν_r can be estimated. A typical condition is $\nu_z \gg \nu_r$ with ν_r being at the order of a few hundred Hz and ν_z at the level of tens of kHz.

2.3. Sideband spectroscopy

Sideband spectroscopy provides a valuable tool to gather various information about the trap and properties of the confined atoms. From sideband spectroscopy as seen in Fig. 2.1 the lattice trapping potential can be read and from the shape of the sidebands the atoms

axial and radial temperature can be estimated. Such properties are relevant to determine the lattice frequency shift in the clocks uncertainty budget.

The blue (red) sideband is generated by the atoms that change their axial state of motion by $+1$ (-1) when undergoing the clock transition $^1\mathrm{S}_0 - {}^3\mathrm{P}_0$. The shape of the sidebands is smeared out towards the carrier due to the coupling between the longitudinal and transverse motion of the atoms. From the sidebands lineshape several properties of the atoms can be inferred. The sideband corner frequency is differs from the axial trapping frequency ν_z by one recoil frequency due to the trap anharmonicity. It can be read directly from the plot (Fig 2.1). The sideband corner frequency in Fig. 2.1 is identified by the high frequency edge of the blue sideband. According to Eq. 2.9 the axial trap frequency is related to the lattice potential depth which is a crucial contribution of the lattice frequency shift. From the enclosed area and the shape of the sidebands the axial and radial temperature T_z and T_r can be determined following the model developed in [39]. Here the strong confinement in the axial direction allows quantum treatment for the estimation of the axial temperature whereas the radial component can be treated classically by a Boltzmann distribution.

2.4. Lamb-Dicke Regime

In 1953 R. H. Dicke postulated recoil-free spectroscopy for atoms being tightly confined to a spatial extent that is smaller than the wavelength of the probe laser [41]. Atoms trapped in the Lamb-Dicke regime, e.g. in an optical lattice, the recoil due to absorption and re-emission of a lattice photon is absorbed by the potential and not by the atom itself. Excitation of external atomic states of motion is suppressed. For completeness a brief overview is presented following the description given in [39, 42]. For atoms trapped in a one dimensional (1-D) harmonic potential the trap energy levels are described by

$$E_n = h\nu_z \left(n + \frac{1}{2}\right) \tag{2.11}$$

with ν_z the axial trap frequency (Eq. 2.9) and n an integer value.

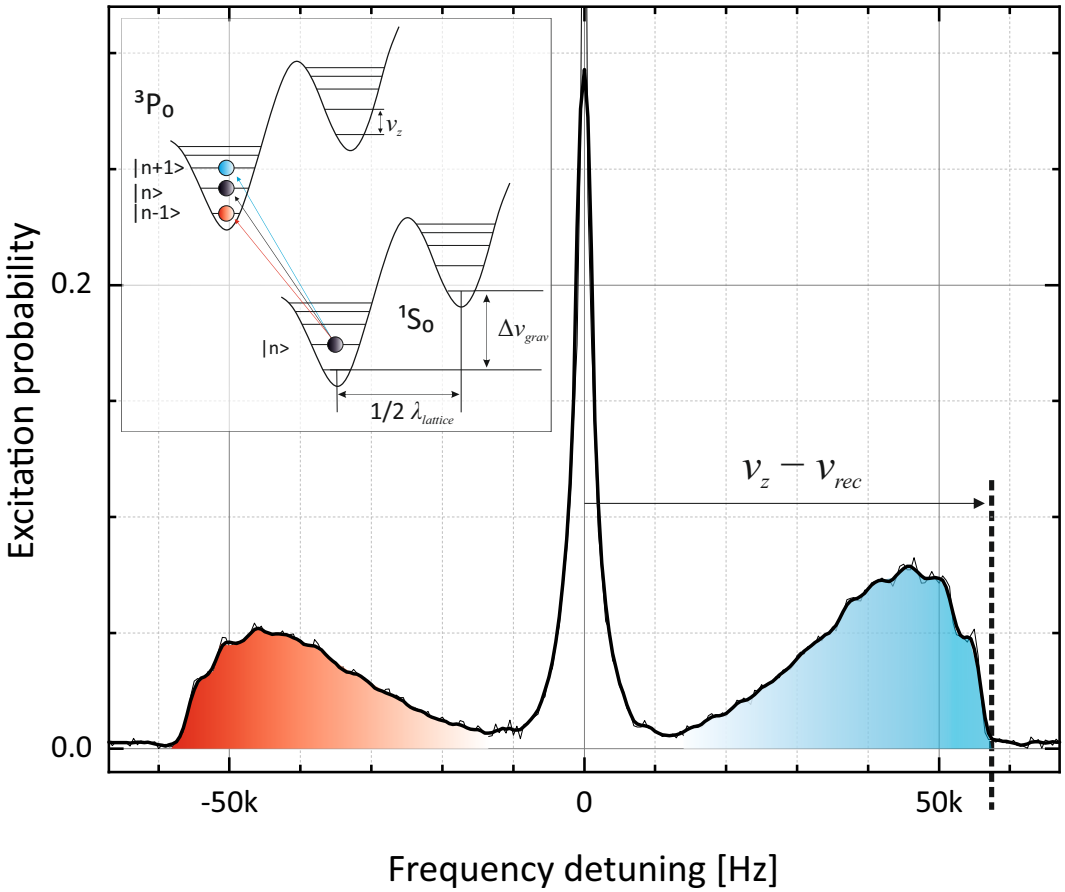

Figure 2.1.: Longitudinal sideband spectroscopy on the $^1S_0 - {}^3P_0$ clock transition. The corner frequency can be directly read from the plot (vertical black dashed line). From the ratio of the area enclosed by the sidebands the axial/radial temperature T_z of the trapped atoms can be estimated following the model developed in [39]. The radial temperature T_r is derived from a function fitting to the shape of the sideband. Details in the text. The "dents" in the sidebands seen predominantly at frequencies close to the edges arise from the anharmonicity of the trap [39].

The Lamb-Dicke parameter is defined as $\eta_z \equiv k_z z_0$ with wave vector $\vec{k}_z = 2\pi/\lambda_p$ the wave vector of the probe laser, m the atoms mass and the oscillator length z_0 that can be described as

$$z_0 = \sqrt{\frac{\hbar}{4\pi m \nu_z}} \tag{2.12}$$

The axial Lamb-Dicke parameter can thus also be described as

$$\eta_z = \frac{1}{\lambda_p}\sqrt{\frac{h}{2m\nu_z}} \tag{2.13}$$

The lightfield of the interrogation laser system is described classically as a traveling plane wave along the z-direction $A_0 \cdot e^{ik_z z}$. The atom light interaction for a transition from the initial state i to final state j is described by the dipole matrix element $\langle n_j|e^{ik_z z}|n_i\rangle$. The Lamb-Dicke parameter can be found by expanding the exponential to first order and using the usual raising ($\hat{a}^\dagger$) and lowering operators ($\hat{a}$) and considering z to be z_0 to

$$\begin{aligned}\langle n_j|e^{ik_z z}|n_i\rangle &\approx \langle n_j|1|n_i\rangle + \langle n_j|ik_z z|n_i\rangle \\ &= \delta_{n_i,n_j} + ik_z z_0 \left(\langle n_j|\hat{a} + \hat{a}^\dagger|n_i\rangle\right) \\ &= \delta_{n_i,n_j} + ik_z z_0 \left(\sqrt{n_i}\delta_{n_{i+1},n_j} + \sqrt{n_i+1}\delta_{n_{i-1},n_j}\right)\end{aligned} \tag{2.14}$$

When squaring the matrix element one finds three terms remaining giving

$$\left|\langle n_j|e^{ik_z z}|n_i\rangle\right|^2 = \delta^2_{n_i,n_j} + \eta_z^2\left(n_i\delta^2_{n_{i+1},n_j} + (n_i+1)\delta^2_{n_{i-1},n_j}\right) \tag{2.15}$$

A more general expression can be found in Eq. 3.16 in [35]. The conclusion from Eq. 2.15 is that in the Lamb-Dicke regime there are three cases for the dipole matrix operator to be non-zero, or in other words when absorption is allowed. Considering a single atom in the electronic ground state $^1S_0$ and motional state n_i in a harmonic potential. When operating the potential at the magic wavelength the potential is the same for the excited state $^3P_0$. For excitation where the motional state remains unchanged $\Delta n = 0$ only the first delta function in Eq. 2.15 is non-zero. This transition is known as the carrier transition at frequency ν_0. For $\Delta n = \pm 1$ the transition frequency is shifted by $\pm\nu_z$ representing sideband transitions which are often referred to as the red ($\Delta n = -1$, $\nu_0 - \nu_z$) and blue

($\Delta n = +1$, $\nu_0 + \nu_z$) sideband. The sideband frequency ν_z scales with the potential depth to $\sqrt{U}$ and are at a high frequency detuning compared to the width of the transition. The relative strength of the side bands compared to the carrier transition is given by $\eta_z^2(n_i+1)$ thus strongly suppressing even the first order sidebands already. For typical experimental conditions used in the Sr3 clock ν_z is approximately 55 kHz leading to an oscillator length of $z_0 = 33\,\text{nm}$ and a Lamb-Dicke parameter of $\eta_z = 0.3$ with $\lambda_p = 698.45\,\text{nm}$. This confirms confinement within the Lamb-Dicke regime for the Sr3 clock. Additionally the Fourier limited linewidth is typically very narrow (in the order of Hz) compared to ν_z which is often refereed to the resolved sideband regime that allows sideband spectroscopy. Sideband spectroscopy allows to gather various information on the trapped atoms, such as the axial and radial temperature and the trap frequency ν_z (Sec. 2.3). In a 1-D lattice the confinement in radial direction is a lot weaker compared to along the axial direction ($\nu_z \gg \nu_r$). For a Gaussian beam the radial Lamb-Dicke parameter [39] is

$$\eta_r = \frac{\Delta\theta}{\lambda_p}\sqrt{\frac{h}{2m\nu_r}} \tag{2.16}$$

with $\Delta\theta$ the angle between probe and lattice laser. Even small amounts of beam misalignment will result in a significant contribution to the carrier line shape. So great care has to be taken in aligning clock and lattice beam co linear.

2.5. Precision spectroscopy and lock to the clock transition

During the red MOT, the atoms are loaded into the optical lattice at the maximum potential depth the setup can deliver of approx. 150 E_{rec}. According to Eq. 3 in [39] this allows for atoms occupying a axial quantum number of approx. v = 6 to be trapped. To select the coldest atoms form the ensemble the potential is lowered to approx. 26 E_{rec} for about 40 ms. This procedure is called "spilling" where the number of bound states is limited to $v_z \leq 2$ and atoms occupying higher lying states become untrapped. This results in a more defined, less energetic distribution of the atomic ensemble in the vibrational states.

State preparation

The remaining atoms are then prepared in either of the $m_F \pm 9/2$ stretched magnetic sublevels by optical pumping on the ${}^1\mathrm{S}_0(F = 9/2) - {}^3\mathrm{P}_1(F' = 9/2)$ "stirring" transition called spin polarization. In an unpolarized atomic ensemble all $m_F = -9/2... + 9/2$ magnetic sublevels are equally populated. By optical pumping, the distribution is transfers to the outermost $m_F = \pm 9/2$ states that are probed during clock spectroscopy.

Population in neighboring m_F states is causing frequency shifts, namely the line pulling effect (Sec. 3.5.9). To remove such residual population, the ensemble will be purified in the next step. Therefore a bias magnetic field is applied that separates neighboring m_F states on the order of approx. 1 kHz due to the Zeeman effect. A Rabi π-pulse resonant on the ${}^1\mathrm{S}_0(m_F = \pm 9/2) - {}^3\mathrm{P}_0(m'_F = \pm 9/2)$ transition with a Fourier-limited linewidth of about 16 Hz only excites those atoms in the $m'_F = \pm 9/2$ state. The frequency of this pulse is several linewidth detuned from a neighboring m_F state ensuring that no other m_F state is addressed. Atoms populating $m_F \neq \pm 9/2$ states remain in the ground state and are heated out of the trap by applying a pulse resonant on the ${}^1\mathrm{S}_0 - {}^1\mathrm{P}_1$ transition.

When performing clock spectroscopy, a Rabi π-pulse de-excites the atoms from the ${}^3\mathrm{P}_0$ state to the ${}^1\mathrm{S}_0$ state. The bias magnetic field is chosen such that the Zeeman frequency splitting between the outermost $m_F = \pm 9/2$ is approx. 580 Hz. After clock interrogation, the fraction of excited/de-excited atoms by destructive fluorescence state detection. Applying a short (5 ms, 80 µW) laser pulse resonant to the ${}^1\mathrm{S}_0 - {}^1\mathrm{P}_1$ transition atoms in the ground state scatter photons. The fluorescence signal strength is proportional to the number of atoms in the ground state. The scattered light is imaged onto a photo multiplier (PMT) where it is converted into an electronic current. The signal is amplified to be processed by the experiment control system.

To determine the excitation probability of the clock spectroscopy, from which the frequency correction is derived, a total of three detection pulses are applied. As already described the first pulse detects the number atoms that have been de-excited to the ${}^1\mathrm{S}_0$ ground state. The number of atoms that remained in the excited state is detected by repumping them to the ${}^1\mathrm{S}_0$ ground state first, and subsequently apply a detection pulse. Repumping is done by two repump lasers (Fig. 1.4). The third detection pulse determines the background signal for offset correction.

2.5.1. Lock to the atoms

In order to distinguish the frequency correction from the excitation probability and to remain in resonance with the atoms, each of the four locking points at the full width half maximum (FWHM) points are probed (Fig. 2.2). The Fourier limited linewidth of the Rabi fringe is related to laser pulse duration by FWHM $\approx 0.8/t_{\text{pulse}}$ [43]. The measured excitation probability is the frequency discriminator from which the error signal for the clock laser is derived. The steeper the slope of the fringes the higher the frequency sensitivity. Steeper slopes can be achieved by longer interrogation times. The sequence described above is referred to as the single-cycle operation which is the normal mode of clock operation. For self evaluation of certain frequency shifts, the frequency correction of two independent locks is compared where the parameter of interested is altered between the two cycles. This is refereed to as interleaved measurement.

The effect of the spin polarization on the can be seen in Fig. 3.33 where an excitation probability of about 80% was reached for the desired $m_F = \pm 9/2$ states.

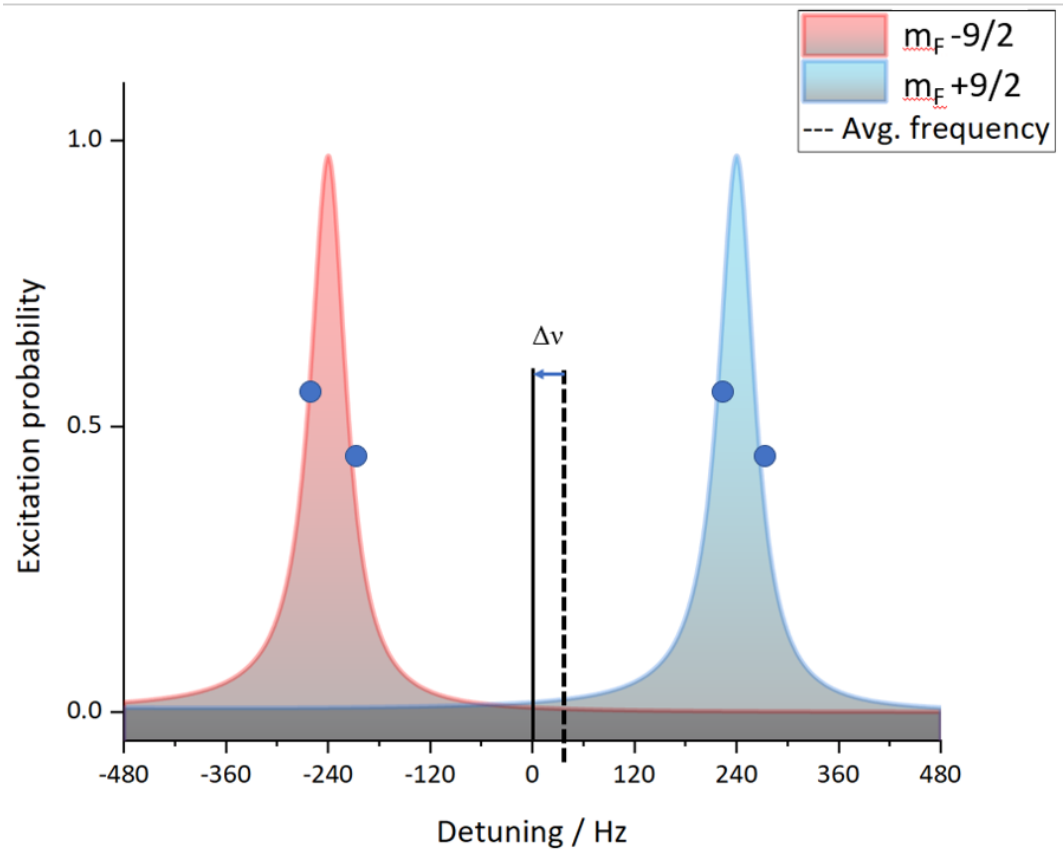

Figure 2.2.: Principle of interrogation of the clock transition. From the four interrogations at the two $m_F = \pm 9/2$ Zeeman sublevels (blue dots) a frequency offset $\Delta\nu$ is derived to correct the clock laser frequency to resonance (solid vertical line). At the full width half maximum points of the fringe the slope is steepest and the frequency sensitivity highest.

2.6. Systematic frequency shifts on the clock transition

The following subsections are presenting an overview about the relevant systematic frequency shifts in a strontium optical lattice clock. All the effects are listed in the clock's uncertainty budget. For a preliminary uncertainty budget of the cryogenic Sr3 system please refer to chapter 3.5. The uncertainty budget is found in Tab. 3.4.

2.6.1. Stark-effect

In the presence of an electric field the energy splitting of atomic levels is shifted according to

$$\Delta\nu_{Stark} = -\frac{1}{2h}\left(\Delta\alpha_{DC}\vec{E}_0^2 + \Delta\alpha_{AC}(\omega)\langle\vec{E}^2(\omega)\rangle\right) \tag{2.17}$$

with $\vec{E}$ the static and $\vec{E}(\omega)$ dynamic component of frequency ω of the electric field. Furthermore, $\Delta\alpha_{DC}$ and $\Delta\alpha_{AC}(\omega)$ are the corresponding differential polarizabilities of the involved atomic states. In a static electric field the frequency shift experienced by the atoms can therefore be written as

$$\Delta\nu_{Stark} = -\frac{1}{2h}\left(\Delta\alpha_{DC}\vec{E}_0^2\right) \tag{2.18}$$

The ac-Stark frequency shift arises from the interaction between the atoms and alternating electric fields such as the optical lattice (Sec. 2.6.3) or with the probe light (Sec. 2.6.5). The most relevant frequency shift for strontium lattice clocks, the black body radiation shift is also an ac-Stark shift and is discussed in the following section in more detail.

2.6.2. Black body radiation frequency shift

In state-of-the art strontium optical lattice clocks operated at room temperature, the black body radiation (BBR) shift is the dominant source of frequency shift and shift uncertainty. The frequency shift is about 2.1 Hz or $5 \cdot 10^{-15}$ in fractional units. The

shift uncertainty is currently limited to approx. $2 \cdot 10^{-18}$ by the knowledge of the atomic response [44]. At temperature T the spectral density of the BBR is described by Planck's law

$$\rho(\omega, T) = \frac{\hbar\omega^3}{4\pi^3 c^2} \frac{1}{e^{\hbar\omega/k_b T} - 1} \tag{2.19}$$

with k_b being the Boltzmann constant, T the absolute temperature in Kelvin and $\hbar$ the reduced Planck constant. The time average of the square of the electric field can be written as

$$\langle |E|^2 \rangle_T = \frac{8\pi^5 k_b^4}{15\epsilon_0 h^3 c^3}\ T^4. \tag{2.20}$$

The atomic interaction with the BBR-field leads to a differential energy shift on the clock states. The resulting frequency shift on the $^1S_0$ and $^3P_0$ clock transition resulting from the BBR-spectrum integrated over all frequencies can be written as

$$\Delta E = \frac{1}{4h\epsilon_0 \pi^3 c^3} \int_0^\infty \Delta\alpha(\omega) \frac{\omega^3 d\omega}{e^{(\omega/k_B T)} - 1} \tag{2.21}$$

with $\Delta\alpha(\omega)$ being the differential polarizability of the clock states.

The resulting frequency shift on the clock transition as described in [45]

$$\Delta\nu_{BBR}(T) = \Delta\nu_{stat} \left(\frac{T}{T_0}\right)^4 + \Delta\nu_{dyn} \left[\left(\frac{T}{T_0}\right)^6 + \mathcal{O}\left(\frac{T}{T_0}\right)^8\right] \tag{2.22}$$

with $\Delta\nu_{stat} = -2.130\,23(6)$ Hz [45] and $\Delta\nu_{dyn} = -148.7(7)$ mHz [44] being the static and dynamic coefficient at $T_0 = 300\,\mathrm{K}$

Recently, our group investigated the theoretical treatment of the BBR shift and found a significant deviation in $\Delta\nu_{dyn}$ [46] to the published value in [44] that manifests in a BBR frequency shift difference of about $4{\cdot}10^{-18}$ for room temperature operated Sr-lattice clocks. The reported value in [46] for the dynamic contribution is $\Delta\nu_{dyn} = -150.51(43)$ mHz. In the temperature range from 50 K to 350 K the dynamic shift can be written as a polynomial

$$\Delta\nu_{dyn}(T) \approx \eta_6 \left(\frac{T}{T_0}\right)^6 + \eta_8 \left(\frac{T}{T_0}\right)^8 + \eta_{10} \left(\frac{T}{T_0}\right)^{10} \tag{2.23}$$

,

which covers the range relevant in this work. The approximation in Eq. 2.23 is accurate to the $1 \cdot 10^{-19}$ level to the calculated $\Delta\nu_{dyn}$ at room temperature a far below that level at cryogenic temperatures (Fig. 3 in [46]). Any BBR shift evaluation in this work relating Sr3 will use the formalism presented above with the updated value on the dynamic coefficient based on the work in [46].

The previous value of $\Delta\nu_{dyn}$ from [44] deviates by about $1 \cdot 10^{-18}$ to the reevaluated at room temperature (293 K). This is quite significant considering the 1σ systematic uncertainty of the most accurate Sr-lattice clocks [44, 47] of about $2 \cdot 10^{-18}$. Especially for inter species frequency comparisons that are not limited to the accuracy of current primary standards, the cesium fountain clocks, this is of importance. Such measurements performed in the past may be considered to undergo a reevaluation.

The evaluation of the BBR frequency shift and its uncertainty is derived from the temperature readings of the temperature sensors. The temperature readings of the different sensors is modeled as a rectangular probability distribution between the highest T_{max} and lowest T_{min} reading to a representative temperature

$$T_{rep} = \frac{T_{max} + T_{min}}{2} \tag{2.24}$$

with an uncertainty of

$$u(T_{rep}) = \frac{T_{max} - T_{min}}{\sqrt{12}} \tag{2.25}$$

This method follows the recommendation of [48] in determining a representative temperature.

2.6.3. Lattice light shift

A deep understanding of the interaction between the lattice and the atom is essential once clock uncertainty surpasses the 10^{-17} level. Here higher-order lightshift contributions such as hyperpolarizability and multipole atom-light interaction become relevant and must be considered.

In state-of-the-art strontium lattice clocks, the lattice induced light shift can be the leading contribution in the uncertainty budget apart from the BBR shift uncertainty. In a red detuned lattice, which is the case as for most strontium lattice clocks, the atoms are trapped in the anti-nodes of the interference pattern. In the presence of such an electric field, the neutral strontium atom will be polarized and respond with a change in transition frequency.

$$\Delta\nu = -\frac{1}{2h}\Delta\alpha_i|E|^2 \tag{2.26}$$

with α_i the polarizability of the corresponding state $|i\rangle$ and E the external electric field. The sign of α is given by the frequency detuning of the trapping laser relative to the atomic transition. A smaller laser frequency (red detuned) leads to a positive sign and the atoms will be trapped in the anti-nodes of the electric field while the opposite case gives a blue detuned lattice with atoms captured in the nodes. Trapping atoms therefore requires inducing a non-zero polarizability by the lattice light field for each of the two clock states. The wavelength and polarization of the lattice laser can be chosen such that the differential polarizability $\tilde{\alpha} = \alpha_e - \alpha_g$ of excited- and ground state vanishes resulting in an intensity independent frequency shift of zero of the clock transition. This is the concept of the so called "magic wavelength" [49]. More details can also be found in [37, 42, 50].

Considering the electric dipole (E1) interaction as described in [51], the frequency shift $\Delta\nu^{E1}$ can be decomposed into scalar ($\Delta\nu^{sc}$), vector ($\Delta\nu^{vec}$) and tensor ($\Delta\nu^{ten}$) shift contributions where $\Delta\nu^{vec}$ and $\Delta\nu^{ten}$ are sensitive to the lattice polarization. For common orientations of a linear polarized lattice either perpendicular or parallel to the bias magnetic field, $\Delta\nu^{ten}$ is always non zero. Typically $\Delta\nu^{sc}$ is adjusted by the lattice frequency such that it balances $\Delta\nu^{ten}$ to $\Delta\nu^{sc} + \Delta\nu^{ten} = 0$. This operating condition where $\Delta\nu^{E1} = 0$ is called the "Stark-cancellation wavelength". For lattice polarization as discussed above the vector shift cancels.

To reach a systematic uncertainty of below 10^{-17}, this concept must be expanded to deal with higher-order light shift contributions such as the electric-quadrupole (E2) and magnetic-dipole (M1) polarizabilities (E2M1) and the hyperpolarizability. In a 1D lattice along the z-axis the E2M1 shift $\tilde{\alpha}^{qm}(n_z)$ introduces a lightshift dependence of the vibrational state n_z. The hyperpolarizability $\tilde{\beta}(\omega, \zeta)$ that depends on the lattice frequency

and degree of circular polarization ζ. In ytterbium and mercury based clocks there exists a "magic polarization" [52] where the hyperpolarizability can be canceled by tailoring a certain degree of circularity. The hyperpolarizability for linear β^l and circular β^c light then cancels. However this is not possible for strontium since the β^l and β^c require opposite signs.

For all of PTB's Sr-lattice clocks, we follow the concept of the "operational magic wavelength" (opMWL) presented by the group of Prof. Katori [52]. This concept is taking higher order shift contributions, the E2M1 polarizablity and the hyperpolarizablity into account that the E1 magic wavelenght protocol is neglecting. The idea of the opMWL is to operate the lattice frequency detuned from the E1 magic wavelength (by a few MHz as proposed in [53]) at the benefit of achieving a lightshift that remains insensitive to trap depth variations for a certain range. In the following the notation from [53] will be used. The full description of the frequency shift of the clock transition taking all the mentioned perturbations into account is given as

$$h\delta\nu(u, \delta_L, n_z) \approx \tag{2.27}$$

$$\left(\frac{\delta\tilde{\alpha}^{E1}}{\delta\nu}\delta_L - \tilde{\alpha}^{qm}\right)\left(n_z + \tfrac{1}{2}\right)u^{1/2} - \left[\frac{\delta\tilde{\alpha}^{E1}}{\delta\nu}\delta_L + \tfrac{3}{2}\tilde{\beta}\left(n_z^2 + n_z + \tfrac{1}{2}\right)\right]u + 2\tilde{\beta}\left(n_z + \tfrac{1}{2}\right)u^{3/2} - \tilde{\beta}u^2$$

with the differential hyperpolarizability coefficient $\tilde{\beta} = -458(\pm 14) \cdot 10^{-9}$ Hz which is the weighted mean of the values published in [44, 53–55]. For the coefficient of the E2M1 polarizability, significantly disagreeing values are published in [51, 53, 55, 56][5]. In the following the weighted mean of the values published in [51, 53, 55] is used which is $\tilde{\alpha}^{qm} = -369.5(\pm 456.8) \cdot 10^{-6}$ Hz. In Eq. 2.27 the radial states of motion n_r are taken into account in

$$u = U_0 - k_B T_{rad}/\nu_{rec} h \tag{2.28}$$

which is a thermally averaged potential of the peak potential U_0 determined by sideband spectroscopy (Sec. 2.3).

[5] [56] without uncertainty

2.6.4. First- and second-order Zeeman effect

The atoms are not only sensitive to electric fields but also to magnetic fields. The Zeeman-effect is used in the interrogation sequence and essential for the general clock operation (see 2.5). Also to compensate for Earth's magnetic field (and any other stray magnetic field from the laboratory environment of course) at the location of the atoms, their responds due to the Zeeman-Effect is used.

In ^{87}Sr the difference in Landé g-factors of the ground- and excited clock state lead to a non zero frequency shift. The first order (linear) Zeeman shift can be written as

$$\Delta\nu_{Zee}^{(1)} = \delta g \mu_B m_F B/h \tag{2.29}$$

with δg the difference in Landé g-factors and m_F the magnetic sublevel ($m_F = \pm 9/2$) of the clock states and B the (applied) magnetic field.

$$\mu_B = e\hbar/2m_e c \tag{2.30}$$

where μ_B the Bohr magneton, m_e the electron mass. The linear Zeeman effect as a source of a systematic frequency shift can be neglected, since it averages to zero in the interrogation sequence described in 2.5.

The second-order Zeeman effect however does not cancel since both $m_F = \pm 9/2$ states are shifted in the same direction. This shifts the center frequency which leads to a frequency shift depending on the magnitude of the applied spectroscopy magnetic field. Typically the Zeeman splitting frequency of the stretched magnetic substates ($m_F = \pm 9/2$) is a few hundred Hz. The frequency splitting can be written as

$$\Delta\nu_{Zee}^{(2)} = aB^2 \tag{2.31}$$

where the coupling coefficient a is an atomic property of the relevant states. Since the knowledge of the absolute magnetic field is typically not of interest because the Zeeman frequency splitting of the involved magnetic sublevels is the relevant information and obtained during a clock interrogation cycle (Sec. 2.5), it is more convenient to write the parameter α in units of Hz/Hz^2. The frequency shift with respect to the splitting frequency

of the $m_F = \pm 9/2$ can be written as $\Delta\nu_{Zee}^{(2)} = \xi(\Delta\nu_{Zee}^{(1)})^2$. Measurements in Sr1 resulted in a value of $\xi = -2.40(2)\text{Hz/Hz}^2$ [57] was found which is in agreement with previous measurements [42, 58, 59]. The JILA group published a measurement with improved accuracy yielding $\xi = -2.456(3)\text{Hz/Hz}^2$ [47]. Since it is the most accurate measurement to date the coefficient from [47] will be used in the evaluation of the second-order Zeeman shift throughout this manuscript. The values published in [60] have confirmed the value published in [47].

2.6.5. Clock laser AC-Stark shift

When interrogating the atoms with the clock laser, coupling of the clock transition to other states causes a frequency shift thereof. The typical Rabi-π-pulse duration is about 700 ms for the Sr1 and Sr3 clocks.

The reduced matrix element can be deduced from the lifetime of the $^3\text{P}_0$ state as measured in [25] and used to determine the required intensity of a Rabi π-pulse with the duration given above ($I = 2.9 \cdot 10^{-7}$ W/cm^2). With respect to the shift coefficient of $-28(2)$ Hz/ (Wcm^{-2}) [61] a frequency shift of $-1.9(19) \cdot 10^{-20}$ is expected.

2.6.6. Other sources of frequency shifts

This section briefly discusses other systematic frequency shifts that also needs to be considered to the ones mentioned above. We identified several technical sources that can cause a frequency shift on the clock transition.

Line pulling

For spectroscopy, the atoms are prepared in either of the $m_F = \pm 9/2$ Zeeman sub levels of the $^3\text{P}_0$ state. The line-pulling frequency shift can arise due to two different aspects. First, a residual population in neighboring m_F states, predominantly the $m_F = \pm 7/2$ states, can be (de)excited off-resonantly by the clock pulse causing an asymmetric background for the $m_F = \pm 9/2 - m_F' = \pm 9/2$ clock transition and shifting the line center. To prevent such parasitic population in other Zeeman states we use a technique called "clean-up" as already described in 2.5. The remaining population is measured experimentally by scanning the expected frequency with the clock laser and measure the excitation probability.

From the Zeeman splitting of the sub levels and the experimentally measured population the frequency shift can be determined.

The second aspect that contributes to the line pulling effect arises from imperfect polarization of the clock laser at the position of the atoms. When its polarization is not purely linear along the quantization axis defined by the magnetic field, the atoms can get (de)excited on $m_F = \pm 9/2 - m'_F = \pm 7/2$ $\sigma^{\mp}$-transitions. A potential cause is either misalignment of the clock lasers polarization axis (set by e.g. a polarizing beam splitter) or due to stress induced birefringence of optical transmitting elements (e.g. viewports). As a consequence the an admixture of σ-polarisation is present that allows coherent transition to neighboring m_F states causing frequency shifts by line pulling.

A maximum population of 10% for atoms in other states was seen experimentally. An approximation on this effect can be done by numerically integrated the time-dependent Schrödinger equation [62] to estimate an upper limit for the frequency shift.

Optical path length error

The new clock system Sr3 is placed in the same laboratory as its predecessor Sr1. Its interrogation laser system [16, 63] is in the neighboring room requiring light transport to the clock via a 15 m long optical fiber (single mode, polarization maintaining).

Any kind of disturbance acting on the fiber (vibration or temperature change) or a chirp on the AOMs RF-power result in a change of laser phase. During interrogation those phase changes will affect the excitation probability of the atomic ensemble resulting in a frequency shift. To prevent such phase changes an optical path length stabilization was implemented ensuring stable laser phase delivered to the atoms. More details can be found in [64]. For common experimental parameters used in this experiment its contributions is added as an uncertainty of $1 \cdot 10^{-19}$ only.

Servo error

Narrow linewidth spectroscopy on the $^1S_0 - {}^3P_0$ clock transition requires sufficient pre-stabilization of the interrogating laser system. Therefore it is locked to a room temperature ultrastable reference cavity made from ultra low expansion (ULE) glass [16]. The stability of the laser system is improved further by stability transfer from a cryogenic silicon cavity [17] via a frequency comb (Sec. 3.3). Such cavities always suffer from frequency drifts due to e.g. aging of the spacer material. Linear drift rates reported in [17] are 15 mHz/s for the ULE cavity and about 100 µHz/s for the cryogenic Si-cavity. In the

clock measurement cycle, the linear drift rate is measured and compensated by a feed forward after every interrogation of the four locking points. Nevertheless a second order drift rate remains and can lead to an offset frequency relative to the constant atomic resonance frequency. Typical a single interrogation cycles takes approx. 1.55 s requiring 6.2 s (12.4 s) for an entire single lock (interleaved) measurement. According to [59] the calculated time constant for the second order drift rate to settle is 124 s (with drift gain $\beta = 0.05$ and lock gain $G = 0.5$). The observed second order drift of the Si cavity $\ddot{\nu}_{cav}$ is about 77 nHz/s^2 which is added as an upper limit uncertainty estimated for the servo error of $0.5 \cdot 10^{-18}$.

Gravitational redshift

When comparing the transition frequency of atomic clocks such as PTBs Sr and Yb^+ clock, the relativistic redshift due to a difference in gravity potential at the position of the atoms must be considered [65,66]. In the case of stationary clocks that are co-rotating with Earth, the gravitational redshift difference of an electromagnetic wave traveling from the position A to position B is given by

$$y_B - y_A = \frac{\Delta W}{c^2} + \mathcal{O}(c^{-4}) \tag{2.32}$$

with W the geopotential of the individual clock. Here $y_{A,B}$ are the fractional frequency shifts due to the potential difference. The redshift becomes positive when the potential at point B is larger (typically greater geometric height) than at point A. For two oscillators of equal frequency and the observer placed in point B, the oscillator in point A appears to run at a lower frequency of approx. $1 \cdot 10^{-18}$ cm^{-1} of height difference.

2.7. Stability of optical clocks

2.7.1. Quantum projection noise

Besides the systematic uncertainty of an atomic clock, another main property is its instability. The output frequency of an atomic clock always comprises noise caused by different sources. Theses are either related to the quantum nature of the experiment, the quantum projection noise (QPN), or to technical sources such as electronic noise or frequency

fluctuations of the interrogating laser system. Laser frequency noise in combination with the non continuous interrogation of the atomic transition is referred to as the Dick effect (sec. 2.7.2). A common measure to estimate the instability (= the statistic significance of a measurement) of a given time τ is the Allan deviation (ADEV) $\sigma_y(\tau)$ [21, 67, 68]. It is given by

$$\sigma_y(\tau) = \frac{\Delta\nu}{\nu_0}\frac{1}{K\sqrt{N}}\sqrt{\frac{T_c}{\tau}} \tag{2.33}$$

where for Rabi excitation of pulse duration T_π, $\Delta\nu$ is the Fourier limited line width of approx. $0.8/T_\pi$ of the $^1S_0 - {}^3P_0$ clock transition frequency of $\nu_0 = 429\,228\,004\,229\,873.0(2)$ Hz [69]. The parameter K accounts for the observed transition line shape. It is in the order of ≈ 1 for Rabi spectroscopy. T_c is the single interrogation cycle time (Sec. 2.5, $T_c = T_\pi + T_{prep}$) and N the signal to noise ratio at the quantum projection noise limit which is equal to the number of atoms for an excitation fraction of p_e=0.5. QPN is a fundamental quantum mechanical property related to the interrogation of the atoms. It arises when the atoms are in a superposition state of ground $|g\rangle$ and excited state $|e\rangle$. Detecting the atomic state will collapse the superposition into either of the states. The excitation probability is estimated by the number of detected atoms in $|g\rangle$ and $|e\rangle$.

$$p_e = \frac{N_e - N_o}{N_e + N_g - 2N_o} \tag{2.34}$$

where N_o is the measurement offset. For many atoms the variance of Eq. 2.34 can be written as

$$\sigma(p_e) = \sqrt{N p_e(1 - p_e)} \tag{2.35}$$

with N the number of clock atoms. Eq. 2.35 has a peak uncertainty at the clocks operating point $p_e = 0.5$. Since the excitation probability of a single particle is binary several measurements are required to precisely determine its excitation probability. This features a major advantage of lattice clocks compared to ion clocks where in a single interrogation cycle many atoms contribute to the spectroscopic signal. This leads to a huge advantage in instability over Ion clocks were only one particle is available.

Nevertheless in some aspects Ion clocks are favorable over lattice clocks e.g. due to lower vulnerability of certain systematic effects. Combining the benefits with larger particle number triggered the development of multi Ion clocks to close the gap in instability of such systems to lattice clocks.

2.7.2. Dick Effect

As discussed in Sec. 2.5 every clock cycle consists of three different steps. Preparation of the atomic ensemble, performing clock spectroscopy (interrogation) and state readout. During preparation and readout the interrogation laser's frequency is not observed by the atoms. in this so called "dead-time" aliasing of laser frequency noise leads to a phantom frequency offset known as the Dick effect [43] that degrades clock stability. Interrogation lasers with low noise characteristics such as system that are prestabilized to ultra stable cavityies [17, 63] allow longer probing duration that reduces the Dick effect to a certain extend. But for a single clock dead-time will always be present so as the Dick effect. The influence of the Dick effect on the Sr1 clock was discussed in great detail in [57, 70]. Since the same interrogation system is now in use in Sr3 the previous characterization is still applicable and will not discussed here again.

3. The all cryogenic Sr-lattice clock Sr3

The Sr-lattice clock at PTB has a history of about two decades where it contributed high quality scientific results in various fields of research such as the search for dark matter [71], relativistic geodesy [72], temporal variation of fundamental constants [8] and more. The characterization of systematic effects on the Sr atoms was successfully published in numerous publications [45, 57, 70].

In the characterization of the most important frequency shift in Sr-lattice clocks, the black body radiation (BBR) shift, Sr1 contributed valuable experimental results [45]. Even today, nearly a decade later the determined static coefficient $\Delta\nu_{stat}$ of the total BBR frequency shift is still the most accurate value available.

The dynamic contribution $\Delta\nu_{dyn}$ published in [45] was updated with lower uncertainty a few years later in [44] but both values are in agreement within their uncertainties. Recently the evaluation of $\Delta\nu_{dyn}$ was revised in our group [46] which lead to a correction of approx. $1 \cdot 10^{-18}$ in the total BBR frequency shift [6]. The total systematic uncertainty of PTB's Sr-lattice clock Sr1 operated at room temperature is at the level of approx. $2 \cdot 10^{-17}$, dominated by the uncertainty of the BBR shift. The limitation arises due to temperature differences across the chamber. From the highest T_{max} and lowest T_{min} temperature measured the representative temperature and uncertainty $(T_{max} + T_{min})/2$ are estimated with an uncertainty of $(T_{max} - T_{min})/\sqrt{12}$. This procedure is in accordance to BIPM´s "GUM: guide to the Expression of Uncertainty in Measurements" [48]. The Sr1 vacuum chamber does not allow a reduction of the temperature differences due to its design. Even with extremely well controlled temperature of the apparatus as presented in [47], a fractional uncertainty of about $1.4 \cdot 10^{-18}$ remains[7] due to the uncertainty of the dynamic coefficient. In other words without better knowledge of the dynamic coefficient a Sr-lattice

[6] At a temperature of 293 K

[7] $0.9 \cdot 10^{-18}$ after the revision of [46]

clock operated at room temperature can not surpass a total systematic uncertainty below about $0.9 \cdot 10^{-18}$. To improve the BBR shift uncertainty, either the uncertainty of the dynamic coefficient must be lowered or performing clock operation at lower temperatures. Lower operation temperatures relax the requirements on the knowledge of the coefficients inherently as demonstrated in Fig. 3.8 already. In the design of the new Sr3 clock we follow that approach and operated it at around 80 K. In the following chapter the new physics package is described with a focus on its impact on the BBR shift and the overall clock performance.

3.1. The new physics package

The new vacuum system features a significantly different approach as the Sr1 clock. The design of Sr1 was a rather simple large sphere and not optimized for homogeneous temperature distribution that minimizes the BBR shift uncertainty. The main improvement in Sr3 is a three layer design to shield the atoms in the inner layer best from room temperature BBR. The first layer is basically the vacuum chamber itself made from stainless steel. Inside the vacuum system a dual layer cryostat (Figs. 3.1, 3.3 3.9) made from oxygen-free high thermal conductivity copper (OFHC) is attached to a cooling engine that supports cryogenic operation. The dual layer design of the cryostat shields the atoms best from black-body radiation and the inner layer provides excellent temperature homogeneity. A detailed description of the cryostat can be found in Sec. 3.2.1. In the following sections the Sr3 systems is described in further detail.

3.1.1. Vacuum chamber

The Sr3 vacuum chamber is fabricated from low magnetic stainless steel 1.4404 (316L). Their CF-flanges are made from a steel alloy (1.4429, 316LN ESR) that offers an even lower magnetic permeability (approx. 1.005 Vs/Am compared to 1.1 Vs/Am of 316L). After machining low hydrogen annealing at a temperature of approx. 950 °C in vacuum was applied, to minimize the diffusion of hydrogen into the chamber. This may degrade the systems vacuum pressure. The vacuum chamber and the relevant attachments are mounted into a lightweight aluminum framework. At the bottom a 400 L/s Ion pump with

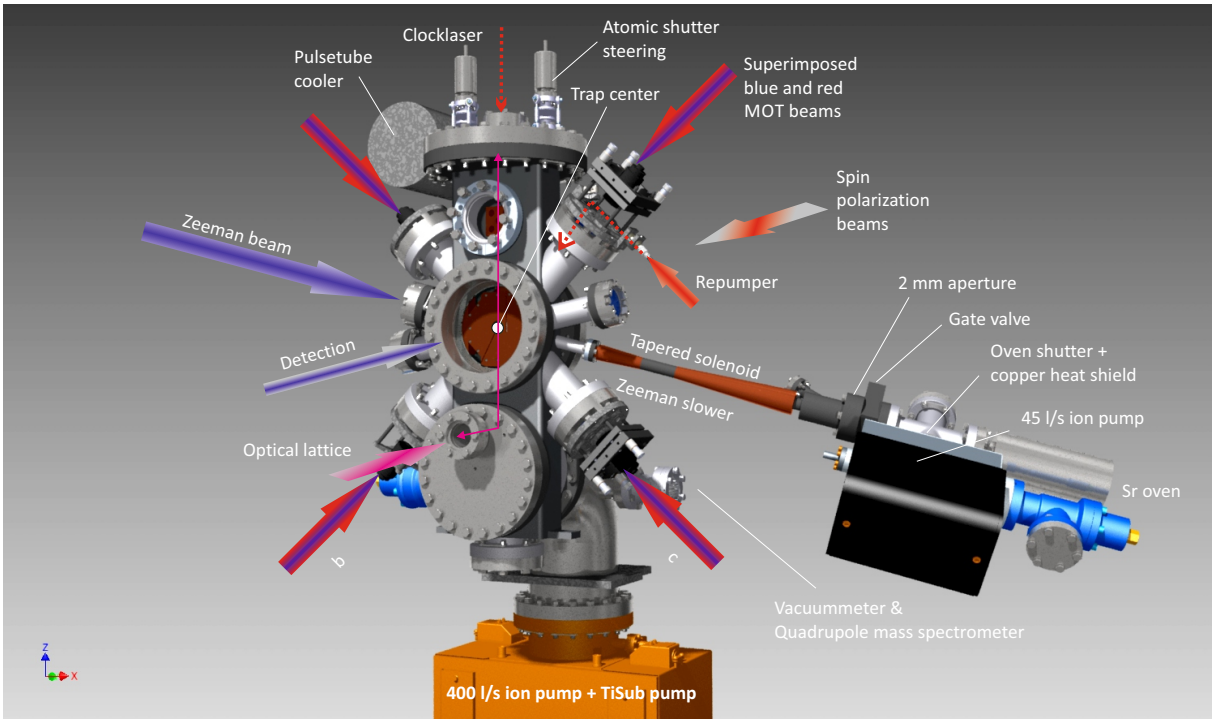

Figure 3.1.: Physics package of Sr3. The optical beams are delivered via FC-APC optical fiber to the vacuum chamber. The superimposed MOT beams at 461 nm and 689 nm are delivered from the bottom (b and c) at an angle of about 45° towards gravity. The vertical lattice is inserted horizontally through a CF-40 viewport at the front and reflected upwards by an in-vacuum mirror. The clock laser is counter propagating to it. The MOT coils are not shown here. They are placed in the 140 mm diameter viewport next to the trap center where the detection and horizontal MOT beams (not shown) are delivered.

an additional titanium sublimation pump (Gamma Vacuum 400LX TiTan Ion Pump) is installed (Fig. 3.1). Close to the elbow that holds this ion pump, at a CF-40 T-piece a Bayard-Alpert vacuum meter (BARION pro from Vacom) is installed that allows to measure the vacuum pressure ranging from $1 \cdot 10^{-2}$ mbar down to $3 \cdot 10^{-11}$ mbar. At the other port of the T-piece, opposite to the vacuum meter, a residual gas analyzer (PrismaPro QMG 250 F1) is installed to measure the residual gas composition in the vacuum system. Its covers a detectable mass range of 1-100 atomic mass units (amu) with a detection threshold of $4 \cdot 10^{-13}$ mbar. Knowledge about the background gas composition is essential for the estimation of the induced frequency shift (Sec. 3.5.4).

The strontium oven section is separated by a gate valve from a 40 cm long tube attached to the main chamber. Around the tube the tapered solenoid Zeeman slower is assembled. The gate valve allows to seal the oven part from the main vacuum chamber when the oven gets refilled.

In between the oven and the valve, a 6-way cross is installed. Through a CF-40 viewport it allows observation of fluorescence from the atomic beam when the Zeeman slower laser is active. This is a quick and easy way to verifying if the Zeeman laser works properly or if the atomic beam is present. Two other ports of the 6-way cross hold the atomic beam shutter and its heat shield (Sec. 3.2.7. On the last port a 45 L/s ion pump is installed for differential pumping. The gasket at the oven/6-way connection has a 2 mm diameter aperture only to minimize strontium vapor deposition into the vacuum system. The gasket between the gate valve and the 6-way cross has a 10 mm diameter aperture and protects the gate valve from pollution with strontium vapor. The oven is mounted into a port aligner (Hositrad HMC1000) with XY manipulator allowing a travel range of ± 12.5 mm and a tip-tilt range of $\pm 2°$.

At the top of the main chamber two CF16 ports are designated to implement the cryogenic atomic beam shutters. The cryogenic atomic beam shutters block any direct line of sight from the atoms to the oven or outside room temperature BBR. Thus suppressing the BBR shift during spectroscopy. They are part of the cryostats concept to minimize the BBR shift uncertainty but at the time this manuscript was written they have not been implemented. More about the influence of the missing cryogenic beam shutters on the BBR shift uncertainty can be read in Sec. 3.2.6.

To compensate for any stray magnetic field either from earth or from laboratory equip-

ment a set of three orthogonal pairs of magnetic field coils in Helmholtz configuration is installed at the experiments framework. Each pair consists of two identical coils, electrically connected in series and can be separately addressed via a current sink controlled by a ramp generator that can be programmed by the experimental control program. The Helmholtz field of every coil can be varied in every individual step of the experimental cycle pattern.

Pulse tube cooler

To cool the cyrostat to its operational temperature to about 77 K a closed cycle pulse tube cooler (PTC) is installed near the vacuum system (Thales cryogenics LPT9710 with Chroma 61602 AC power supply) into the framework. The feed trough for the cold finger of the PTC required a Helicoflex seal (supplied by Technetics Group) instead of a copper gasket. It never turned out to be a limitation in achievable vacuum pressure at any operational temperature. The pulse tube cooler is actively water cooled by copper pipes winded around its heat dissipating parts. A flow sensor in the water cooling circuit monitors the water flow and will switch off the pulse tube coolers power supply in case of cooling water flow failure to prevent the pulse tube cooler from taking damage from overheating.

Optical access

The vacuum system offers several viewports for optical access for all relevant laser beams. All relevant beams apart from the horizontal MOT beams are depicted in Fig. 3.1. The Zeeman slower beam is implemented counter propagating to the atomic beam at the opposite side of the oven. Two of the three MOT beams are fed in from the bottom at an angle of 45° against gravity and are retro reflected at the opposite side of the chamber. The third beam is directed trough the MOT coils at the front CF-160 flange. Their free aperture of about 18 cm is quite large but severely shaded by the inner aperture of the MOT coils of only about 20 mm. The retro reflected detection beam and the beams for spin polarization are passing trough them at a slight angle of approx. 15° to the coils axis.

Close to the retro-reflector of one of the MOT beams the repump laser beams enter the chamber. The beams of both lasers are coupled into the same FC-APC fiber by superimposing them with a polarizing beam splitter on a compact distribution board similar to the one described in Sec. 4. At the opposite side of the chamber a mirror allows to retro reflection the beams.

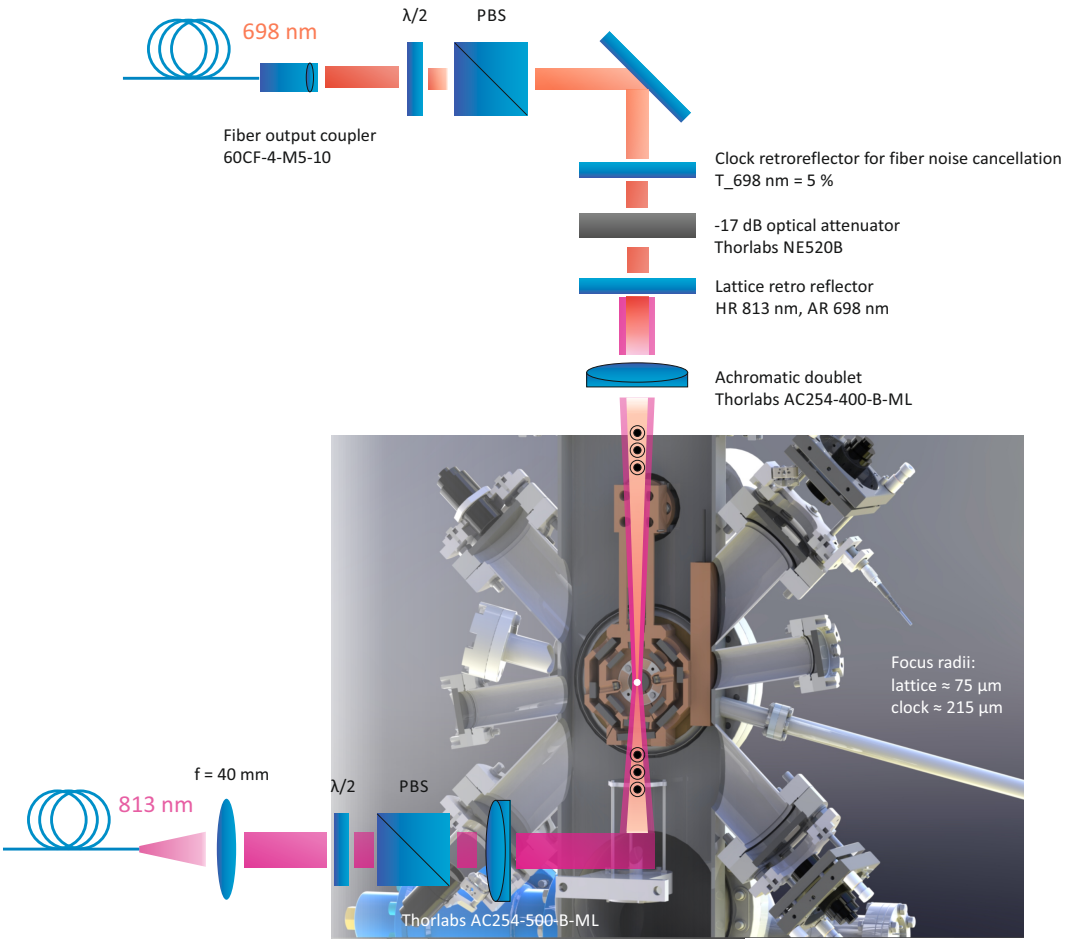

Figure 3.2.: Schematic of the lattice and clock laser propagation. Both beams are delivered via FC/APC fiber and form $1/e^2$ focus radii of 75 µm (lattice) and 215 µm (clock) at the position of the atoms. The parallelism between lattice and clock laser beam is better than 0.3 mrad.

3.1.2. Lattice and clock laser beam delivery

In Sr3, the orientation of the lattice was chosen vertical. This greatly suppresses tunneling as discussed in Sec. 3.5.10 and allows to operated at lower potential depth that in turn reduces the lattice light shift uncertainty. The light from the lattice laser is transported via a 10 m long polarization maintaining large-Mode-Area Photonic Crystal Fiber (AL-PhANOV LMA-PM-15) to the vacuum chamber. A robust cage system is attached to the vacuum chamber that holds several optomechanics for beam shaping and polarization control (Fig. 3.2).

After the lattice fiber an $f = 40$ mm lens collimates the lattice beam to a diameter of

approx. 2.8 mm and passes a rotatable waveplate that aligns the polarization of the lattice to that of the PBS. To create a diffraction-limited focus with minimal optical aberrations a pair of achromatic doublets (Thorlabs AC254-500-B-ML, AC254-400-B-ML) are used to form the lattice focus where the atoms will be trapped into.

After the first doublet, the lattice beam enters the chamber through a CF-40 viewport at the front of the chamber and is reflected upwards by an in-vacuum fold mirror. The beam propagates vertically thorough the cryostat and exits the vacuum chamber through a CF-40 viewport at the top CF-200 flange. There another cage systems is mounted to the vacuum chamber. It holds the relevant optics for lattice retro reflection and for the alignment of the clock laser beam and its polarization control.

The lattice laser is re-collimated by the other doublet (Thorlabs AC254-400-B-ML) retro reflected by a highly reflective (HR) mirror. This mirror is also highly transmissive for clock laser light at 698 nm. The clock laser light is delivered by an polarization maintaining single mode fiber from the clock laser in the neighboring laboratory. The output coupler collimates the clock beam to diameter of approx. 1 mm. A retro reflector with only 5% transmission at 698 nm reflects most of the light back trough the fiber which forms one arm of an interferometer that is used to stabilize the optical phase of during spectroscopy [64]. After the clock laser retro reflector the optical power is reduced by a gray filter with an optical attenuation of approx. -17 dB. The aromatic doublet then focuses the clock laser to the same position as the lattice. The foci were measured with a beam profiler camera (Cinogy, CMOS-1201-Pico (1/2.5")). The clock laser waist radius is measured to $w_{0,698\ nm} = 215\,\mu\text{m}$ which is about four times larger than the lattice focus of $w_{0,813\text{nm}} = 75\,\mu\text{m}$. This minimizes inhomogeneities of the Gaussian probe beam intensity profile that the atoms experience.

Both foci overlap with a displacement better than 10 µm and a parallelism below 0.3 mrad. Great care must be taken in the beams parallelism otherwise the line contrast will degrade as described in [35,39]. This effect increases with stronger misalignment of the probe with respect to the lattice axis. The polarization of the lattice and the clock laser are aligned nearly parallel in the horizontal plane and pointing along the quantization axis given by the magnetic field of the MOT coils.

Two enhancement cavities are foreseen for potential future installation. The first one inside the cryostat (Fig. 3.2) that allows the study of higher order lattice light shifts

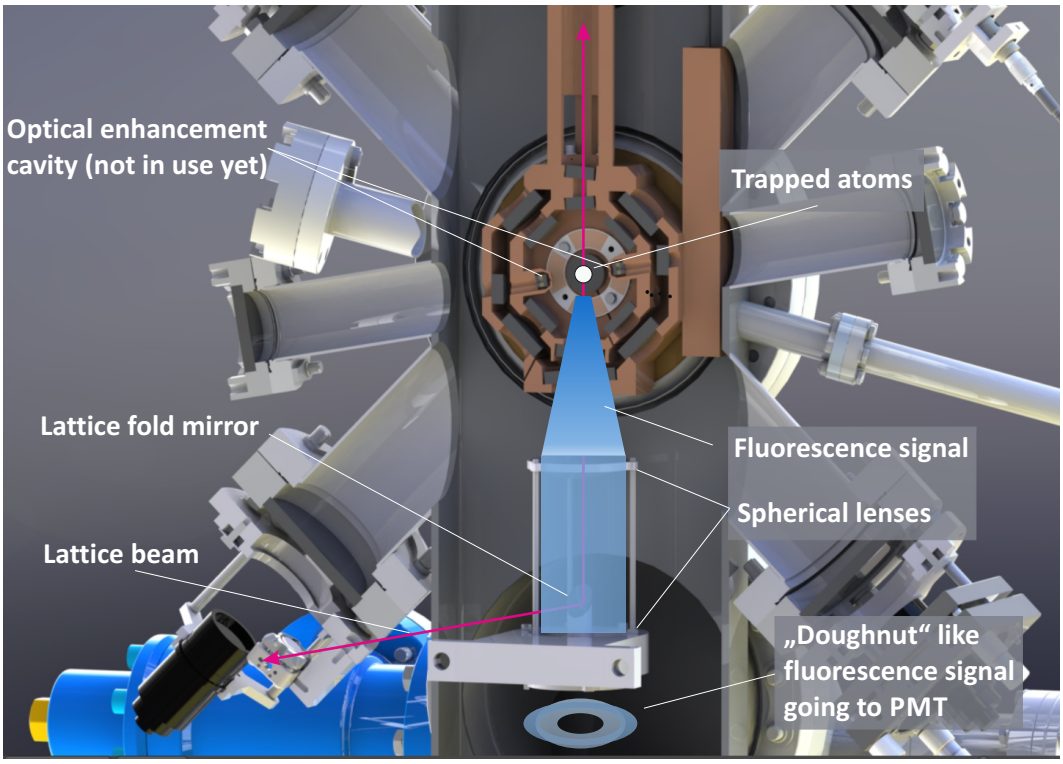

Figure 3.3.: View on the inside of the Sr3 physics package. Due to the fold mirror for the lattice that is placed between two lenses that collect fluorescence signal for the state detection the detection beam has a dark spot in the middle. The optical enhancement cavity is not in use yet.

as well as a non destructive detection [73, 74]. Another one outside the vacuum system enhances the vertical lattice and allows the study of higher order light shifts such has the E2/M1 shift and hyperpolarizability.

3.1.3. State detection optical imaging system

To detect the atomic state, Sr3 relies on the same destructive fluorescence state detection scheme as Sr1 [62]. Three consecutive pulses resonant to the $^1S_0 - ^1P_1$ transition determine the number of atoms in the ground- $|g\rangle$ and excited state $|e\rangle$ followed by a background signal calibration. The light scattered from the atoms (Fig. 3.3) is collected and collimated by an in-vacuum customized AR coated spherical lens (50.8 mm diameter, 100 mm) with a central hole of 10 mm diameter. The central hole is required for the lattice laser beam to pass trough. The collected light from fluorescence is thus shaped like a ring looking

similar to a LG_{01} mode or "doughnut-mode". An additional in-vacuum f=400 mm lens focuses the light that is exiting the vacuum system trough the bottom CF-63 viewport. An adjustable fold mirror directs the light towards the gated photo multiplier tube (PMT). By an additional f=50 mm lens the images on the PMTs active detector surface was optimized. An optical bandpass filter (Thorlabs FL460-10) that has a passband around 460 ± 2 nm and a transmission window of width FWHM $= 10 \pm 2$ nm blocks any parasitic radiation in the range of 200 nm $-$ 1100 nm. This minimizes the background signal from e.g. stray light. Within this imaging system, several apertures reduce stray light that is contributing to the background signal. On the entire optical path, all components are colored in varnish black where possible. The PMT produces an output current of $I_{max} = 100$ µA that is amplified to a voltage ranging from $0-10$ V for typical experimental conditions. The output signal of the amplifier is connected to one of the analog input channels of the experimental control system where it is processed and converted into and arbitrary number of "counts".

3.1.4. Experiment control system

The experimental control program is based on the commercially available software LABVIEW. It was adopted from the team operating the Sr2 transportable clock where my college Stefan Vogt did a great job in further developing the software that was initially developed from the group of Carsten Klempt at the university of Hannover. He described it in great detail in his work [33]. With the FPGB (field-programmable gate array) based hardware the experimental control system enables a large variety of functionality. A serial port interfaces allow communication with external devices such as Direct Digital Synthesizers (DDS) and ramp generators.

In total 80 individually programmable transistor-transistor logic (TTL) output channels as well as eight analog input and eight analog output channels are available for communication with external devices. At the moment approximately half of the TTL output channels are used to run the clock. The integrator error signal of the frequency lock of the lattice-, 461 nm- and 689 nm laser are connected to analog input channel to monitor their status online for potential user intervention. The detected signal of the PMT is connected to an analog input channel. The experimental control program converts its voltage signal to the arbitrary unit "counts" that is proportional (but not yet calibrated) to the number

of detected atoms. For each channel a pre- and post delay can be programmed which is very convenient to account for time delays in the addressed devices such as a mechanical beam shutter. In our experiment the control system addresses six ramp generators to steer the current in the compensation magnetic coils, the spectroscopy lattice depth of an interleaved measurement and the bias magnetic field forming the quantization axis for the atoms.

3.1.5. MOT coils

The magnetic required during the two MOT stages, state preparation and spectroscopy is generated by a pair of custom build coils. Its design was adapted from our transportable clock Sr2 [33] which proved to be reliable even during field operation. They are installed outside the vacuum system in two 140 mm diameter viewports of a CF-160 flange (Fig. 3.1 and Fig. 3.5). The TTL addressable electric circuit design allows to operate the coils either in Helmholtz or anti-Helmholtz configuration. During the MOT stages the coils are operated in anti-Helmholtz configuration to provide a field gradient at the center. During state preparation and spectroscopy (Sec. 2.5) it is operated in Helmholtz configuration producing a homogenious field at the place of the atoms that establishes the quantization axis.

Generating the required magnetic field during the blue MOT phase requires the largest current the system requires of 50 A. The coils electrical resistance was measured to be 24.4 mΩ and 25.6 mΩ resulting in an electrical average power consumption of 125 W. Even at a duty cycle below 50%, which is typical during clock operation, their thermal load is still high and causes severe heating of the coils and their surroundings. To dissipate the heat efficiently water cooling is required. Considering to place the coils as close as possible to the atoms at the inside of the cryostat to reduce the heat dissipation, any heating of the coils will be a handicap for cryogenic operation and of course introduce a BBR frequency shift on the atoms. Placing the coils outside of the vacuum chamber circumvents this problem and allows a non vacuum compatible design which reduces complexity. In Sr3 this approach was followed. The coils are made of hollow wire for cooling water flow. The winding scheme directs the cold water intake to supply such windings first that are closest to the vacuum chamber. In that way, heat transfer from the coils to the vacuum chamber is minimized.

To measure the coils magnetic field they have been operated at a test bench. They were placed at a distance of 86 mm which is equal to their final distance when assembled to the Sr3 vacuum system. The coils axial magnetic field, denoted as the z-axis, was measured with an axial hall probe (Magnet-Physik HS-AGB5-4805). They were tested in anti-Helmholtz configuration at 20% of the design current since no water cooling was available at that time. According to the Biot–Savart law the on-axis magnetic field depends linear on the electric current, thus one can expect a 5 fold increase in the magnetic field when operated at the design current of 50 A. Fig. 3.4 shows the measured magnetic field recorded at a current of 10 A multiplied by a factor of 5 to estimate the magnetic field at the design current of 50 A.

The center field gradient is about 0.1 mT/cm, which is only 75% of the gradient compared to [33]. It is likely that our coils suffer from a short circuit occurred during the manual manufacturing process, effectively reducing the number of coil windings and thus the maximum magnetic field. The electrical resistance of the identical reference coils from the transportable clock are approx. 30 mΩ which is significantly higher. This supports the theory of reduced windings due to short circuits.

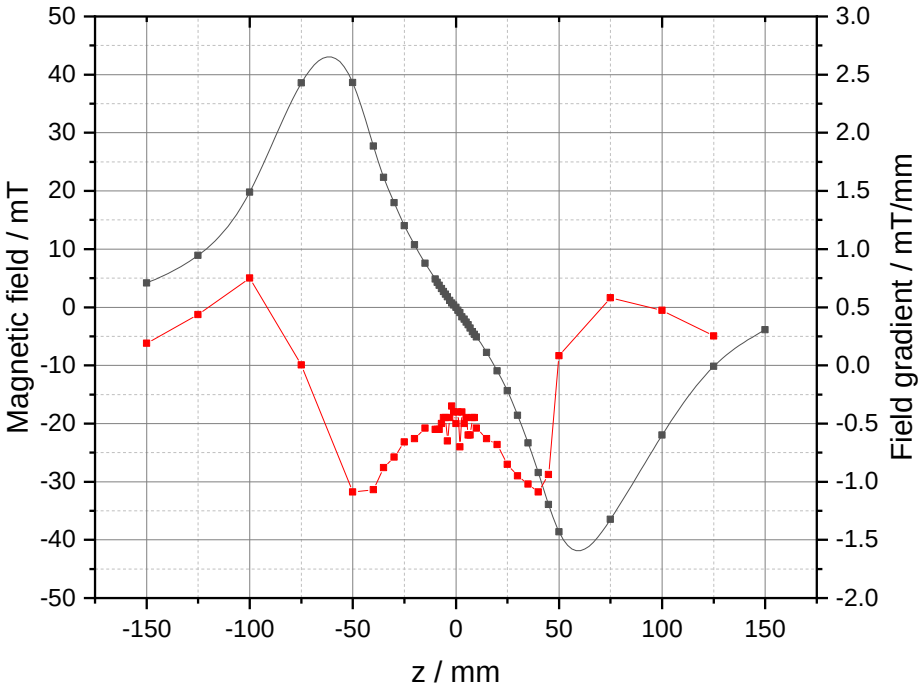

Figure 3.4.: Axial magnetic field generated by the MOT coils in anti-Helmholtz configuration. The measurement was performed at an electrical current of 10 A and up scaled to estimate the magnetic field at the design current of 50 A. The center gradient of the coil arrangement is 0.1 mT/cm at 1 A of current.

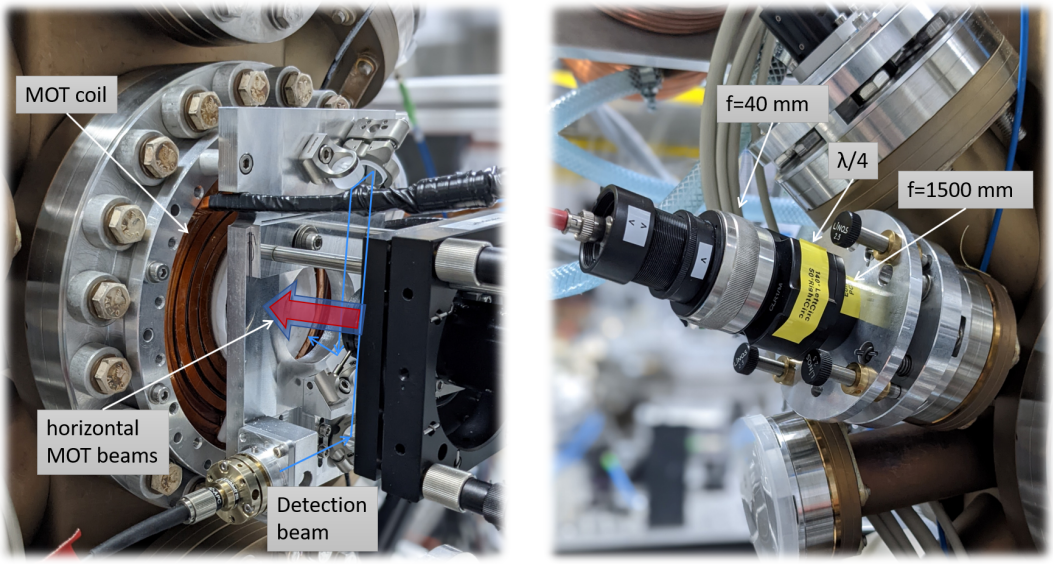

Figure 3.5.: Photograph of one of the MOT coils (left) installed in Sr3. The aluminum mounting plate holds the fiber output coupler and beam delivery mirrors for the detection beam and the output coupler of the superimposed horizontal blue and red MOT beam and aligner. For the Zeeman slower beam an alignment tool similar to a conventional mirror mount is installed directly to the CF-40 flange. It allows full beam alignment (lateral and tip-tilt) as well as full polarisation control via rotation of the fiber end and a rotatable $\lambda/4$ waveplate. The f=40 mm collimation lens can be adjusted in the beam propagation direction for optimizing the beam diameter with respect to the atomic beam size.

3.1.6. Zeeman slower

The first step in the process of preparing the atoms for spectroscopy is to capture them from the oven into a 3D magneto optical trap (MOT). The most common way is to use an evaporative oven as atomic source and decelerating the atoms by using a Zeeman slower. A different technique is laser ablative loading [75, 76], which is not part of this work. The principle of decelerating atoms with a Zeeman slower has been discussed in Sec. 2.1.1.

In Sr3 at an oven temperature of approx. 500 °C the included strontium is evaporated. Capillaries at the oven's exit form an atomic beam. An additional aperture of 2 mm diameter in approx. 23 cm distance from the oven, reduces the divergence of the atomic beam.

Light from a frequency stabilized ECDL is delivered through an FC-APC fiber from a laser distribution board to the experiment. In the distribution board a fraction of the light from the ECDL is rerouted and used for frequency control and frequency monitoring. The laser is operating near the ${}^1\mathrm{S}_0(F = 9/2) - {}^1\mathrm{P}_1(F' = 11/2)$ transition at 461 nm is coupled into the vacuum chamber opposite to the oven, counter propagating to the traveling atoms (Fig. 3.1 right). A mechanical mount at the CF-40 flange allows transverse and angular alignment of the optical beam (Fig. 3.5). The required optics are mounted into a robust short lens tube system.

After the fiber the beam diverges to 6 mm in diameter before it is collimated by an adjustable f=40 mm lens. An $f = 1500$ mm lens focuses the beam all along the Zeeman slower to a diameter of approx. $2w(z = 1065\mathrm{mm}) = 2$ mm at the capillaries of the atomic oven. For fine adjustment of the overlap between the optical- and the atomic beam the collimation lens is adjustable along the propagation axis which influences the beams caustic. The fiber holder and a following $\lambda/4$ plate are rotatable offering full polarization control.

The first approach for a Zeeman slower was based on a longitudinal field design based on spherical permanent magnets [77]. Measurements of the longitudinal magnetic field profile along the Zeeman slower axis turned out to be not ideal which is why we did not continued to follow such a concept. We decided to go the more flexible way for Sr3 and use a coil based slower that delivers a longitudinal magnetic field. For the lab based system it was not difficult to construct a water cooling system. It was shared with that of the

MOT coils.

Target parameters

At a typical oven temperature of about 500 °C the most probable velocity of the atoms is approx. 450 m/s (Eq. 2.1). This corresponds to a Doppler frequency shift of $\Delta\nu_{Doppler} = -977\,\mathrm{MHz}$ from the atomic $^1\mathrm{S}_0 - {}^1\mathrm{P}_1$ transition frequency at rest. To compensate the Doppler shift with the Zeeman effect, a magnetic field of approx. $B_0 = 70\,\mathrm{mT}$ is required.

In our design, we requested a final velocity of the atoms $v_{ex} = 50\,\mathrm{m/s}$ which is typically slow enough to capture the atoms in the first MOT stage.

The full extend of the slowing length is 253 mm given by the available length of the vacuum tube. An offset magnetic field of approx. $B_{off} = -38\,\mathrm{mT}$ was introduced that corresponds to a frequency detuning of the unperturbed transition frequency of $-535\,\mathrm{MHz}$ which is easier to bridge by frequency shifting acousto optical modulators (AOM). But this leads to a zero crossing of $B(z)$ (Fig. 3.6) and a change in sign. To remain $B(z)$ following the target field an additional coil is required that is called "auxiliary" in the following. The other is denoted as "main"-coil. The design currents are 6.2 A and 2.7 A for the main and auxiliary coil which causes a thermal heat load of 66 W in total that is dissipated by the same water cooling cycle of the MOT coils.

Slower's magnetic field, Doppler spectra

At the electrical design currents given above the slower's longitudinal field $B(z)$ was measured with the same longitudinal hall probe as that of the MOT coils. The result can be seen in Fig. 3.6. The measured magnetic field is in excellent agreement with the simulation and matches the target field.

To test how the Zeeman slower performs in the deceleration of atoms, their velocity distribution is measured using Doppler spectroscopy. Therefore, an additional probe beam is fed into one of the available MOT viewports (Fig. 3.1) to probe the traveling atoms at the position of the MOT. The angle between the atomic beam and the probe beam is 61.5°, which allows to determine the Doppler shifted resonance frequency of the atoms in the atomic beam. The radial velocity of the atoms in the collimated atomic beam is expected to be close to 0 m/s so an additional laser beam probing the atoms perpendicular to their direction of travel can determine its resonance frequency at rest as a reference. Due to the

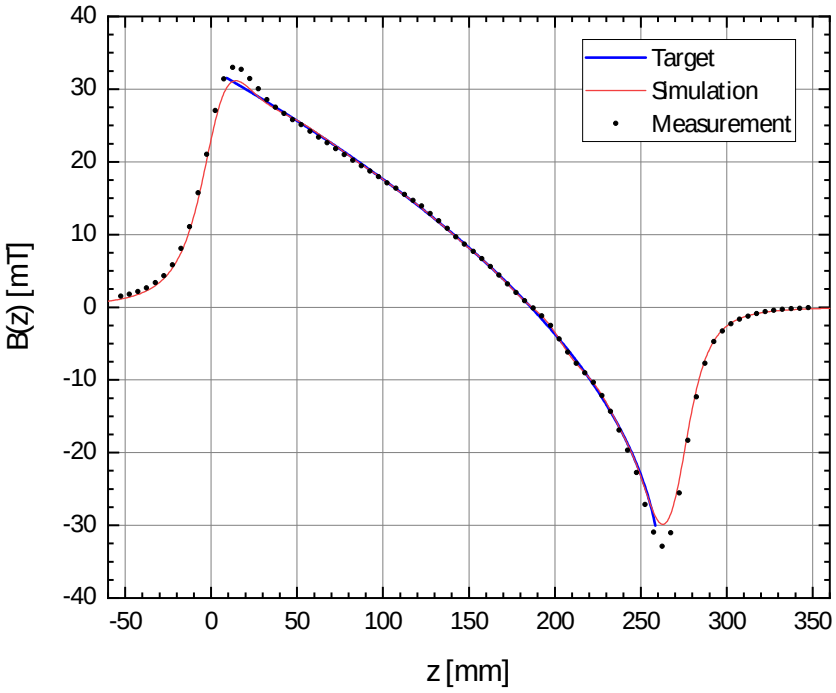

Figure 3.6.: Measured magnetic field (black dots) along the Zeeman slower's z-axis. The target field (blue solid line) and the simulated field of the design (red solid line) described in the text are in good agreement. The measured magnetic field is slightly deviation at the extremes of the target field, but apart from that in excellent agreement.

known angle of the probe beam fed into the MOT viewport, the resonance frequency can simply be corrected for the Doppler effect without the need of the perpendicular probing beam. All further results in the text are corrected for the corresponding Doppler shift. The fluorescence signal of the atoms is detected by the state detection system (Sec. 3.1.3). Since the PMT was not available at the time of the measurement a CCD-Camera was used instead. It produced a signal in the arbitrary unit "counts", proportional to the fluorescence signal of the atoms.

The laser beams for the Zeeman slower and the probe beam are delivered from two different ECDL's. The Zeeman laser is frequency stabilized to a cavity-stabilized laser that only serves that purpose. To monitor the frequency detuning between the Zeeman laser and the probe laser, a fraction of their power is used to create a beat note on an avalanche photo detector (APD, Thorlabs APD210). Their beat note is monitored on a spectrum analyzer while the probe beam was scanned. Its scanning range was approx. 1.4 GHz to cover the full velocity distribution of the atomic beam. From the frequency of the beat note the axial velocity of the atoms is derived.

The measurement result is shown in Fig. 3.7. The reference measurement without active Zeeman slower (without light and without magnetic field) serves as reference. Its peak velocity is at about 435 m/s, which is in good agreement to the expected 450 m/s calculated with Eq. 2.1. The slight deviation is suspected to be caused by a temperature offset between the temperature sensor and the strontium inside the oven. The colored measured velocity distributions in Fig. 3.7 represent measurements at different laser frequency detunings from resonance ranging from −793 MHz to −632 MHz. Atoms can be decelerated velocities ranging from approx. 700 m/s to about 50 m/s (see inset in Fig. 3.7). At all detuning frequencies measured (colored lines in Fig. 3.7) deceleration was observed, where larger frequency detunings produce greater signals at the corresponding peak velocity.

Since the probe laser is not frequency stabilized during every frequency scan its frequency drift leads to a offset that transfers to an error in the determination of the velocity distribution of the atoms. The error bars for the peak velocity in the inset in Fig. 3.7 attribute this issue. The error was obtained by observing the probe laser frequency difference before and after such a frequency scan. The frequency detuning of the Zeeman slower laser has been determined by the frequency of the beat note and the frequency of

the probe laser read from a wavemeter. The width of the beat note was about 5 MHz which is attributed as the uncertainty in the frequency detuning of the Zeeman slower laser.

Since the atomic beam ends at the viewport where the Zeeman slower laser beam is entering the chamber, a certain amount of Sr atoms will hit the optical surface and stick to it. After build up of a layer of deposited strontium on the optical surface, it will become opaque. This has been experimentally investigated by [78]. Based on their results the atomic flux in Sr3 is estimated to be $1.9 \cdot 10^{11}$atoms/s cm^2 at an oven Temp of 500 °C. The resulting growth rate is 0.38 nm/h. We define the "lifetime" of the viewport as time elapsed for a loss in transmission of 50% at a given growth rate. For our case it is expected to be about 1800 h (77 days) of continuous operation. The lifetime also scales inverse with the vacuum pressure. The lower the residual gas pressure the shorter the lifetime will be. The presence of water in the residual gas will counteract the buildup of strontium by reacting to $Sr(OH_2)$ which is transparent at 461 nm. In Sr3 this problem occurred already. A layer of deposited strontium was clearly visible and had a strong negative effect on Zeeman slowing of the atoms which exhibited in a poor loading efficiency into the blue MOT. The layer was obviously thick enough to decrease the optical transmission. The viewport used here is an AR coated sapphire window that minimizes strontium vapor deposition. It was exchanged and the loading efficiency of the blue MOT was recovered. The observed lifetime cannot be states with certainty since this is not a documented parameter but from personal feeling it is in marginal agreement with the predicted lifetime. The deposited strontium on the exchanged viewport could be removed by cleaning the surface with deionized water.

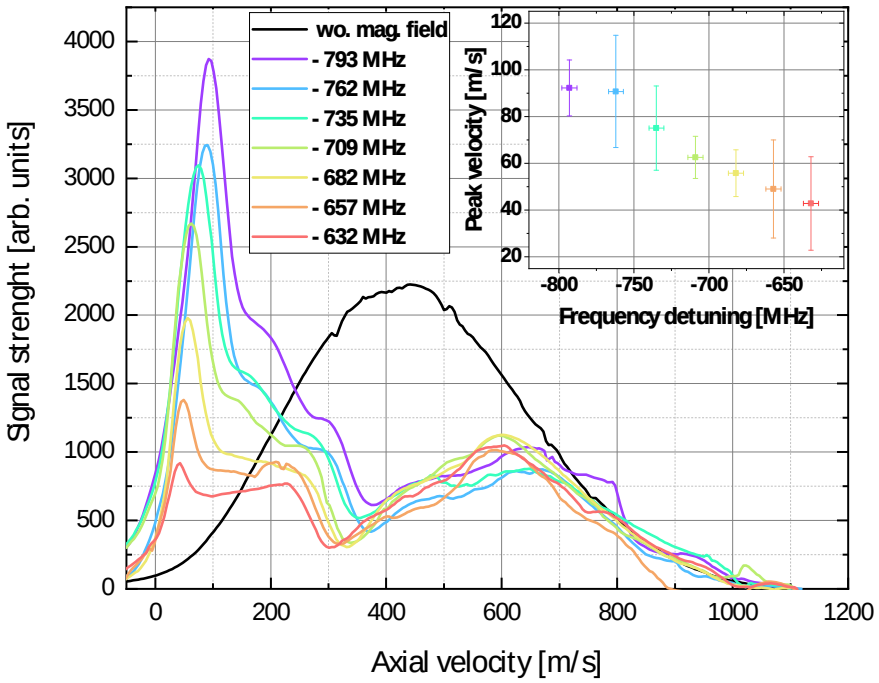

Figure 3.7.: Measured Doppler spectra with Zeeman slower at different laser detunings (colored lines) and without (black). Atoms with velocities of up to approx. 700 m/s can be decelerated with our Zeeman slower to final velocities ranging from 90 m/s down to about 40 m/s. The inset shows the peak of the velocity distribution of the decelerated atoms at the given detuning. The experiment was performed by using ^{88}Sr due to the greater the natural abundance of that isotope that gives a greater measurement signal. The results can be adapted directly to ^{87}Sr since their properties regarding laser cooling is similar. Error bars in the inset attribute the laser frequency drift that translates into an error in the determination of the atomic velocity. The uncertainty of the detuning arizes due to the uncertainty of the Zeeman slower lasers frequency which has been determined by the frequency of the beat note that has a width of approx. 5 MHz.

3.2. Reducing the black body radiation shift uncertainty

Operating a Sr-lattice clock at cryogenic temperatures substantially relaxes the requirements on the exact knowledge of the representative temperature and the resulting frequency shift of the clock transition. This is a common approach to tackle the black body radiation shift uncertainty in lattice clocks [57, 79, 80]. In Fig. 3.8 the relationship between operating temperature and BBR shift uncertainty for different uncertainties is shown. Decreasing the operational temperature results in a dramatic improvement in shift uncertainty even if one has to accept higher uncertainty (e.g. due to decreasing temperature homogeneity) of the temperature to a certain extent. When operating a Sr-lattice clock at room temperature the knowledge of the atomic response to the BBR field is the limiting the fractional uncertainty of the BBR shift to approx. $1 \cdot 10^{-18}$ [46]. The commercial availability of closed cycle coolers (e.g. pulse tube coolers) allow operational temperatures of approx. 77 K. A cryogenic clock without the need for refilling liquid nitrogen and the required supply logistics is hereby an advantage. In the following sections the cryogenic environment, the dual layer cryostat that represents the core of the new Sr3 clock, and its impact on the BBR frequency shift uncertainty is described.

3.2.1. Cryostat

Previous attempts to reduce the BBR shift uncertainty in Sr1 relied upon atomic transport into a liquid nitrogen cooled environment [57]. Therefor the optics forming the optical lattice were placed on translation stages to transport [81] the ultracold spin polarized ensemble for about 45 mm into the coldfinger for spectroscopy under cryogenic temperature conditions. The duration for the atomic transport was about 350 ms and lead to a loss of atoms of about 10%. Additionally the transport induced vibrations resulted in an additional first order Doppler frequency shift of $5.5(8) \cdot 10^{-17}$ [57]. To circumvent theses issues, Sr3 features an all cryogenic design based on a dual layer cryostat that offers good temperature homogeneity and thereby enables a BBR shift uncertainty in the low 10^{-18} range even when operated at room temperature. The core design of Sr3 is based on an in-vacuum dual layer cryostat made of OFHC copper (Fig. 3.9). This material offers good thermal- and electric conductivity which makes it a suitable candidate for applications at cryogenic temperatures. The temperature of the cryostat can be lowered ranging from

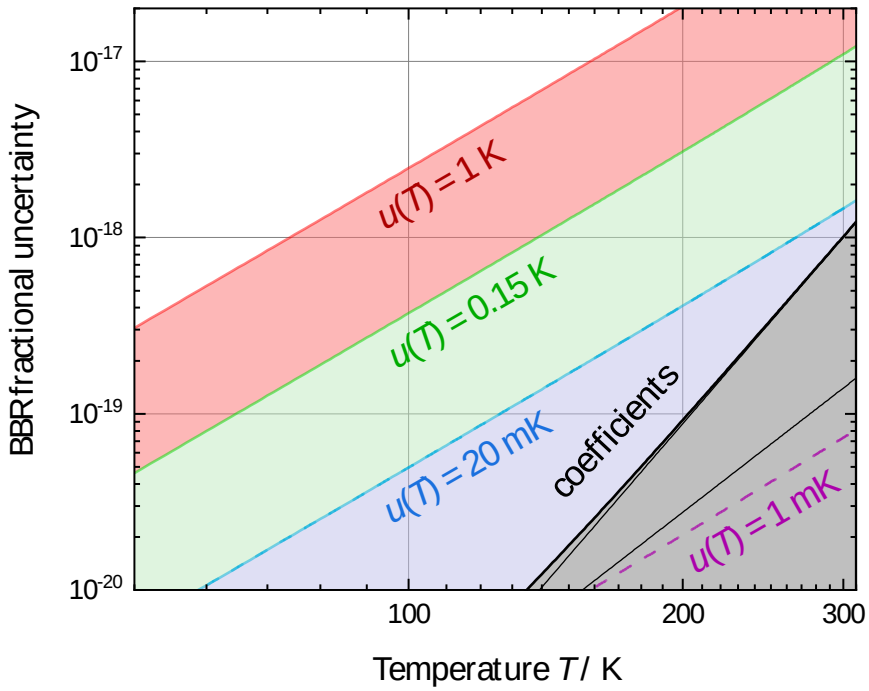

Figure 3.8.: Fractional uncertainty of the BBR frequency shift due to the uncertainty of the representative temperature T and the atomic response coefficients $\Delta\nu_{stat}$ and $\Delta\nu_{dyn}$ as a function of absolute Temperature. Operation near room temperature with an uncertainty of 20 mK of the representative temperature the limiting factor is the knowledge of the dynamic coefficient α_{dyn} in the atomic response to the BBR field. During clock operation at room temperature an uncertainty of approx. 20 mK of the representative temperature was achieved, and approx. 150 mK when operating near 80 K. This figure includes the revised contribution of $\Delta\nu_{dyn}$ from [46].

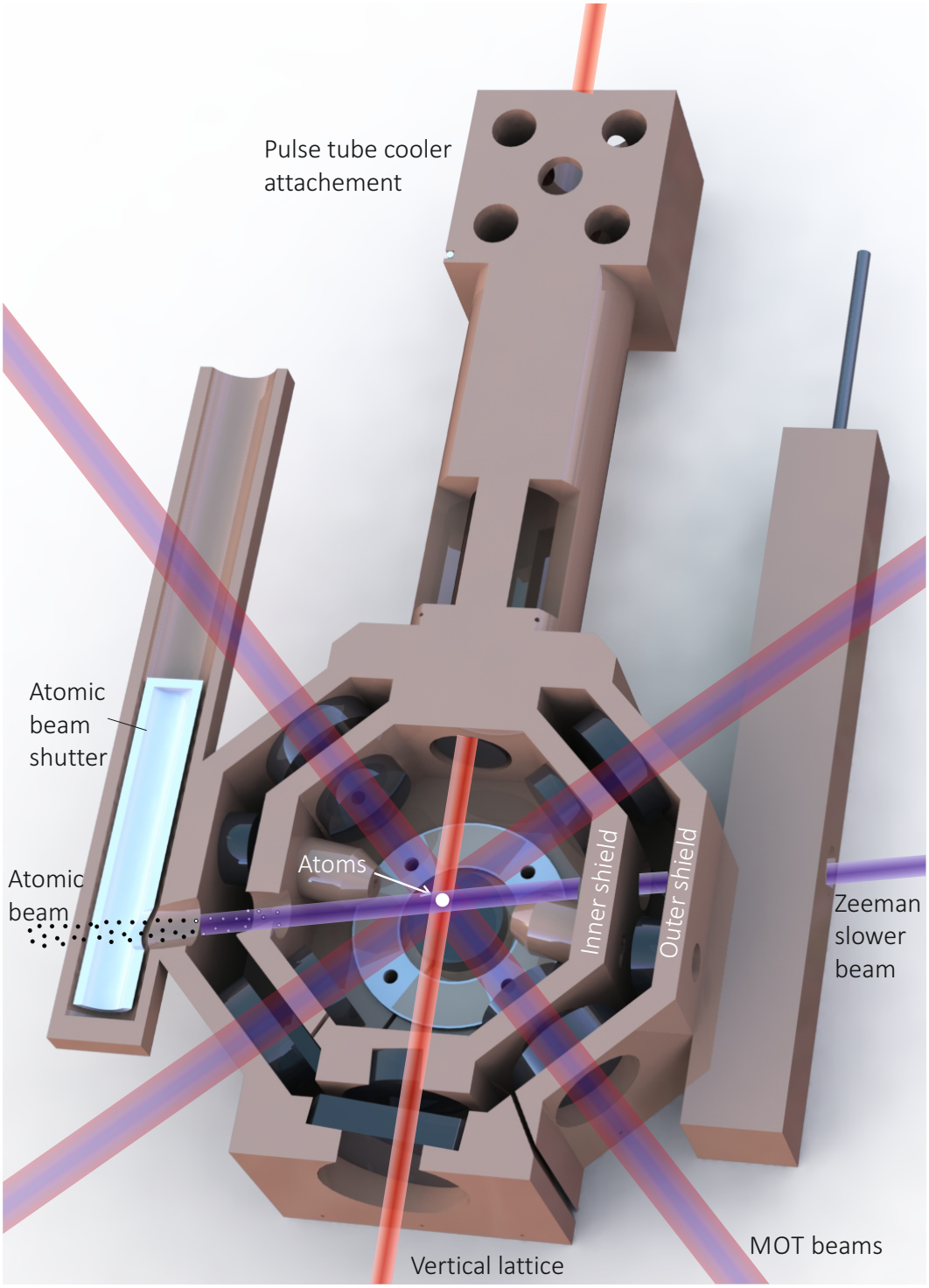

Figure 3.9.: Dual layer in-vacuum cryostat. The design shields the atoms greatly from BBR and offers excellent temperature homogeneity offering a BBR uncertainty at the low 10^{-18} level at room temperature and about an order of magnitude better at cryogenic temperature. The inner shield is painted black (not shown) to prevent the build up of a BBR field. During cryogenic operation at approx. 80 K the atomic beam shutters (not installed yet) block the direct line of sight from the atoms to the outside. This prevents intruding room temperature BBR to cause a frequency shift and an uncertainty contribution.

room temperature to below approx. 70 K by the closed cycle pulse-tube cooler. The cryostat also works as a Faraday cage to protect the atoms from outside electric fields. The surface of the cryostat is reflecting thus owing a small emissivity factor that minimizes absorption of thermal photons. Before installation it was stored in a sealed environment filled with nitrogen to prevent oxidation and maintain its surface reflectivity. Intruding BBR is therefore mostly reflected by the surface. The inside of the inner shield is coated with several layers of Aquadag. A special dispersion of colloidal graphite in purest water with a very high emission factor. Any BBR photon that enters the inner shield will mostly be absorbed by this surface. To date the cryogenic atomic beam shutters are missing. They are supposed to be implemented through the hollow nacelle structure at both sides of the cryostat (Fig. 3.9). Two CF-16 flanges at the top of the vacuum chamber are foreseen to mount them on rotatable feed throughs. This allows to alter the shutters state. Without physical contact to the body of the cryostat, the shutters temperature follows that of the cryostat due to radiative coupling. nevertheless the structure will be mounted on rotatable rods at the top CF-16 flanges of the vacuum chamber causing a certainty heat intake. This will be investigated when the shutters are being assembled into the clock. It is expected that their temperature deviates from that of the cryostat at cryogenic temperatures. In a thermal simulation, the shutters reached a temperature of 130 K at a cryostat temperature of about 80 K. Once the shutters are installed their temperature has to be verified in the running experiment. The influence on the BBR shift uncertainty is discussed in Sec. 3.2.6 and can also be seen in Fig. 3.25 in Sec. 3.5.3.

Since an optical enhancement cavity is not implemented in the inner shield yet, its hollow mounting structure is sealed with copper covers that are coated with Aquadag too. This prevents additional leakage from outside room temperature BBR during operation.

As partially depicted in Fig. 3.9, a symmetric arrangement of two ceramic ring structures (one not shown) are mounted in the inner shield close to the atoms. These are holding the electrodes for the dc Stark shift measurements. A more detailed description of them as well as the determination of the dc Stark frequency shift and its uncertainty can be found in Sec. 3.4.

During the blue MOT phase, by far the largest current is switched on to the MOT coils to create the magnetic field gradient necessary. The switching of such large current induces eddy currents into the electrically conducting cryostat. After the relatively fast switch-off

of the MOT coils current (5 ms), the eddy current in the cryostat will start to decay over time. This causes unstable conditions for the splitting frequency of the outermost $m_F = \pm 9/2$ magnetic sublevels. To prevent this a slit in both layers of the cryostat (Fig. 3.9) suppresses the buildup and decay of such currents. To minimize intruding BBR the slits are displaced to each other.

Optical access and BBR absorption characteristics of N-BK7 windows

The two cryostat layers feature a total of 16 windows for optical access of the relevant laser beams (Fig. 3.9). The windows are fabricated from N-BK7 and received a dielectric AR-coating for the particular laser wavelengths. The two apertures for loading the atoms and the Zeeman slower do not have such windows. The apertures that let the counter Zeeman slower laser beam enter the chamber are not covered by a window since any deposition of strontium vapor there would require to remove the cryostat from the main chamber for cleaning which is quite complex.

The optics are attached to the cryostat with a 2 mm thick ring of indium. It provides sufficient adhesion when the optics are squeezed to the surface of the cryostat. Any glue would most likely outgas which is extremely unwanted this close to the atoms since the residual gas can cause frequency shifts (Sec. 3.5.4). Typically, baking of adhesives reduces their final outgasing rates. But in order to maintain the highly reflecting unoxidized surface of the cryostat, baking would require to happen which is not possible in Sr3. Indium on the other hand does not affect the vacuum pressure and is an approved material to contact optics to metals such as aluminum or copper. Despite the difference in thermal expansion coefficients of the copper/indium/BK7 combination ($17/44/7 \cdot 10^{-6}$/K) during all performed temperature cycles no failure was observed proving this is a reliable approach.

The main purpose of the windows assembled to the cryostats outer- and inner shield (Fig. 3.9), is to absorb room temperature BBR and prevent it from entering the inner shield. The windows are made of N-BK7 that combines transparency at the frequency range relevant for laser cooling and trapping, as well as absorption characteristics in the spectral range of room temperature black body radiation. The advantage of N-BK7 is a significantly lower transmission at frequencies below 1 THz compared to e.g. fused silica that is often used for similar optics [82]. Based on the work presented in [57] the transmission through 12.7 mm of N-BK7 is calculated. In Fig. 3.10 the BBR spectral density at a temperature of 20 °C (gray semicolon line) and its transmission through 12.7 mm of N-BK7 (red solid line) as a function of frequency is shown. In the determination of the frequency shift the polarizability of the three lowest lying transitions $(5s^2)^1\mathrm{S}_0-(5s5p)^1\mathrm{P}_1$, $(5s5d)^3\mathrm{P}_0-(5s4d)^3\mathrm{D}_1$ and $(5s5p)^3\mathrm{P}_1-(5s6s)^3\mathrm{S}_1$ (see also Fig. 1.4) is considered where the $^3\mathrm{P}_0-{}^3\mathrm{D}_1$ transition contributes by far the most due to its resonance around a frequency (wavelength) around 115 THz (2.6 µm). Integrating the transmitted BBR spectral density over the relevant frequency range (0-200 THz) the BBR frequency shift is calculated to $0.9(9)\cdot 10^{-19}$ and added to the Sr3 uncertainty budget (Tab. 3.4) at cryogenic operation.

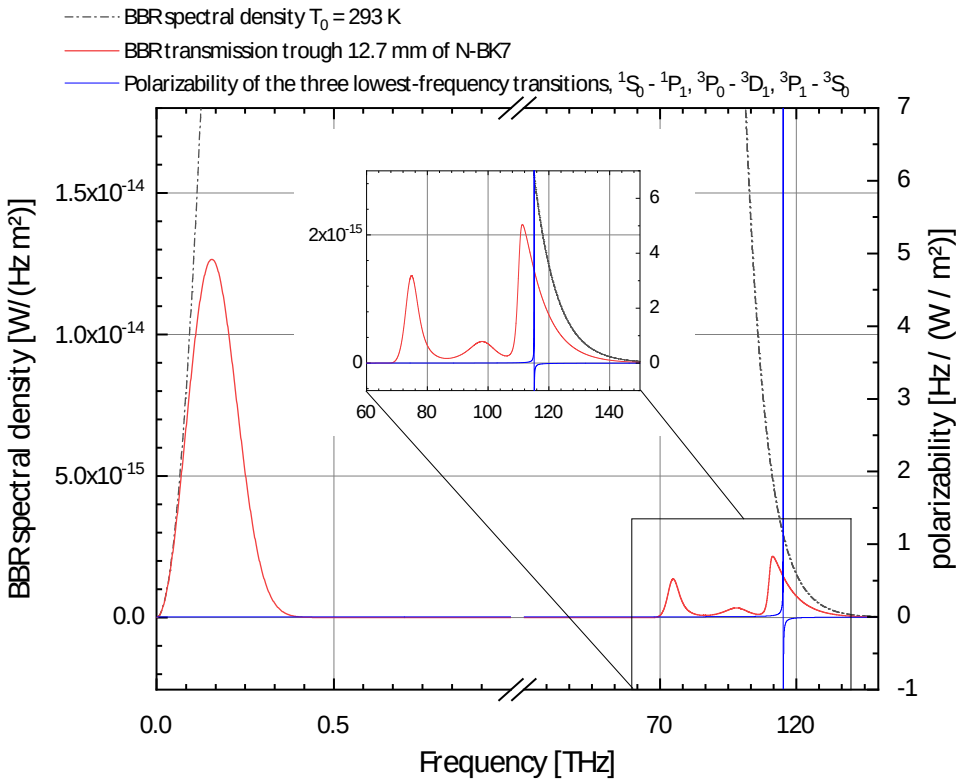

Figure 3.10.: Spectral density of black body radiation at a temperature of 293 K (gray semicolon line) including the residual transmission through 12.7 mm of N-BK7 (red solid line) as a function of radiation frequency. The BBR suppression due to absorption occurs over a wide frequency range of the BBR spectrum at room temperature. The transmission window at frequencies above 110 THz leads to poor suppression of the high frequency tail. The leakage of BBR around the $^3P_0 - {}^3D_1$ resonance causes the dominant shift contribution of a total shift of $0.9(9) \cdot 10^{-19}$ from the leakage through the N-BK7 windows.

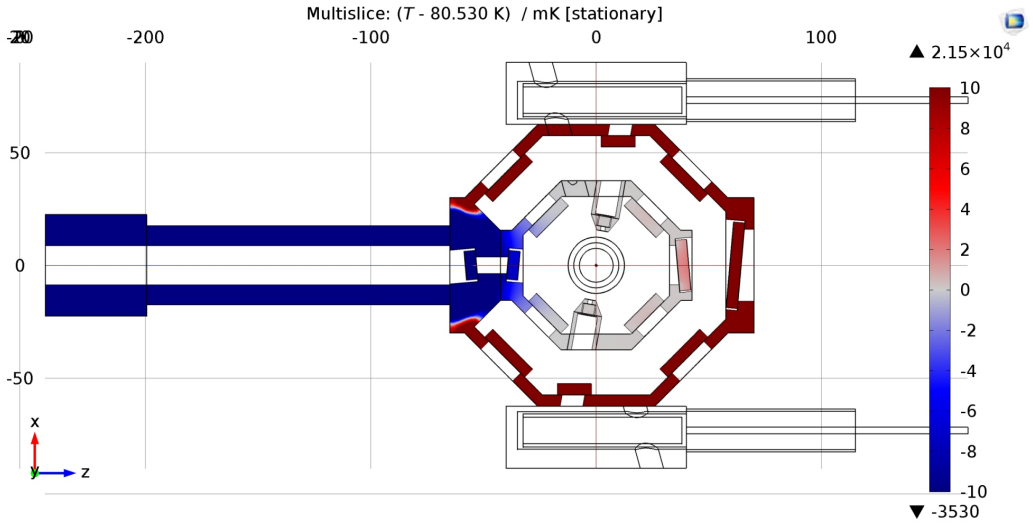

Figure 3.11.: Simulation of the temperature homogeneity of the cryostat when operated at cryogenic temperature. The mean temperature in the inner shield is about 80.53 K in the simulation. The peak temperature deviations are −3.53 K and +21.5 K over the shown parts of the cryostat. The temperature homogeneity of the inner chamber is considerably better, predicting a homogeneity of approx. 20 mK which translates to a frequency shift uncertainty of below $1 \cdot 10^{-20}$.

3.2.2. Expected frequency shift uncertainty from BBR

Placed in the middle of the inner shield, the atoms are excellently shielded from room temperature BBR. The 35 mm diameter pylon of the cryostat connects the outer shield and the cold finger of the pulse tube cooler. To allow access for the lattice- and clock laser the pylon is hollow featuring a 20 mm diameter hole. Results from a thermal simulation performed with the program "Comsol Multiphysics", indicate that the temperature of the cryostat ranges from the temperature of the cold finger of about 77 K to a maximum of approx. 102 K (Fig. 3.11) at the far end of the outer shield of the cryostat.

The temperature that the atoms experiences is the relevant parameter for the determination of the BBR shift which is that of the inner shield. Its temperature homogeneity is approx. 20 mK at 77 K in the simulation. According to Eq. 2.25 this leads to a 1-σ temperature uncertainty of 5.8 mK and a frequency shift uncertainty of below 10^{-20} in fractional frequency units.

3.2.3. Temperature acquisition

To measure the temperature of the cryostat during clock operation, eleven platinum resistance thermometers with a nominal resistance of 100 Ω at 0 °C (Pt100) are assembled to it. Ten of the sensors are supplied and calibrated by Sensing Devices Inc. (A2485) and the remaining one is from a different source (RS-Components, Order No. 293-8480). More details about their calibration can be found in Sec. 3.2.4. Five of the sensors are attached to the inner shield from where the temperature is directly processed to determine the clocks BBR shift. The outer shield holds four sensors and the pylon that is the connection to the cryocooler is equipped with two sensors. All sensors come with four wires that support the four-terminal sensing method (4T sensing). This technique increases the measurement accuracy by eliminating the lead and contact resistance from the measurement. All sensors are glued to the copper cryostat using the UV curable adhesive Optocast 3410 Gen.2. The glue was cured with an UV lamp at an optical intensity of approx. 40 mW/cm^2 for about 20 minutes. No additional high temperature bake out process was done to prevent the unprotected copper surface of the cryostat from oxidization.

The sensors are electrically connected to the CF-63 flange at the vacuum chamber that supports a Sub-D feedtrough. The pin assignment and sensor positions can be found in the appendix (Fig. A.3 and Fig. A.1). From the Sub-D connector the sensors are connected to a multiplexer (Fluke 1586-2588 DAQ-STAQ) and read out sequentially by a precision temperature scanner (Fluke 1586A Super-DAQ) where for each sensor the [a5] and [b5] coefficients and the resistance at the triple point of water (R(TPW)) (Sec. 3.2.3) is programmed to convert the sensors resistance into temperature according to the ITS90 temperature scale [83].

The readout interval of the temperature measurement bridge is typically once per minute. The measured temperature values are linearly interpolated to the 1 s grid used by the frequency counters. Automated real time BBR frequency shift corrections[8] are generated from these data during clock comparisons e.g. with the transportable clock Sr2 or the Yb^+ single on clock. Sr1 relied on a manual BBR shift evaluation. Especially temperature drifts of the system made the data evaluation tedious because long data

[8]This includes the correction to the thermodynamic temperature scale and corrections due to the unblocked apertures of the cryostat.

sets required separation in order to keep the systematic BBR correction and uncertainty reasonably low.

3.2.4. Calibration of Pt100 Temperature sensors

The ten Pt100 temperature sensors purchased from Sensing Devices Inc. have been calibrated by the supplier based on the "Guidelines for Realizing the International Temperature Scale of 1990 (ITS-90)[9]" with trace ability to the National Institute for Standards and Technology (NIST).

The manufacturer states an uncertainty (k=2) of 20 mK, 5 mK and 10 mK at temperatures of −196 °C, 0 °C and 30 °C respectively. Provided with each sensor are three individual coefficients: The electrical resistance at the triple point of water (R(TPW)), and the a[5] and b[5] coefficients that are experimentally found at the fix points defined in [83].

To verify that the calibration is still valid after shipment and storing the sensors for approx. 2 years, they were measured against a Pt25 platinum reference thermometer at our site.

Calibration at 0 °C to 50 °C:

For the calibration measurement, a home build test environment was used that is temperature controlled and well shielding the sensors under test from outside room temperature fluctuations. It consisted of a massive copper block (referred to as the test chamber) where the sensors are put into deep holes. Due to its size, the copper block is thermally very stable and rather insensitive to temperature fluctuations. Additionally, it is embedded into two layers of Styrofoam filled with buffer material for optimum shielding against the outside room temperature. The test chamber's temperature is controlled by a bath thermostat that provides a stable temperature within the range of approx. 0 °C to 50 °C. Four sensors can be tested simultaneously in the chamber where one was always the Fluke 5699 Pt25 reference thermometer. The measurement bridge that measures the sensors electrical resistance was a Fluke 1594A Super-Thermometer is referenced to an external resistance normal (Fluke 742A-100) with a nominal resistance of 100 Ω at a

[9] https://nvlpubs.nist.gov/nistpubs/Legacy/TN/nbstechnicalnote1265.pdf, Link last checked Sept. 2021

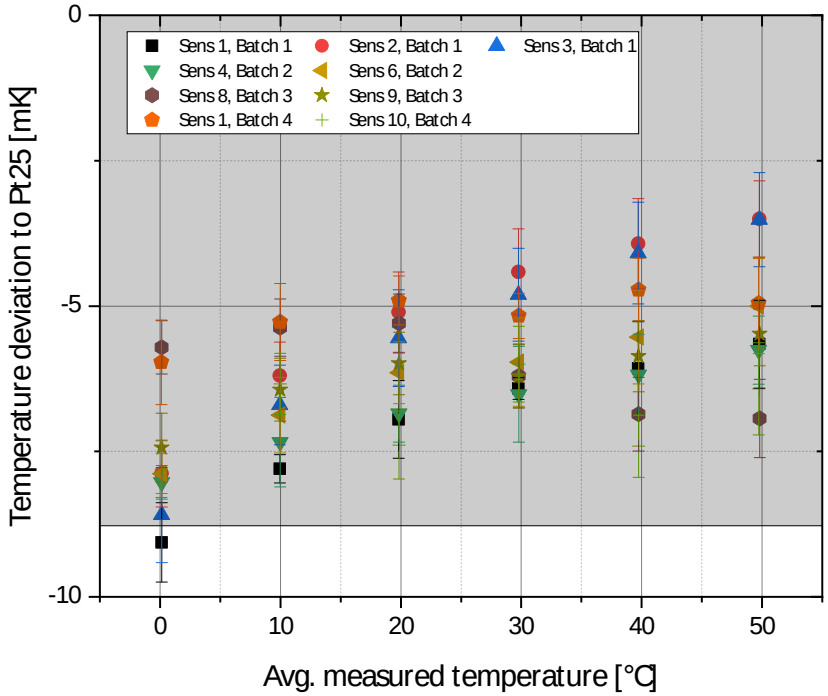

Figure 3.12.: Experimental results from the calibration of the Pt100 temperature sensors. Shown is the deviation of the temperature calculated with the [a5] and [b5] coefficients from the measured resistance according to ITS90 [83] with respect to the Pt25 reference platinum thermometer. The gray shaded area is the estimated systematic uncertainty of the calibration environment and the sensors (details in the text) which spans symmetrically around zero. Error bars are statistical uncertainties by the standard deviation. The results are corrected for self heating of the sensors in the environment (details in text).

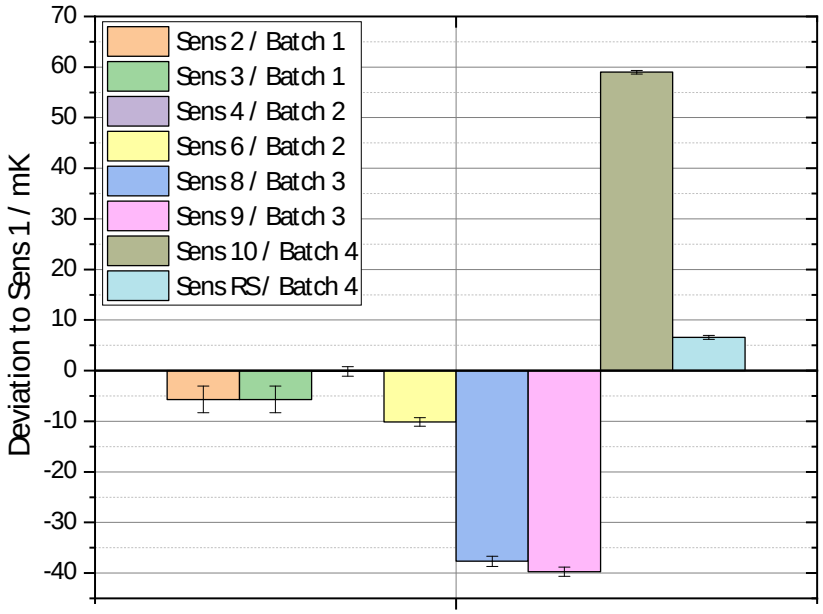

Figure 3.13.: Experimental results from the calibration of the Pt100 temperature sensors performed in liquid nitrogen at approx. 77 K. Shown here is the deviation of the calculated temperature from the measured resistance according to ITS90 [83] with respect to the sensor 1. Error bars are the statistical uncertainties represented by the standard deviation of the measurement.

temperature of 20 °C. All sensors have been measured using the four terminal sensing method. In each measurement batch, three Pt100 sensors are measured against the Pt25 reference thermometer at temperatures of $0, 10, 20, 30, 40$ and 50 °C. Each temperature was held for at least six hours after a 30 minute ramping from the previous temperature at a data recording interval of 30 s. The order of the aforementioned test temperatures were chosen random to avoid unnoticed systematic changes of the calibration unit.

All tested Pt100 sensors are in agreement with the Pt25 within the measurement uncertainty as seen in Fig. 3.12. For all sensors the manufacturer calibration uncertainty is confirmed at 0 °C and 30 °C within the uncertainties of the measurement. Unfortunately during handling two sensors (No.5 and No.7) got damaged and clearly show false readings different to the others by several tens of mK. These sensors are installed at the cryostat anyway and serve as auxiliary sensors only and are not considered for the evaluation of the BBR frequency shift. The total systematic uncertainty of the measurement is estimated to 8.8 mK[10]. It is depicted as the gray shaded area in Fig. 3.12. Since sensor 1 has been measured in two different batches (batch 1: black squares, and batch 4: orange pentagons) it allows for an estimation of the systematic reproduceability of the temperature measurements. The deviation of the measurement results of this sensor is approx. 3 mK and included in the total systematic uncertainty of the measurement environment.

The electrical sensing current applied to the sensors during the calibration measurement is typically regulated to constant 1 mA. This leads to parasitic heating of the sensors which affects the temperature measurement in the form of an offset. To correct for it, the measurement was repeated with two times the electrical power. The measured temperature deviation is then extrapolated to a sensing current of I=0 mA for all sensors. The results in Fig. 3.12 this correction is applied.

Calibration at liquid Nitrogen temperature: To verify the calibration of the sensors at liquid nitrogen temperature (LN_2) of approx. 77 K, a Dewar was used since the test environment used for the previous calibration is not capable for testing at such temperature. The Dewar was filled with LN_2 and three Pt100 sensors immersed into it. The Pt25 was separately immersed, but unfortunately it prove to be not suitable for an

[10] Uncertainty contributions are: 4 mK measurement uncertainty of the setup, 4 mK heat conduction through wires, temperature gradients and heat resistance, 6 mK calibration uncertainty of the sensors, 3 mK uncertainty of the Pt25 reference thermometer.

accurate comparison. Due to its very long probe compared to the Pt100 sensors its temperature reading differed to those of Pt100 sensors was several K and strongly dependent on the depth of the immersion into the bath. Therefore one of the Pt100 sensors 1 was chosen as reference sensor and the temperature deviation of the other sensors measured against it. This procedure automatically removes temperature drift of the bath since they are common mode rejected. Of course the calibration of the supplier cannot be verified by this procedure but still allows to identify sensors that produce unreliable results at 77 K. In Fig. 3.13 the remaining sensors agree within a range of 100 mK. This is far away from the 20 mK of calibration uncertainty claimed by the supplier. But the setup used to test the sensors was rather provisional. Potential errors such as parasitic heat intake trough the wires of each sensor are likely to have happened during the measurement. Such calibration measurements at liquid nitrogen temperatures are typically performed with the sensors mounted into a massive copper block to ensure temperature homogeneity and careful immersing it into the bath. The bath itself should under optimal conditions be non boiling which takes about two days in a well isolated Dewar. In our case the sensors were put into a little mount consisting of two copper plates to simply hold the sensors in place. The LN_2 was able to flow around the sensors potentially causing temperature gradients along the sensor. The temperature measurement was started a few hours after the LN_2 was filled into the Dewar, having the LN_2 still boiling. Additionally a commercially available Pt100 sensor from RS-Components (Order No. 293-8480, accuracy class 1/10 B) was tested using standard coefficients according to DIN IEC 751 for the resistance/temperature conversion. As seen in Fig 3.13 the temperature deviation of this "general purpose" sensor is surprisingly small compared to some of the other sensors which is why it was assemble onto the cryostats pylon. A complete overview of the position of each sensor at the cryostat can be found in the appendix (A.3).

3.2.5. Cooling the cryostat

With the vacuum system set up and the cryostat installed, a first test was performed to cool it to cryogenic temperature. The electric power of the pulse tube cooler was increased step wise to prevent high cooling rates that may induce thermal stress especially on the indium/window connection. A falling off window would be a total failure. After approx. one day of cooling, cryogenic temperatures of about −190 °C have been reached (Fig. 3.14). After another day the temperature of the cryostat is stable to the mK level with negligible remaining settling rate of below 100 mK/d. The temperature instability after reaching stable conditions (starting after approx. 2 days in Fig. 3.14) is at the low mK level or even below 1 mK, as seen in Fig. 3.15. This is below the calibration uncertainty of the individual sensors.

In Fig. 3.14 the sensor I3 shows significantly higher temperature readings of several Kelvin compared to the other sensors at the inner shield I1, I2, I4, and I5. This behavior is also observed at room temperature so that parasitic heating of this sensor from the environment can be ruled out. It is considered broken and unreliable. Its readings will not be considered for BBR shift evaluation. The readings of I1, I2, I4 and I5 are in good agreement where I4 is showing a slightly higher reading. I4 is mounted on the lid of the inner shield and shows an approx. 400 mK higher reading compared to I1, I2 and I5. Those sensors are in agreement of approx. 20 mK verifying the expected temperature homogeneity of the simulation (Fig. 3.11). The higher reading of I4 is likely caused by a non ideal thermal contact between the lid and the main body of the inner shield which was not included of the thermal simulation. For the evaluation of the BBR shift its readings will be considered. The measured temperature homogeneity of the inner layer of the cryostat, facilitates in a BBR shift uncertainty of about $2 \cdot 10^{-19}$ in fractional frequency units.

As expected the outer shield is slightly colder than the inner one due to its direct connection to the cold finger of the pulse tube cooler (Fig. 3.9) via the pylon. The pylon therefore has the lowest temperature of the entire cryostat. The electrical output power of the pulse tube cooler was approx. 80 W to maintain a mean temperature of about −190 °C of the cryostat. This is only about 50% of its maximum allowed power input. At such electric drive power, its cooling power is about 5 W according to the devices data sheet.

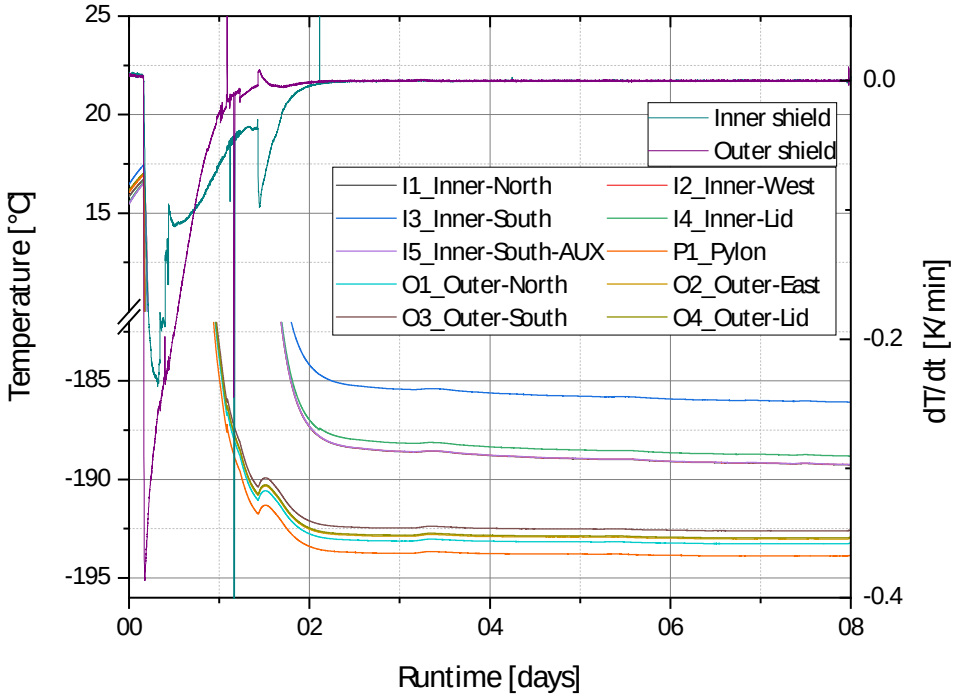

Figure 3.14.: Course of one temperature during the first cooldown experiments of the cryostat. The temperature readings shown are from all in vacuum sensors. The sensor I3 shows a significant offset to the other sensors of the inner shield for unknown reason and is considered damaged during assembly. The other sensors of the inner- and outer shield are in good agreement among each other. The secondary axis shows the temperature variation of the mean inner- and outer shield temperature. After approx. one day of cooling a mean temperature about $-190\,^{\circ}\mathrm{C}$ was reached whereas temperature stability at the mK level requires another day to settle. For a period of several days the cryostat was operated at stable cryogenic temperature conditions.

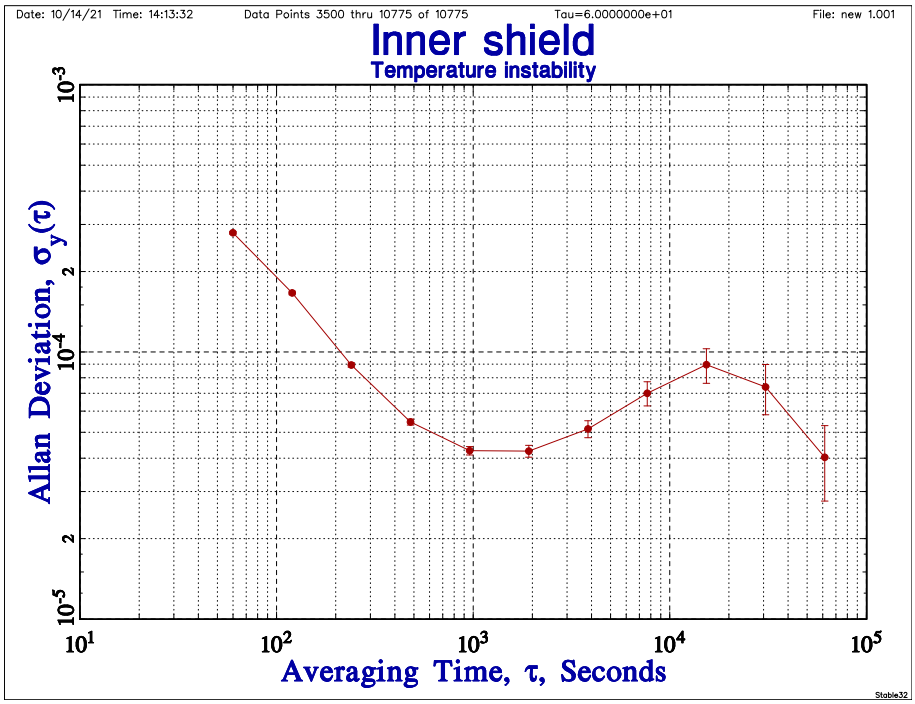

Figure 3.15.: Allan Deviation of the temperature variation of the inner shield after reaching stable conditions seen in Fig. 3.14. The temperature instability reaches a level of below 10^{-4} which is below the calibration uncertainty of the sensors.

3.2.6. The missing cryogenic atomic beam shutters

The demonstrated temperature homogeneity of the inner shield of the cryostat leads to a BBR shift uncertainty at a level of about $2 \cdot 10^{-19}$. However this exclusively refers to the cryostat and neglects the influence of the cryogenic atomic beam shutters (and the leakage through the installed N-BK7 windows) that are yet not installed. Their purpose is to allow loading from the atomic beam into the MOT and prevent any BBR, either from the hot atomic oven or outside room temperature to enter the inner shield during spectroscopy and causing a frequency shift. At the present stage of the Sr3 clock, during spectroscopy there is a direct line of sight between the atoms and room temperature BBR through the unblocked apertures. The geometry on both sides of the cryostat is named "atom injection tube" (AIT). Therefore the absent shutters must be included as an additional source of uncertainty into the clocks uncertainty budget. In the following an estimation of their uncertainty contribution to the total BBR shift is given.

The amount of room temperature BBR the atoms experienced can be described by the solid angle the apertures allow for a direct line of sight between the atoms and the room temperature environment of the laboratory. The center of the two 10 mm diameter apertures are located $72.5\,\mathrm{mm}/\cos^2(15°) = 77.7\,\mathrm{mm}$ away from the atoms. For the determination of the solid angle the apertures are assumed circular for simplicity neglecting their ellipticity. The solid angle Ω for one aperture with respect to the 4π full sphere is calculated to

$$\Omega = \frac{1}{2}\left(1 - \cos\left(\arctan\left(\frac{5\,\mathrm{mm}}{77.705\,\mathrm{mm}}\right)\right)\right) = 1.023(51)\cdot 10^{-3} \;/\; 4\pi \tag{3.1}$$

The uncertainty is related to 5% due to manufacturing tolerances. Additionally intruding BBR may reach the atoms by residual reflection from the surface of the inner chamber although three layers of Aquadaq strongly suppress this. To account for imperfection of the Aquadaq layer, a minimum absorption coefficient of $\alpha_{min} = 0.8$ is assumed conservatively. Following the description in [84] this can be interpreted as an enhancement of the apertures solid angle by a factor of

$$\frac{\Omega_{\mathrm{eff,max}}}{\Omega} = \frac{1}{(1 - \Omega/4\pi)\;\alpha_{\mathrm{min}} + \Omega/4\pi} = 1.25 \tag{3.2}$$

Here we continue with the mean solid angle

$$\Omega_{\text{eff,mean}}/\Omega = (1 + \Omega_{\text{eff,max}}/\Omega)/2 = 1.124(72) \tag{3.3}$$

with an attributed uncertainty of $u(\Omega_{\text{eff,mean}}/\Omega) = (\Omega_{\text{eff,max}}/\Omega - 1)/\sqrt{12}$ according to [85].

The total frequency shift $\Delta\nu_{\text{AIT}}$ due to the two missing shutters can be described by the difference between the external frequency shift $\Delta\nu_{BBR,ext}$, that takes the solid angle into account, and an internal BBR shift $\Delta\nu_{BBR,int}$ of the cryostat

$$\Delta\nu_{\text{AIT}} = 2\ \left(\Delta\nu_{\text{BBR,ext}} - \Delta\nu_{\text{BBR,int}}\right)\ \Omega_{\text{eff,mean}}/4\pi \tag{3.4}$$

with $\Delta\nu_{\text{BBR,ext}}$ being the BBR induced frequency shift of the intruding BBR which is in principle that of the laboratory of a temperature of 293(2)K.

At the experimental conditions during the first cool down described in Sec. 3.2.5, one finds a frequency shift contribution of $\Delta\nu_{\text{AIT}} = -11.02(95) \cdot 10^{-18}$ that is added to the clocks uncertainty budget in Tab. 3.4. The uncertainty was determined with Gaussian error propagation (GEP) of Eq. 3.4. At cryogenic operation, the uncertainty contribution of the missing beam shutters is dominating the total BBR shift uncertainty as seen in Tab. 3.4. The laboratory temperature is stabilized by an active air conditioning to approx. 20 °C with fluctuations observed that typically do not exceed ±0.5 K. Also it is rather unlikely that parts of the steel chamber get significantly warmer than the environment. All potential sources for heat intake into the steel chamber (Zeeman slower, MOT coils and PT-cooler) are actively water cooled or do not have a direct line of sight to the atoms. In that sense attributing an uncertainty of 2 K to the temperature of the external BBR contribution is rather conservative. In the method described above, both apertures are being treated equally regarding the BBR field that is assumed to enter the cryostat. Although one aperture is pointing to the hot atomic oven. This is addressed by a separate steerable shutter close to the oven. It blocks the line of sight between the oven and the atoms during spectroscopy. This will be described in the next section.

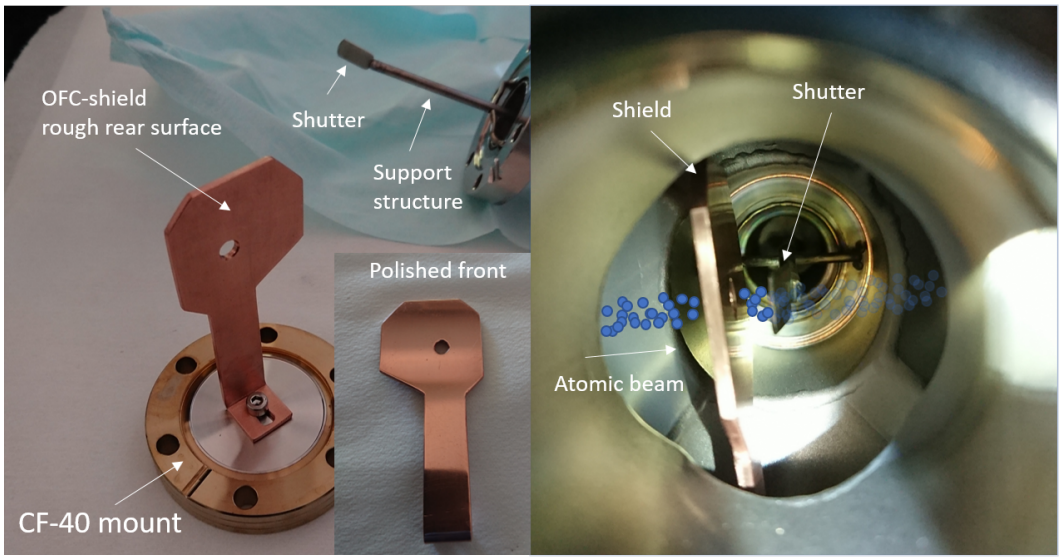

Figure 3.16.: Picture of the OFHC-shield that protects the shutter from radiative heating by the hot atomic oven. The shutter can be moved sideways

3.2.7. Oven shutter

A direct line of sight from the hot atomic oven to the atoms undergoing spectroscopy, can lead to a BBR frequency shift. Therefore a shutter is installed close to the oven to block the line of sight from the oven to the atoms during spectroscopy to suppresses a BBR shift contribution from the hot atomic source. The shutters is steered by a brushless servo motor (Savöx SB-2272MG) which is controlled by a microprocessor that enables to steer the shutters state by a TTL signal from the experiment control program. It is mounted in one of the CF-40 ports at the vacuum cross between oven and Zeeman slower. The distance from the oven is approx. 7 cm. The shutter blade which is the part of the shutter that effectively blocks the line of sight, is made from stainless steel (SST) and approx. 8 mm × 16 mm in dimension. To prevent the shutter from being heated by the emitted radiation from oven, a heat shield with a center aperture of 5 mm is installed approx. 1 cm before the shutter (Fig. 3.16). It is fabricated from 2 mm thick OFHC copper and has a highly polished surface facing the oven to reflect most of its radiation. The backside is fabricated rough to prevent BBR reflecting to the atoms. Due to the copper heat shield, the shutter has a line of sight to the oven only when closed and is completely hidden behind it in the open state. In this way the radiative heat intake from the oven is minimized. Assuming a worst case emissivity of the oven of $\epsilon_{oven} = 1$ and a temperature

of $T_{oven} = 800\,\mathrm{K}$, according to the Stefan-Boltzmann law the maximum radiation power of the oven is about 20 W. For an upper limit estimate, here we assume all the radiative power to be directed exclusively towards the heat shield. The emissivity of the polished copper shield is very high and estimated to $\epsilon_{shield} = 0.05$, thus it cannot absorb more than 1 W in this worst case scenario. In reality the oven can be expected to radiate in all spatial directions which will reduce the thermal load on the heat shield. The thermal resistance to the CF-40 mounting surface of the heat shield is estimated to be 1 W/K which is rather poor but serves once again as an upper limit since no grease or foil was used to improve the thermal conductivity. The shields maximum temperature deviation ΔT to ambient temperature is calculated by Fourier's Law of Heat Conduction

$$\dot{Q} = \lambda_{\mathrm{OFHC}} \frac{A}{l} \Delta T \tag{3.5}$$

where $\dot{Q}$ is the heating power, $\lambda_{\mathrm{OFHC}} \geq 350\,\mathrm{W/mK}$ the heat conductivity of OFHC copper and $A = 3 \cdot 10^{-5}\mathrm{m}^2, l = 0.1\,\mathrm{m}$ the geometric cross section and length of the heat shields post. According to Eq. 3.5 and taking into account the thermal resistance of the mounting surface one finds a maximum temperature difference of $\Delta T \leq 10\,\mathrm{K}$. This corresponds to a maximum emission of the heat shield of $\approx 50\,\mathrm{mW}$ only. This is the maximum power the shutter can be heated with which can be neglected.

When the shutter is in the closed state, the heating power from the stainless steel ($\epsilon_{\mathrm{SST}} = 0.6$) oven is at maximum $\dot{Q}_{\mathrm{nozzle}} = 1.5\,\mathrm{W}$.

To estimate the BBR shift from the shutter it is required to know its temperature. Continuing on assumptions about the shutters steady state temperature as before, is not feasible since the heat transport into the shutters support structure and into the CF-40 flange is hard to estimate since the thermal resistance of the interconnection is hard to estimate.

Therefore the temperature of the shutter was measured with a thermal camera (Testo 875-1i). A viewport at the CF-40 six-way-cross allows to observe the shutter blade. It holds a window made from zinc selenide (ZnSn) that is transparent for infrared radiation. After a few days of clock operation, all the relevant vacuum components are considered thermally stable. The shutter was kept closed for several hours to maximize heating from the 500 °C hot oven. In clock operation the shutter is in either state for approx. half of the cycle duration, which reduces also the heat intake by 50%. The stainless steel six-way-

cross directed to the oven had a temperature of 84 °C. In contrast the temperature of the closed shutter was measured to $T_{\text{shutter}} = 28\,°\text{C}$ only which was below of our expectations and is considered neglectable. In addition the 2 mm aperture of the copper gasket between the gate valve and the Zeeman slower tube (Fig. 3.1), allows only a tiny solid angle of $\Omega_{\text{pinhole}} = 8.55 \cdot 10^{-7} \;/\; 4\pi$ seen from the atoms. Given by the tiny solid angle the shutter blades BBR shift and uncertainty contribution is below the 10^{-20} level even for an unrealistic temperature of the blade of 100 °C. Therefore the BBR shift contribution of the atomic beam shutter can be neglected.

Additionally an interleaved measurement, alternating between open and closed shutter was performed to study the BBR frequency shift the hot oven induces. The measurement revealed a zero compatible frequency of $8(117) \cdot 10^{-20}$. This implies that the shutter is not crucial for operation.

3.3. Stability transfer from a cryogenic Si resonator

Ultra stable laser systems are essential tools for narrow line spectroscopy. As mentioned before the Sr3 interrogation laser system is pre-stabilized to a 48 cm-long ULE cavity [63] that provides a frequency instability of about $4.7 \cdot 10^{-16}\ \tau^{-1/2}$ [70] for an interleaved clock measurement with τ the measurement time in seconds. The total Allan deviation of such a measurement can seen in Fig. 3.17. The clock instability can be reduced further by pre-stabilizing the interrogating laser system to a cryogenic silicone resonator. This improves the clocks instability to approx. $1.5 \cdot 10^{-16}\ \tau^{-1/2}$. To reach a statistical uncertainty of $1 \cdot 10^{-18}$, a clock measurement time of about 61 h is required when using the ULE cavity. In contrast the measurement time reduces by about a factor of 10, when stabilizing the clock laser to the cryogenic silicon cavity, to about 6 h. This enables high precision measurements at the low 10^{-18} level on a daily bases. The ULE cavity is specially designed to operate at the clock laser wavelength of 698 nm. In contrast the cryogenic silicone cavity is operated at a wavelength of 1542 nm due to the transmission properties of the silicone mirror substrates. To transfer the frequency instabilities of the silicone laser to the 698 nm laser, the large frequency gap between the two systems is bridged using an optical frequency comb as a transfer oscillator [19, 86]. The noise contribution of the optical frequency comb is below the thermal noise floor of any of the cavity stabilized lasers and is therefore negligible. Additional noise arising from disturbances acting on the optical fibers connecting the lasers and the frequency comb, is suppressed by an active path-length stabilization [64].

For some of the measurements even two crystalline silicone cavities were available. By stabilizing the clock laser to the average frequency of the two silicone cavities, the clock instability improved to about $\sigma_y = 1.2 \cdot 10^{-16}/\sqrt{\tau}$ for interleaved measurements. To infer a single-cycle instability from this an instability contribution from the Dick effect of $4.7{\cdot}10^{-17}/\sqrt{\tau}$ is added in quadrature [70]. This leads to a n instability of $\sigma_y^{sc} = 5{\cdot}10^{-17}/\sqrt{\tau}$ which is at the same level as the best instability of an optical clock reported so far [87].

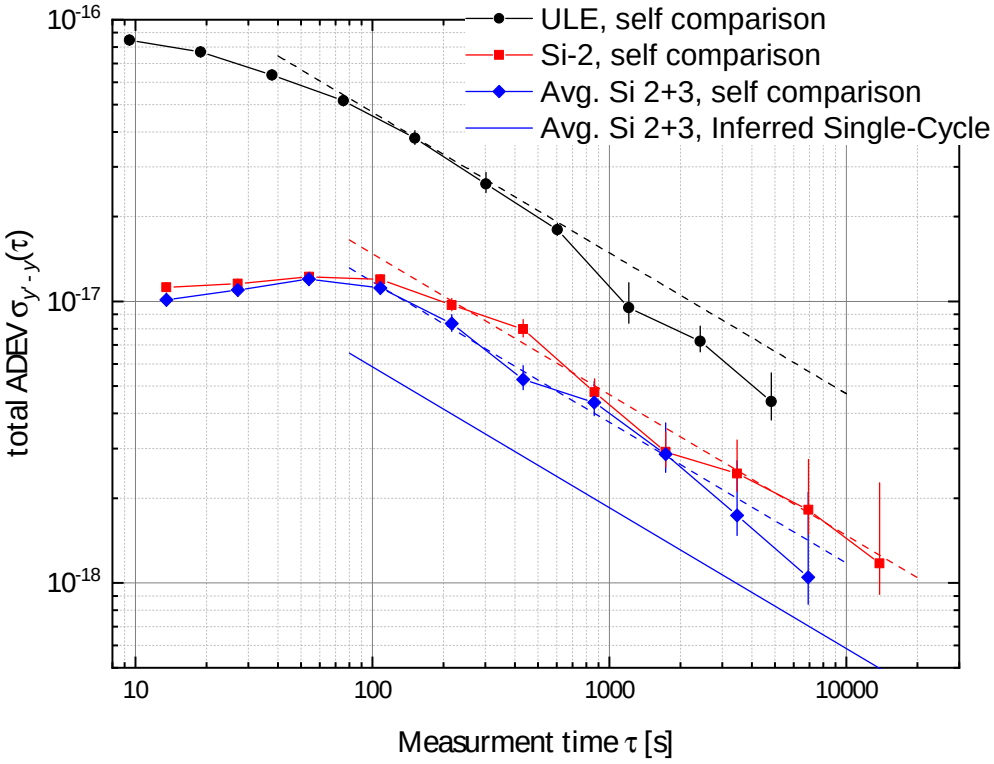

Figure 3.17.: Frequency instability of Sr1 with the interrogation laser system pre-stabilized to different cavities. As reported in [70] the ULE cavity provides an instability of approx. $4.7 \cdot 10^{-16}\ \tau^{-1/2}$ (black dashed line) in a self comparison measurements. In contrast the observed frequency instability using one cryogenic silicone cavity (red dashed line) reduces to approx. $1.5 \cdot 10^{-16}\ \tau^{-1/2}$ which reduces the measurement time by about a factor of 10 to reach the same statistical uncertainty. When using the averaged signal of two cryogenic silicone cavities an ultimate instability of $5 \cdot 10^{-17}\ \tau^{-1/2}$ is inferred for a single cycle stabilization measurement.

3.4. Electrodes and dc Stark shift measurements

Static electric fields are also subject of systematic frequency shifts in lattice clocks [62, 88, 89]. Unlike the ac Stark shift that arises due to the light field of the optical lattice, the dc Stark shift is caused by static electric fields. Such fields can arise from potential differences of the surrounding surfaces or buildup of charges on insulating materials. The dc Stark shift is proportional to the square of the electric field.

The atoms are trapped and interrogated inside the cryostat made of highly electrically conducting copper described in chapter 3.2.1. The cryostat is electrically grounded sharing the same potential as the vacuum chamber and any electric device connected to it. In this way potential differences among surrounding surfaces are minimized. The vacuum chamber itself is grounded to the laboratory power grid. To prevent ground loops the vacuum chamber and the power supplies of connected devices such as ion pump controllers, vacuum gauge meters and the temperature measurement bridge share the same multi-pole socket and thus the same ground potential. The conducting steel vacuum chamber represents a Faraday cage, effectively shielding the atoms from outer electric fields. The optical windows in the cryostat however are coated with dielectric material to minimize optical transmission losses for the required laser beams. The coated areas are not in electrical contact with the cryostat and may allow charge build up. In that consequence a dc Stark shift can arise that needs to be characterized.

In the presence of an electric field the dc Stark frequency shift can be described by Eq. 2.17 with the frequency dependent contribution to

$$\Delta\nu_{DC} = -\frac{1}{2h}\Delta\alpha_{DC}\vec{E}_0^2 \tag{3.6}$$

Here $\vec{E}_0$ is the residual electric field. With an additional user-applied field $\vec{E}$ one can write a frequency shift in the form

$$\Delta\nu = \Upsilon(\vec{E} - \vec{E}_0)^2 \tag{3.7}$$

Such an additional field is generated by applying a voltage U to one of the electrode pairs. The electric field is connected to the applied voltage by the known relation $E \propto U$. The parameter Υ includes relevant atomic properties such as the polarizability. Precise

knowledge about it is not required which becomes clearer in the following development of the formalism that mainly relies on measurable frequency shifts. It is to be mentioned that higher order shift contributions are neglected in this evaluation.

The residual field can be decomposed into parallel and perpendicular contribution to the field direction addresses by the electrode pair

$$E_0^2 = E_{0,\parallel}^2 + E_{0,\perp}^2 \tag{3.8}$$

resulting in a voltage dependent differential frequency shift of

$$\Delta\nu(U) = \Upsilon\left[(E(U) - E_{0,\parallel})^2 + E_{0,\perp}^2\right] = \Upsilon\left[(E^2(U) - 2EE_{0,\parallel}) + E_0^2\right] \tag{3.9}$$

In a clock interleaved measurement, opposite but equal voltages are applied to the electrodes of one pair in one cycle and the electrodes set to a common-ground potential otherwise leads to

$$\Delta\nu(U) - \Delta\nu(U=0) = \Upsilon\left[E(U)^2 - 2E(U)E_{0,\parallel} + E_0^2 - E(0)^2 + E(0)E_{0,\parallel} - E_0^2\right] \tag{3.10}$$

Assuming that the field $E(0) \equiv 0$ Eq. 3.10 becomes

$$\Delta\nu(U) - \Delta\nu(U=0) = \Upsilon E(U)\left(E(U) - 2E_{0,\parallel}\right) \tag{3.11}$$

Defining

$$\sqrt{\Upsilon}E(U) \equiv U\sqrt{-A} \tag{3.12}$$

$$\sqrt{\Upsilon}E_{0,\parallel} \equiv B\sqrt{-A} \tag{3.13}$$

Eq. 3.11 becomes

$$\Delta\nu(U) - \Delta\nu(U=0) = AU(U-2B) \tag{3.14}$$

which is the vertex shape of a parabola developing from the origin and is centered around $-B$. It is interpreted as an offset voltage denoted U_0 in units of V in the following. The parameter A describes the opening of the parabola. It is related to the geometric proprieties of the electrode and comes in units of V^{-2}.

The result of an interleaved measurement is a frequency difference $\Delta\nu$ between the two measurement cycles. Leaving A and B as free parameters in Eq. 3.14 for a parabola fitting function, they are obtained from at least three interleaved measurements. By definition the parabola must cross the origin, because an interleaved measurement with identical applied voltages in both cycles must lead to a zero frequency shift (zero measurement).

So far only a two dimensional problem is discussed. But in fact the unknown background field, named $\vec{E}_{bgr}$ in the following, is pointing arbitrarily in the three dimensional space. With the present description only the projection of it on the applied field of the respective electrode pair can be characterized. To find out its total magnitude a three dimensional analysis is required and thus at least three pairs of independent electrodes are required that are able to produce electric field in different directions. In the following the electrode array that allows to apply electric field in three dimensions will be described.

The ring electrode array

Two ring structures holding a symmetric arrangement of one electrode per quadrant were installed into the inner shield of the cryostat (Fig. 3.18 and Fig. A.2)). The rings are made of aluminum-Nitrate (ALN 180) with an outer/inner diameter of 45 mm / 25 mm and a thickness of 1 mm. The distance between opposite electrode pair is approx. 22 mm. Each ring holds four electrically separated quadrants that represent the electrode. They are made of a 20 µm layer of an electrically conducting, vacuum compatible alloy of Silver and Palladium (AgPd). Special wires suitable for cryogenic ultra high vacuum operation (Lakeshore WQL Phosphor bronze wire, Non-ferromagnetic, AWG 36) are soldered to the electrodes (soldering paste: Kester EM 907) and connect each electrode to the Sub-D feed trough of the chamber. A scetch of the assembly and the pin assignment can be found in the appendix in Fig. A.2 and Fig. A.3. Each electrode can be addressed individually. In the process of the evaluation this either by a selected voltage or being put to the vacuum systems common ground potential. The DC voltage was supplied by a Fluke

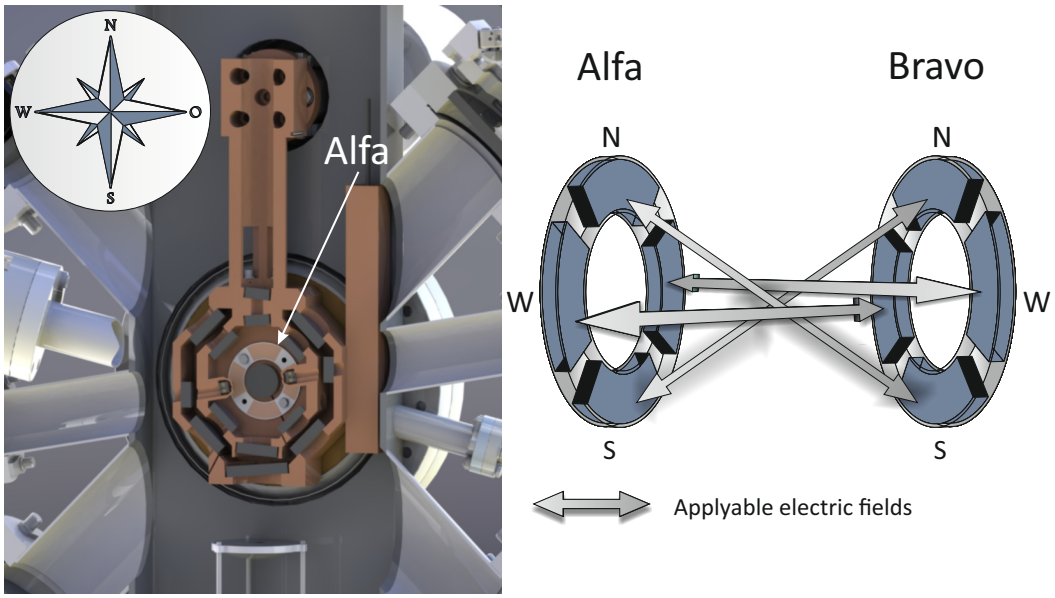

Figure 3.18.: CAD image (left) of the electrode denoted "Alfa" installed in the inner shield of the cryostat. The compass in the upper left indicates the naming of the individual quadrants. The right sketch explicitly states the naming of each electrode to avoid confusion. For the characterization of the residual dc Stark shift the applied electric fields are highlighted by gray arrows.

415B high voltage power supply that provides stable output voltage below the %-level. In the measurement series described in the following electric fields are applied in a way as shown in Fig. 3.18. The two ALN-rings are denoted "Alfa" and "Bravo" and their electrodes denoted by cardinal directions. The atomic oven is hereby in the direction of the eastern quadrant. In the following a "pair" of electrodes will always refer to an applied electric field between kitty-corner positions. The notation "Alfa-North" → "Bravo-South" ("ANBS") for example, indicates an applied voltage between the electrodes "Alfa-North" and "Bravo-South". In the following only the following short notations "ANBS" ("Alfa-North" → "Bravo-South"), "ASBN" ("Alfa-South" → "Bravo-North"), "AEBW" ("Alfa-East" → "Bravo-West") and "AWBE" ("Alfa-West" → "Bravo-East") are used. The arrangement of the electrodes allows determination of the residual electric field direction and magnitude at the position of the atoms. The geometrical characterization of the electric fields generated by the electrode arrangement and the atoms react to by a dc Stark frequency shift must be done experimentally. This will be describe further on in the text. It is not sufficient to simply use geometric properties (e.g. extracted from CAD-model or measured at the assembled cryostat) since the nozzle-like structure inside the inner shield

as well as soldering points break symmetry and may distort the applied electric field.

In the first series of measurements a DC voltage was applied to one of the electrode pairs in one of the two interleaved measurements cycles. The total applied DC voltage was typically 40 V (e.g. in an "ANBS"-measurement) separated to −20 V to one electrode and 20 V to the other electrode of the pair. In the follwing this will be denoted as ±20 V as this refers to the electric field the atoms experiments (apart from the background shift) during one cycle of the measurement. In the second clock measurement cycle these electrodes were put to ground potential like the other ones to ensure they cannot cause an additional frequency shift apart from the background field $\vec{E}_{bgr}$. The measured frequency shift between the two cycles is then attributed to the user-applied electric field and a contribution of $\vec{E}_{bgr}$ parallel to the addressed electrode pair (Fig. 3.19). This will also be called projection of $\vec{E}_{bgr}$.

Nevertheless the background field $\vec{E}_{bgr}$ is not likely to point parallel to any pair of electrodes by coincidence. it is more likely to point arbitrarily in the tree dimensional space. In an interleaved measurement as described above, it is only possible to determine the projection of $\vec{E}_{bgr}$ on the respective direction of the electrode pair (see Fig. 3.19). The angle between $\vec{E}_{bgr}$ and the field directions given by the electrode pairs is not known yet and cannot be determined by the interleaved measurements described above. Thus one has to extend the description of $\vec{E}_0$ by a constant user applied contribution and the contribution of the background field $\vec{E}_{bgr}$. This leads to an additional series of characterization measurements different from the one described above. To differentiate between the two different kinds of measurements those described above with an applied field in one of the two cycles of an interleaved measurement will be denoted "Series 1.)" in the following. Those measurements with an additional constant field in both cycles are denoted "Series 2.)". Fig. 3.19 illustrates the difference between the two measurement series.

In this series of measurements a constant field is applied in both cycles of the same interleaved measurements performed before. The additional electric field is generated by an applied DC voltage of ±20 V.

The constant field is applied to the opposites side of the interleaved field (blue and green arrows Fig. 3.19 right).

The differential frequency shift measured in a measurement of Series 2.) now originates from the user-applied field and the projection of $\vec{E}_{bgr}$ onto the applied field. The

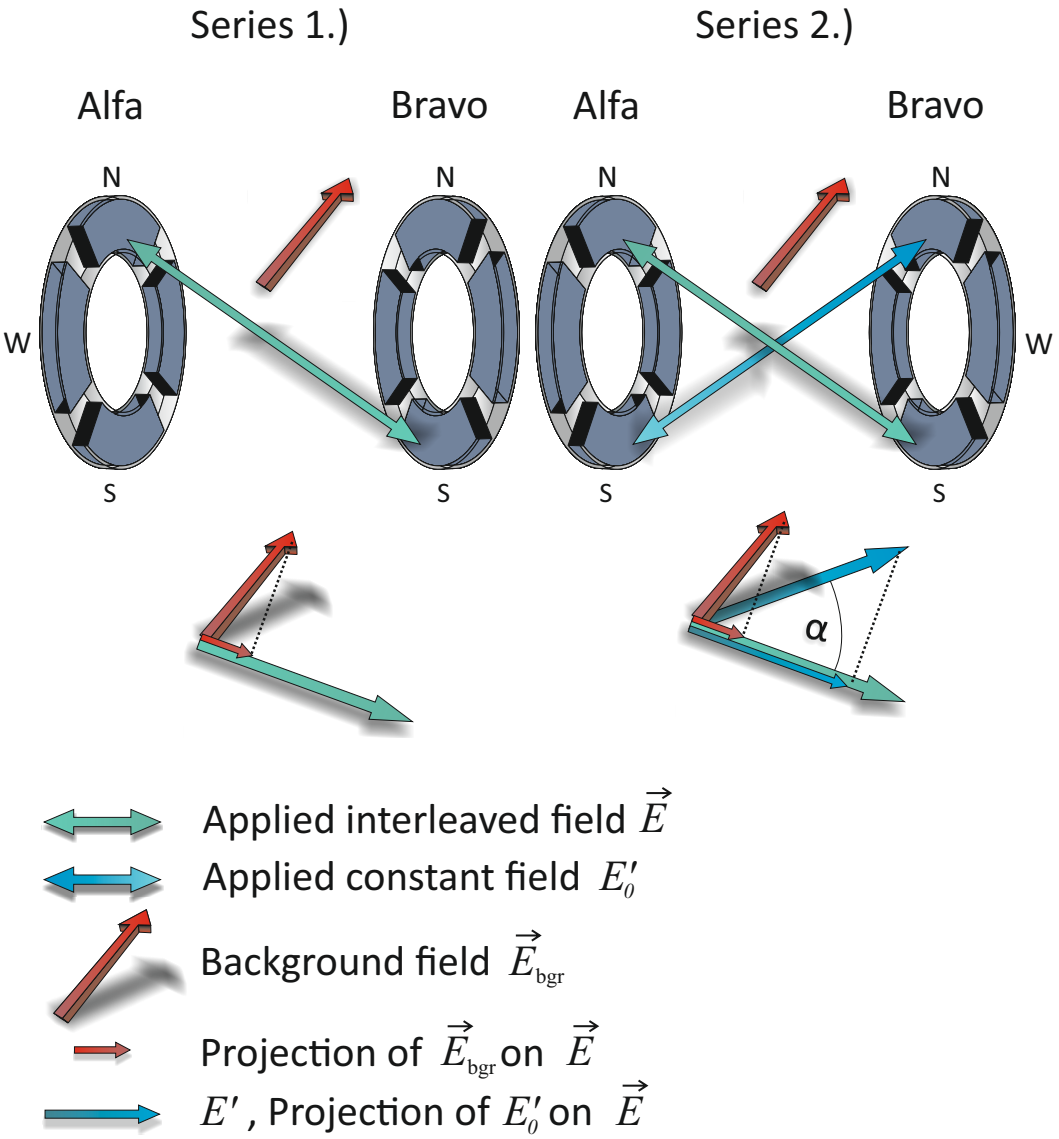

Figure 3.19.: Principle sketch of the applied electric fields during the two different measurement series. In Series 1.) the applied electric field in one cycle of the interleaved measurement includes the projection of the background field $\vec{E}_{bgr}$ that is the dc Stark shift in the clocks uncertainty budget. The magnitude and direction of $\vec{E}_{bgr}$ can only be determined by additional measurements with a constant electric field on opposite electrodes (Series 2.) in both cycles of an interleaved measurement). Those measurements allow the determination of the angles between the applied fields which is required for a full characterization of the electrode configuration.

constant field adds the constant projection E' to the parallel component of the background field $E_{0,\parallel} \rightarrow E_{0,\parallel} + E'$. Also B is now modified to B' to

$$B' = \sqrt{\Upsilon/A}\ (E_{0,\parallel} + E') = B + \sqrt{\Upsilon/A}E' \tag{3.15}$$

due to the additional applied constant voltage as well as 3.14 becomes

$$\Delta\nu(U)' - \Delta\nu(0)' = AU\left(U - 2(B + \sqrt{\Upsilon/A})E'\right) \tag{3.16}$$

The differential frequency shift of a measurement of Series 2.) and Series 1.) leads to the relation

$$[\Delta\nu(U)' - \Delta\nu(0)'] - [\Delta\nu(U) - \Delta\nu(0)] = \delta\Delta\nu \tag{3.17}$$

with $\delta\Delta\nu$ the differential frequency shift obtained from the clock measurement. This can be rewritten as

$$\delta\Delta\nu = \frac{AUE'}{\sqrt{A}} \tag{3.18}$$

where E' is the projection of the applied constant field to the applied field of the interleaved measurement (Fig. 3.19). The angle α enclosed by E' an E'_0 is given by

$$\cos(\alpha) = \frac{E'}{E'_0} \tag{3.19}$$

Such measurements with a constant applied field in both cycles are denoted e.g. "ANBS"/"$\widetilde{\text{ASBN}}$". Here the direction denoted with a tilde e.g. "$\widetilde{\text{ASBN}}$" is the direction where the constant field is applied to. Corresponding to this direction its parameters are denoted with tildes, such as $\widetilde{A}$ or $\widetilde{B}$ as well.

With the known relation from Eq. 3.18 and $E'_0 = \sqrt{\widetilde{A}}\widetilde{U}$ the angle in Eq. 3.19 can be written as

$$\cos(\alpha) = \frac{\delta\Delta\nu}{2U\widetilde{U}\sqrt{\widetilde{A}A}} \tag{3.20}$$

where $\widetilde{A}$ is the fit parameter in the direction of the applied constant voltage $\widetilde{U}$. Since Eq. 3.20 consists of user applied voltages and frequency shifts or parameters related to performed frequency shift measurements (A and $\widetilde{A}$) knowledge of the atomic properties that were included in Υ is not required. Also the geometry of the electrode arrangement is determined by evaluating frequency shift measurements and does not require geometric measurements. To calculation the angles between the other field directions one proceeds analogously using the corresponding parameters in Eq. 3.20. The found angles between the field directions in Sr3 can be found in Tab. 3.2.

Performing the two described measurement series in at least three directions of the available four (where the forth serves as consistency check) the angles of the respective field of each electrode pair enclosed with the background field $\vec{E}_{bgr}$can be determined. The setting up of the coordinate system can be found in the appendix (Sec. A.7).

3.5. Systematic frequency shift evaluation measurements

In the following sections the first measurements performed with Sr3 are described. This includes characterization measurements at room temperature that are relevant to determine the clocks total frequency shift as well as measurements at cryogenic temperature. The uncertainty budget can be found in Tab. 3.4. This chapter directly continues with the results of the dc Stark shift measurements which have been described above.

3.5.1. DC-Stark shift results

The measurements required to characterize the the electrode configuration and the resulting dc Stark frequency shift, were performed in January 2021. To evaluate temporal variations of the dc Stark shift measurements were performed regularly until mid of July 2021. In Fig. 3.20 the measured frequency shift is presented as a function of the applied voltage in one of the two cycles of an interleaved measurement. The parameters A and B obtained from the fit function (Eq. 3.14) are listed in Tab. 3.1.

With the additional constant field E'_0 applied to the opposite pair of electrodes (Series 2.)) the offset voltage B is affected due to the projection E' on the respective direction. A typical result of such a measurement is shown in Fig. 3.21. Here the parameter A of the direction "ANBS" was obtained from the respective measurement of Series 1.).

With the fit parameters A and B obtained by the characterization measurements the angles between the applied fields can be calculated with Eq. 3.20. The results are shown in Tab. 3.2.

Direction	A / $10^{-19} \cdot \mathrm{V}^{-2}$	B / V
ANBS	-1.88 (0.6)	4.29 (26)
ASBN	-2.19 (1)	9.93 (25)
AEBW	-1.28 (2)	2.89 (39)
AWBE	-1.49 (2)	7.63 (39)

Table 3.1.: Parameters A and B derived from the fit function (Eq. 3.14) applied to the experimental results from January 2021. The uncertainties of A are the standard errors given by the fit function. The uncertainty of the offset voltage B is determined by using Gaussian error propagation of Eq. 3.14. The fits to the results given in this table are illustrated in Fig. 3.20.

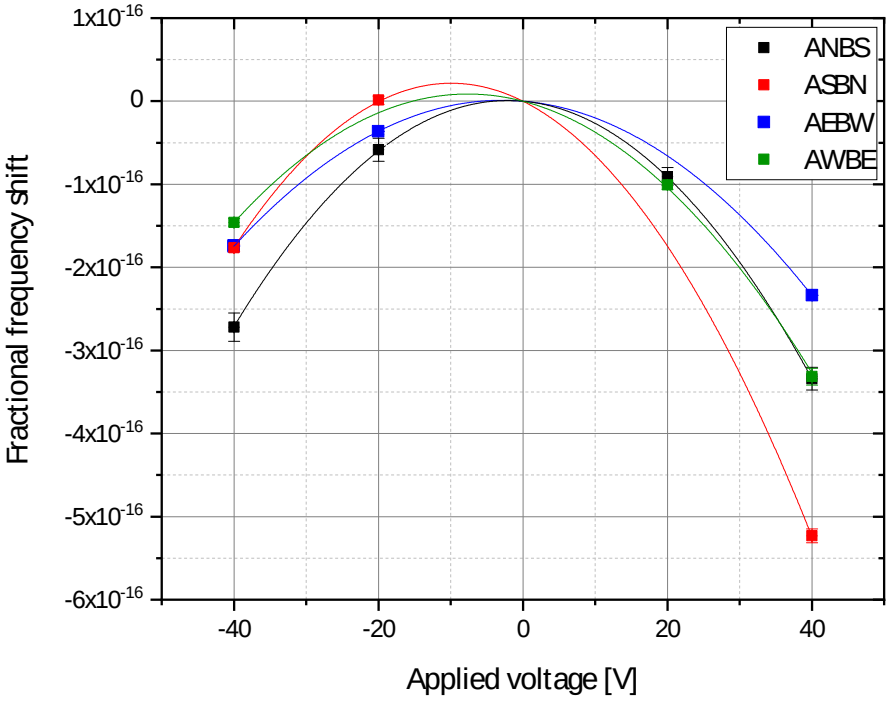

Figure 3.20.: Results of the first series of characterization measurements where in one of the two cycles of an interleaved measurement a voltage of applied (colored dots). The data is fitted using Eq. 3.14 (colored lines) with parameter A and B as free parameters and the restriction $\Delta\nu(U = 0\,\mathrm{V}) = 0$. The parameter A is related to the geometric properties of the electrode arrangement, whereas B is the offset voltage at the parabolas zenith.

Electrodes	angle
$\sphericalangle_{\mathrm{ANBS,\ ASBN}}$	133.6° (±1,4°)
$\sphericalangle_{\mathrm{ANBS,\ AEBW}}$	68.8° (±1.9°)
$\sphericalangle_{\mathrm{ASBN,\ AEBW}}$	94.9° (±2.2°)
$\sphericalangle_{\mathrm{ANBS,\ AWBE}}$	90.9° (±2.3°)
$\sphericalangle_{\mathrm{ASBW,\ AWBE}}$	69.0° (±1.6°)

Table 3.2.: Angles between the direction of the respective electrode pairs. From the results of the two measurement series the angles have been determined using Eq. 3.20. Their uncertainties are estimated by Gaussian error propagation (Eq.3.21).

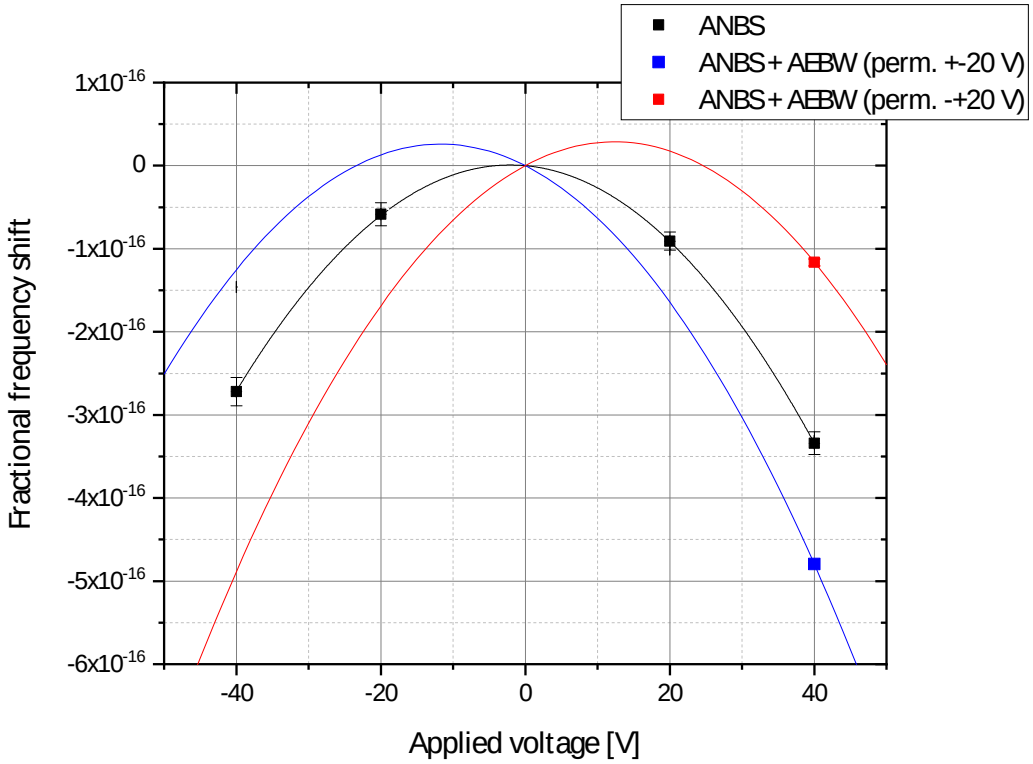

Figure 3.21.: Measurement results of a typical Series 2.) measurement. The electrode pair "ANBS" without a constant applied field on AEBW (black) is shown as reference. The blue (red) data are measurement result with an applied constant field of $\pm 40\,\mathrm{V}$ ($\mp 40\,\mathrm{V}$) at the electrode pair "AEBW". Solid lines are fits obtained from Eq. 3.14. The additional field affects the offset voltage B is affected due to the projection E' on "ANBS" which shift the parabolas accordingly.

	$\hat{e}_1$	$\hat{e}_2$	$\hat{e}_3$	$\hat{e}'_3$
a	1 (0)	-0.678 (18)	0.366 (31)	-0.015 (40)
b	0 (0)	0.735 (17)	0.224 (51)	0.474 (45)
c	0 (0)	0 (0)	0.903 (18)	0.881 (24)

Table 3.3.: Projections of the field vectors towards the reference direction "ANBS". The vector $\hat{e}'_3$ can be used as a consistency check.

As mentioned previously defining $\hat{e}_1$ along the "ANBS" direction as the first base vector, the parameters a, b and c can be calculated by the equations A.2, A.4, A.6. The projection of the individual vectors towards $\hat{e}_1$ can be seen in Tab. 3.3.

The field in the a given direction is described by Eq. 3.13. Again one does not require knowledge about atomic properties or the geometry of the electrode configurations. Eq. 3.13 directly gives the product $\sqrt{\Upsilon} \cdot E_0$ for this. It is the product that is important to know not the factors.

The field vectors are than constructed from the fields and the corresponding vectors given in Tab. 3.3.

From the latest measurement taken in mid of July 2021 a dc Stark shift of $\Delta\nu_{\mathrm{dcStark}} = -1.8(16) \cdot 10^{-18}$ was found which is added to the clocks uncertainty budget (Tab. 3.4).

3.5.2. Shift uncertainty estimation

The errors for certain parameters have already been given in he previous section without describing how those errors have been obtained to not disturb readability. In this section the description on how they have been obtained is given. To determine the uncertainty of found dc Stark shift $\Delta\nu_{\mathrm{dcStark}}$ several sources of potential uncertainties are investigated. Uncertainties related to the experimental setup are basically found in the uncertainty of the applied voltage U since this is the only systematic effect that is not common mode rejected in the two interleaved cycles. Additionally the uncertainties of the measurement results e.g. the parabola fit parameters A and B, are considered in the calculation of the uncertainty of $\Delta\nu_{\mathrm{dcStark}}$. A step-by-step analysis will be presented yielding in an estimation for the uncertainty of $\Delta\nu_{\mathrm{dcStark}}$. For the sake of simplicity, correlations are not considered.

The applied voltage was measured with a calibrated Agilent 34401A digital multimeter allowing a measurement uncertainty of 0.0015% for DC voltages. Typical variations in the output voltage of the power supply units during each clock measurement were observed to be below 10 mV. A significant drift during the measurements does therefore not occur. The uncertainty on the applied voltages throughout each measurement are therefore assumed to be not greater than ±5 mV. Its impact on the resulting angle is negligible.

To obtain the geometric parameter A and the offset voltage B from the fit function Eq. 3.14 for the individual directions of the electrode pairs, three interleaved measurements have been performed. These measurements were performed in a straight consecutive way to minimize an influence of a potential time dependency of the background field $\vec{E}_{bgr}$ on the results.

Uncertainties of the angles

The uncertainty of the angles between any of the applied fields (denoted α in the following equation) e.g. "ANBS" and "ASBN" is estimated by GEP of Eq. 3.20.

For using GEP to estimate the error in the angles all five parameters in Eq. 3.20 need to be derived. Since the uncertainties of U and $\tilde{U}$ are equal as well as the uncertainties of A and $\tilde{A}$ are similar enough to be considered equal, the derivatives shorten to and one term clearly dominating the uncertainty, $\delta\cos(\alpha)$ reduces to

$$\delta\cos(\alpha) \approx \sqrt{\left(-\frac{1}{\sqrt{\tilde{A}A}\,\tilde{U}U}\cdot\sigma(\partial\Delta\nu)\right)^2} \tag{3.21}$$

with $\sigma(\partial\Delta\nu)$ the statistical uncertainty of the corresponding interleaved clock measurement of Series 2.) For completeness, the complete formula can be found in the appendix (Sec. A.7.2, Eq. A.14). From Eq. 3.21 one can see that to reduce the uncertainty on α one can either apply larger voltages $U, \tilde{U}$ or by reducing the statistical uncertainty of the interleaved measurement (e.g. by increasing the measurement duration).

Determining the uncertainty of the vectors is analog. In the chain of the evaluation of the uncertainties of the following parameters it turned out that the uncertainties of the

vectors do not contribute significantly to the total uncertainty of $\vec{E}_{bgr}$. They are mostly included in terms that can be neglected because of little contribution. In this process only $\delta\hat{e}_{3,c}$ and $\delta\hat{e}'_{3,c}$ enter in the uncertainty of E_3 and E'_3. The derivation can be found in the appendix.

Uncertainties of the offset voltage B

The uncertainty of the offset voltage B is estimated by GEP on Eq. 3.14.

$$\delta B = 0.5\sqrt{\left(\frac{1}{AU}\cdot\sigma(\Delta\nu)\right)^2+\left(-\frac{\Delta\nu}{A^2U}\cdot\delta A\right)^2+\left(\left(-\frac{\Delta\nu}{AU^2}-1\right)\cdot\delta U\right)^2} \tag{3.22}$$

with $\sigma(\Delta\nu)$ the statistical uncertainty of the corresponding interleaved measurement, δA the uncertainty of the fit parameter given in 3.1 and δU the uncertainty of the applied voltage. It turns out that the first term dominates the uncertainty δB since it is three (fife) orders of magnitude larger than the second (third) term. So Eq. 3.22 simplifies to

$$\delta B = 0.5\sqrt{\left(\frac{1}{AU}\cdot\sigma(\Delta\nu)\right)^2} \tag{3.23}$$

Uncertainties of the fields

The uncertainty of the fields $\delta\left(\sqrt{\Upsilon}E_{0,\|}\right)$ are estimated by GEP on Eq. 3.13. The derivative

$$\delta\left(\sqrt{\Upsilon}E_{0,\|}\right) = \sqrt{\left(\frac{B}{2\sqrt{A}}\cdot\delta A\right)^2+\left(\sqrt{A}\cdot\delta B\right)^2} \tag{3.24}$$

can be reduced to

$$\delta\left(\sqrt{\Upsilon}E_{0,\|}\right) = \sqrt{A}\cdot\delta B \tag{3.25}$$

since the first therm is small enough to be negligible. This expression is valid for all directions and is therefore written without corresponding indices.

Uncertainties of the field vectors

The error on the field vectors follow the same approach but is more complicated for directions other than "ASBN" since the expressions are long-drawn-out. The full derivatives of the GEP of Eq. A.9 and Eq. A.11 are given in the appendix (Eq. A.21, Eq. A.22).

Again some therms insignificantly contribute to the uncertainty and are neglected, simplifying the expressions to

$$\delta E_1 = \delta \left(\sqrt{\Upsilon} E_{0,\parallel,\mathrm{ANBS}} \right) \tag{3.26}$$

$$\delta E_2 = \sqrt{\left(\frac{1}{\hat{e}_{2,b}} \cdot \delta(\sqrt{\Upsilon} E_{0,\parallel,\mathrm{ASBN}}) \right)^2 + \left(-\frac{\hat{e}_{2,a}}{\hat{e}_{2,b}} \cdot \delta E_1 \right)^2} \tag{3.27}$$

$$\delta E_3 = \sqrt{\left(\frac{1}{\hat{e}_{3,c}} \cdot \delta(\sqrt{\Upsilon} E_{0,\parallel,\mathrm{AEBW}}) \right)^2 + \left(-\frac{\hat{e}_{3,a}}{\hat{e}_{3,c}} \cdot \delta E_1 \right)^2 + \left(-\frac{E_1}{\hat{e}_{3,c}} \cdot \delta \hat{e}_{3,a} \right)^2} \tag{3.28}$$

Uncertainty of the dc Stark shift

Finally the uncertainty on $\Delta\nu_{\mathrm{dcStark}}$ can be given as:

$$\delta\Delta\nu_{\mathrm{dcStark}} = 2\sqrt{\left(E_1 \cdot \delta(\sqrt{\Upsilon}E_{0,\|}^{\mathrm{ANBS}})\right)^2 + \left(E_2 \cdot \delta(\sqrt{\Upsilon}E_{0,\|}^{\mathrm{ASBN}})\right)^2 + \left(E_3 \cdot \delta(\sqrt{\Upsilon}E_{0,\|}^{\mathrm{AEBW}})\right)^2} \tag{3.29}$$

Since the direction "AWBE" serves as a consistency check, replacing the last therm in Eq. 3.29 by $\left(E_3'\delta\left(\sqrt{\Upsilon}E_{0,\|}^{\mathrm{AWBE}}\right)\right)^2$ attributes its contribution to the frequency shift uncertainty $\delta\Delta\nu'_{DC-Stark}$. As seen in Fig. 3.22 both give consistent results that agree within their uncertainty. The final frequency shift presented in this work is given by the weighted average of the two calculated values.

Time dependence of the dc Stark shift

Apart from the characterization measurements, regular measurements were performed to investigate on a temporal variation in the offset field (fit parameter B). Throughout the year 2021 several of those measurements revealed that the offset voltages along the individual directions are changing (lower panel in Fig. 3.22). Nevertheless the offset voltage appears to cease and scatter around zero. For the direction "ANBS" (black trace in Fig. 3.22) it switched sign over time, which emphasis the necessity for regular validation measurements. The total frequency shift $\Delta\nu_{\mathrm{dcStark}}$ is evolving similarly (upper panel in Fig. 3.22). From a frequency shift of about $-7 \cdot 10^{-17}$ in January 2021 in reduced by more than an order of magnitude to $-1.8 \cdot 10^{-18}$.

The observed temporal variation of the offset voltage can be caused by a build-up of charges on non conduction surfaces. Such surfaces are e.g. dielectric coatings on windows on the windows of the cryostat. The inner shield has a total of eight windows with such coatings and their distance to the atoms is a few centimeter only.

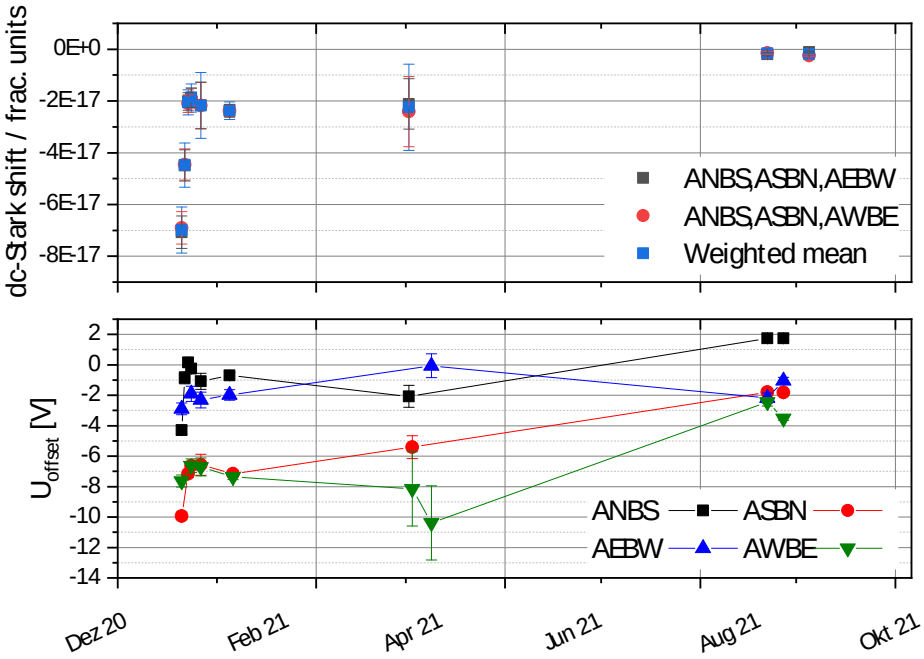

Figure 3.22.: Time evolution of the offset voltage $-B$ for each electrode pair and the resulting frequency shift experienced by the Sr-atoms. The observed time variance of the offset voltage may be caused by a build of charges on non conducting surfaces. The dc Stark shift appeared to stabilize around $-2 \cdot 10^{-17}$ in the first half of 2021 but significantly decreased to approx. $-1.8(5) \cdot 10^{-18}$ in July 2021. Notably the offset voltages of trace "ANBS" switched sign over time, which even more underlines the necessity for regular validation measurements.

3.5.3. Clock operation at cryogenic temperature

The first successful test of cooling the cryostat to cryogenic temperatures described in Sec. 3.2.5, demonstrated a homogeneous temperature distribution of the dual layer cryostat at either room- or cryogenic temperature. Cooling the environment is more or less "turn-key operation" since it only requires to run the pulse tube cooler. For the inner layer of the cryostat it takes about two days to reach a temperature of below $-185\,^{\circ}\mathrm{C}$ cryogenic temperatures and about half a day more for its temperature to reached stable conditions (Fig. 3.14). In this chapter first results of Sr3 operated at room- and cryogenic temperature are presented.

During one of the first attempts to cool the system to cryogenic temperature of about 80 K, the transportable clock, Sr2 was operated simultaneously. This allowed to observe the change in the Sr3 clock laser frequency due to the varying BBR induced frequency shift in a direct frequency comparison of the two clocks. Via a beat note the frequency difference of the Sr2 and Sr3 clock lasers are recorded by dead time free counters. Throughout the measurement the temperature of Sr2 was about 22 °C and fairly constant. Fig. 3.23 shows the time evolution of the frequency difference ($\nu_{\mathrm{Sr2}} - \nu_{\mathrm{Sr3}}$) of the two clocks while Sr3 was cooled down (purple). The temperature of Sr2 remained close to room temperature (green) throughout the measurement. With the theoretical model described in Sec. 2.6.2, the frequency shift with respect to the measured temperature in Sr3 was calculated (blue) and shows good agreement with the recorded frequency difference between the two clocks (black).

Several characterization measurements have already been performed at room temperature operation such as finding the operational magic wavelength, density shift or the dc Stark shift measurements. At cryogenic temperature a magic wavelength measurement was performed in March 2021 resulting in a frequency shift of $4.4(33) \cdot 10^{-18}$ between the two cycles of the interleaved measurement. This is in marginal agreement with the measurements presented below (Sec. 3.5.6). The temperature evolution and BBR shift uncertainty during the measurement can be seen in Fig. 3.24 (right). For comparison the left panel shows the same parameters at room temperature operation. Despite the uncertainty of the representative temperature is about a factor of 8 larger at cryogenic temperature compared to room temperature operation, the total BBR shift uncertainty reduces from $1.55 \cdot 10^{-18}$ to about $1 \cdot 10^{-18}$ at cryogenic temperature. The total BBR shift

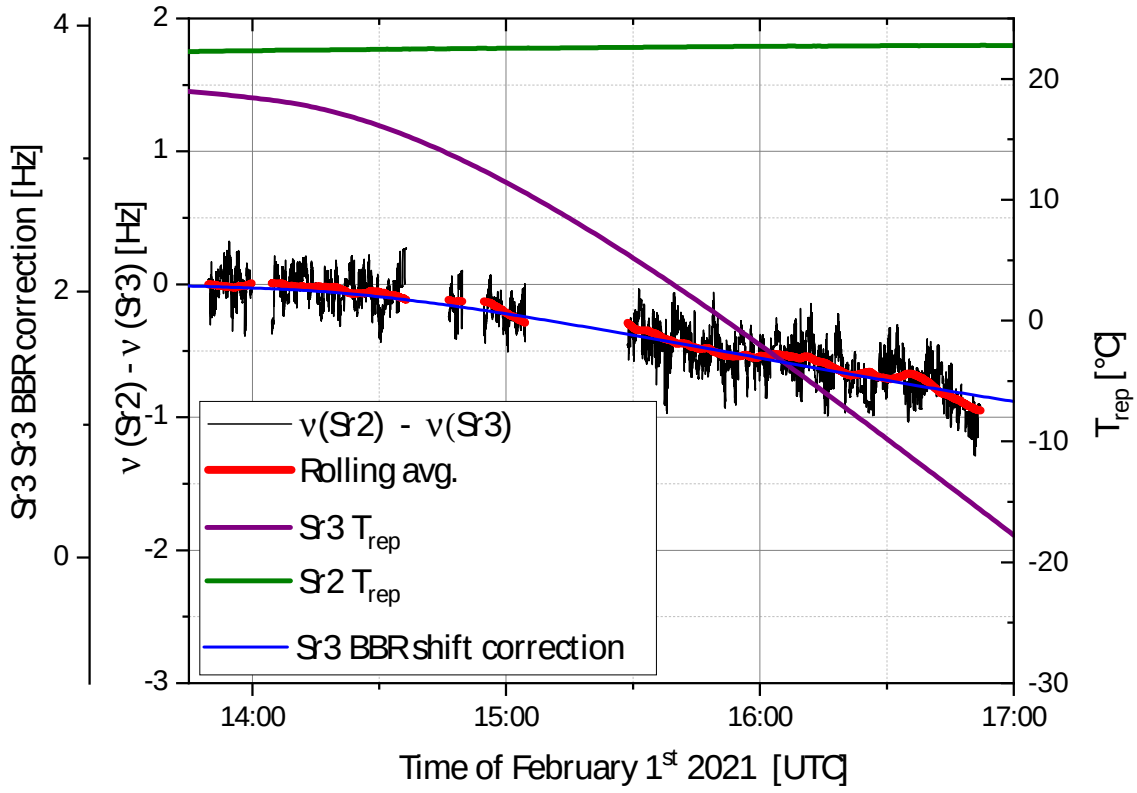

Figure 3.23.: Frequency difference between the transportable Sr-lattice clock Sr2 and Sr3 throughout one of the first attempts to cool Sr3 to cryogenic temperature. The temperature of Sr2 was kept constant, whereas the temperature of Sr3 dropped (purple line) from room temperature of about 18 °C to −18 °C. The frequency difference among the clocks changes due to the ceasing BBR shift in Sr3 (black line with rolling avg. in red). The change in transition frequency of Sr3 agrees to the calculation (blue line) from Eq. 2.22.

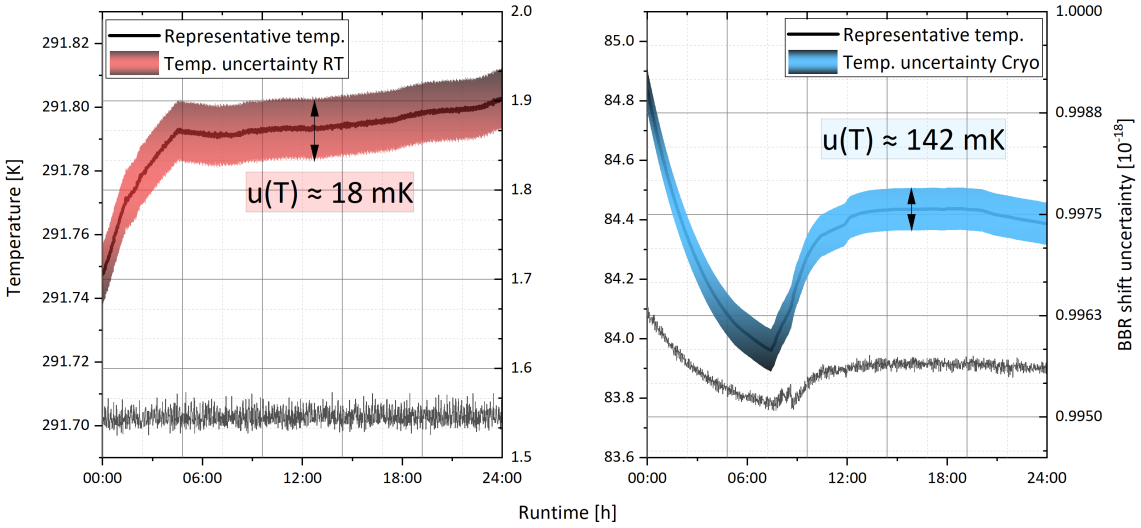

Figure 3.24.: Temperature measurement of the inner shield of the cryostat during clock operation at room temperature (left) and at cryogenic temperature of approx. 84 K (right). The temperature span of the inner shield is approx. 50 mK/450 mK at room/cryogenic temperature corresponding to a frequency shift uncertainty of $\approx 1.55 \cdot 10^{-18} / < 1 \cdot 10^{-18}$. The BBR uncertainty includes an operating temperature depending calibration uncertainty of the Pt100 sensors of 6 mK/20 mK, and a calibration uncertainty of 6 mK of the temperature measurement bridge. The total BBR uncertainty at cryogenic temperature is dominated by the BBR shift uncertainty contribution of the missing atomic beam shutters. With the shutters installed the total BBR shift uncertainty is expected to be below $3 \cdot 10^{-19}$.

uncertainty at cryogenic temperature is dominated by the uncertainty contribution due to the missing atomic beam shutters (Sec. 3.2.6). With the shutters installed the total BBR shift uncertainty is expected to be below $3 \cdot 10^{-19}$.

In Fig. 3.25 the total BBR shift uncertainty (red solid line) as a function of the cryostats inner shields temperature is visualized. It consists of the uncertainty contributions from the cryostat itself (black solid line) and from the unblocked holes due to the missing beam shutters (blue solid line). The intruding room temperature BBR of 293 K is attributed an uncertainty of 2 K which is a rather conservative estimation based on data from the laboratory climate control system that show temperature variation at the level of below 0.5 °C. Below a temperature of 40 °C of the cryostat, the uncertainty con-

tribution from the unblocked holes is dominating and further reduction of the cryostats temperature does not reduce the total BBR uncertainty below a level of about $0.95 \cdot 10^{-18}$. This is expected to change dramatically when the shutters are installed.

To estimate the total BBR uncertainty with installed shutters, their BBR shift uncertainty contribution is calculated based on an estimate of the shutters temperature. Compared to the situation without the shutters, where the intruding leakage was constant at room temperature for all cryostat temperatures, now the holes are covered by the shutters. Their temperature is coupled to the cryostats one. With decreasing temperature of the cryostat the shutters are temperature will follow due to radiative heat exchange into the support structure of the cryostat (sec. 3.2.1). From a thermal simulation a shutter temperature of approx. 130 K at a cryostat inner shield temperature of approx. 80 K is assumed. Additionally, at room temperature the cryostat and the shutters temperature are equal of course.

Based on that, the shutters temperature is linearly interpolated by $T_{\mathrm{shutter}} = f(T_{\mathrm{cryostat}}) = 0.756\, T_{\mathrm{cryostat}} + 68.86\,\mathrm{K}$. The shutter temperature uncertainty is attributed an uncertainty of 2 K which is the same as for the case without shutters. At the current state without the cryogenic shutters the clocks uncertainty reduces with decreasing temperature of the cryostat as seen in Fig. 3.25[11]. These assumptions lead to a temperature dependent BBR uncertainty contributions as depicted in Fig. 3.25. Although the temperature of the shutters is expected to be about 50 K warmer compared to that of the cryostat at 80 K, its uncertainty contribution (blue semicolon line) is never as dominant as without shutters. To reach the projected BBR uncertainty in the low 10^{-19} range the shutters must be installed. At present there is little necessity to work at cryogenic temperature since the uncertainty is only improving by about $< 1 \cdot 10^{-18}$. Nevertheless, in the previous discussion the uncertainty on the representative temperature of the cryostat is assumed to be 18 mK and constant for all temperatures. Its dependence on the cryostats temperature must be considered and measured experimentally.

[11] The temperature uncertainty of the cryostat in this model is const. = 18 mK

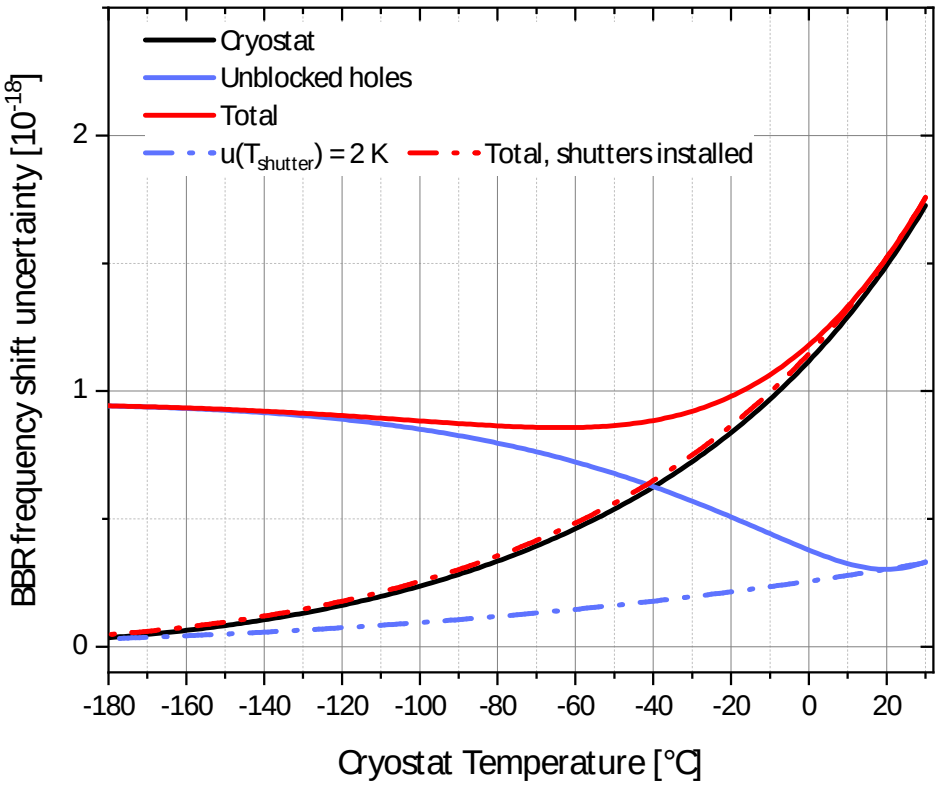

Figure 3.25.: BBR shift uncertainty contributions of the current Sr3 system at the present state without the cryogenic shutters (solid lines) and their estimated contribution with installed shutters (semicolon lines). At room temperature operation the uncertainty contribution of the missing shutters (blue solid line) is not relevant for the total BBR uncertainty (red solid line) since it is completely dominated by the cryostat. At this configuration a minimum uncertainty of about $0.85 \cdot 10^{-18}$ is expected for operation around $-60\,^{\circ}\mathrm{C}$. Surpassing this limit with installed shutters can be expected below an operating temperature of the cryostat of about $-30\,^{\circ}\mathrm{C}$ (red semicolon line) where the shutter contribution is not dominating at any temperature.

3.5.4. Background gas collision shift

In an optical lattice clock the atoms can only be trapped for a finite time commonly referred to as the lifetime in the optical lattice or in short "lifetime". It is defined as the 1/e decay time of a falling exponential function. In every vacuum chamber a non zero residual vacuum pressure exists. Atoms or molecules from the background gas can collide with the strontium atoms in the optical lattice eventually removing them from the trap. This leads to a reduction of the spectroscopic signal and may limit the probing duration which in turn degrades the clocks stability. Apart from that, background gas collisions can also cause a frequency shift on the clock transition commonly referred to as the "background gas collisional frequency shift" which contributes to the clocks total uncertainty. It can be determined by measuring the lifetime in the optical lattice.

For Sr1 an upper limit for the frequency shift has been estimated in [62] based on the procedure in [90]. This theoretical model relies on the determination of a phase changes due to scattering of clock atoms with most common background gas species (H, He, H2, Sr and Xe) found in ultra high vacuum applications. Recently the first experimental evaluation of the background gas collisional frequency shift was presented [91]. In the measurement the authors compared the transition frequency of two ^{87}Sr-lattice clocks where one serves as a stable frequency anchor. The other clock was operated at different hydrogen dominated background gas pressures with a corresponding lifetime of the atoms in the optical lattice. By comparing the clocks differential frequency for different lifetimes, a background gas collision frequency shift coefficient of $-30(3) \cdot 10^{-18}$, for a lifetime of 1 s, was found. For the determination of this frequency shift in Sr3, we rely on the model described above which requires to analyze the background gas composition first, to ensure the model can be applied here.

Residual gas analysis

For stainless steel vacuum chambers such as the Sr3 system the largest residual partial pressure is typically from hydrogen. To verify this assumption a residual gas analysis was performed using the PrismaPro QMG 250 F1 quadrupole mass spectrometer attached to the vacuum chamber (Fig. 3.1). It measures in a mass range from 1 to 100 atomic mass units with a detection threshold of $4 \cdot 10^{-13}$mbar. With the pressure in the Sr3 vacuum

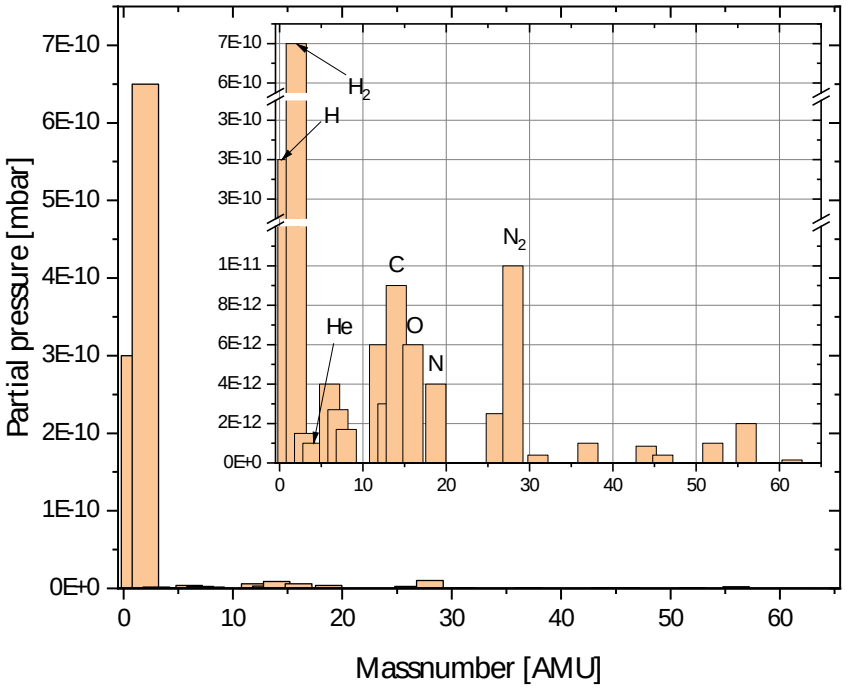

Figure 3.26.: Residual gas analysis of the Sr3 clock. Besides little contribution from several gases from atmosphere Hydrogen is the dominant component.

chamber is typically in the range of $1..10 \cdot 10^{-10}$mbar therefore the quadrupole mass spectrometer is a suitable analyzer for the background gas composition. The measurement result seen in Fig. 3.26 reveals that the partial pressure from hydrogen (H and H_2) is by far the most dominant gas species of the total pressure that was about $1 \cdot 10^{-9}$mbar at the time of the measurement. Therefore it is legit to rely on the frequency shift evaluation based on the work of [91] described above. The determination of the lifetime in the optical lattice is described in the next section.

Lifetime in the optical lattice

The residual gas analysis described in the previous section revealed a gas composition dominated by Hydrogen by far which allows to evaluation of the background gas collisional shift based on the work of [91] which additionally requires to know the lifetime in the optical lattice. To measure the lifetime atoms are loaded into the optical lattice and are hold there for variable times with subsequent detection of the remaining fraction. The lattice potential depth is hereby identically to that of common clock operation which is the shallow potential depth ($77E_{rec}$). Considering a constant loss of atoms from the lattice over time, an exponential decay can be expected with its 1/e-value derived as the lifetime.

The measurement results in Fig. 3.27 show the remaining populations as a function of holding time in the optical lattice. The pressure in the chamber throughout the measurements was about $5 \cdot 10^{-10}$mbar.

In total three different measurements were conducted. Two with the cryostat operated at room temperature and one at cryogenic temperature. The two measurements at room temperature have been performed with different number of trapped atoms. One with the highest number of trappable atoms (red dots) the other with about 30% (black dots) of that. The measurement at cryogenic temperature (green dots) was performed with the maximum number of atoms that could have been trapped which was still lower than the measurement at room temperature with reduced number of atoms. The solid lines in Fig. 3.27 correspond to 1/e fit functions. The expected population dynamic follows an exponential decay of the form

$$N(t) = N_0 \cdot \exp(-t/\tau) + N_{\mathring{off}} \tag{3.30}$$

with N_0 the initial number of atoms at $t = 0\,\mathrm{s}$, τ the 1/e lifetime in seconds and $N_{\mathring{off}}$ an offset parameter to force the fit to converge to an atom number of zero at infinite hold time. However, for the measurements performed only that at room temperature (red in Fig. 3.27) with a reduced number of atoms shows a 1/e decay (linear progress in the logarithmic plot). For the measurement with the maximum number of atoms, a 1/e fit (black dotted line in Fig. 3.27) clearly does not match the measurement data.

Therefore the fit function is modified to attribute an additional loss factor a in units of $1/\mathrm{s}^2$ to

$$N(t) = N_0 \frac{\exp(-t/\tau)}{1 + \tau a N_0 (1 - \exp(-t/\tau))} + N_{\mathrm{off}} \tag{3.31}$$

The results when using Eq. 3.31 as fit function are listed in Tab. 3.5.4. For the measurement with high atom number (black) using Eq. 3.31 as fit function, leads to a lifetime of approx. 9.1(32)s including a two body loss rate of $-3.8(5)\cdot 10^{-5}$ $1/\mathrm{s}^2$. Apart for the atom number the measurement with reduced atom number (red) is performed under the same conditions. Here $a_{RT,30\%}$ is a positive value which is unphysical since it represents a growth. So a will be restricted to values below or equal to zero. Then the fit resulted in a lifetime of about 7.8(4)s which is the lowest of all the measurements. The measurement at cryogenic temperature was held about a month later and featured a fresh setting up of the clock. This includes a realignment of the two MOTs and the lattice laser beam, as well as a new set of parameters for the magnetic field compensation. This was necessary because when reducing the temperature of the cryostat the number of trapped atoms continuously decreased with temperature to finally zero. After reaching a temperature of about 80 K trapping atoms required the steps described above. The maximum number of captured atoms in the lattice (green) was significantly lower compared to the one performed at room temperature with reduced number of atoms (red). Surprisingly one finds a two body loss rate more than eight times larger and a comparatively large lifetime of 14.6(22)s. A longer lifetime at cryogenic temperature was expected due to the better background gas pressure in the inner shield of the cryostat. The origin of the significantly larger two body losses has not been resolved yet but has to be considered for future determination of the collisional shift by measuring the lifetime in the optical lattice. All measurements share the non 1/e decay and are suspected to suffer additional loss from a source other than background gas collisions. Whereas the data at room temperature with reduced number of atoms (red) is closest to it. Considering a global increase in atom number throughout this measurement series may explain the tendency towards a positive value of $a_{RT,30\%}$.

Until now the atoms have not been spin polarized in the measurement. A high lattice site occupation may occur and potentially introduce severe in-site collisional losses. Therefore measuring the population dynamics with spin polarized atoms was performed (purple in Fig. 3.27) to suppress multiple atomic occupation per lattice site. The fit reveals

Op. Temp.	Color	Atom No.	τ [s]	Frequency shift [10^{-18}]	a [10^{-5}/s^2]
Room Temp.	black	Max.	9.1(32)	-3.3(4)	-3.8(5)
Room Temp.	red	30%	7.8(4)	-3.8(4)	0(8)
Cryogenic	green	Max.	14.6(22)	-2.1(4)	-32(7)
RT (Spin polarized)	purple	Max.	8.2(3)	-3.7(4)	-8.7(14)

a similar two body decay rate as for the black data points that is suspected to have had a higher atomic density. Additionally the number of spin polarized atoms was comparable to the measurement with a reduced number of atoms (red) which is supposed to have had a lower atomic density compared to the measurement with a maximum number of atoms (black). In therms of atom density in the lattice, it is likely that the spin polarized ensemble (purple) is comparable to that of the measurement with a reduced number of atoms (red). In terms of lifetime their results are comparable. However for the spin polarized sample, in-site collisional losses can be ruled out. If this is the origin for the additional loss therm, $a_{RT,sp}$ would be compatible with zero which is not the case.

The measurement conducted at cryogenic temperature (green) revealed a high two-body loss compared to those at room temperature. For further investigating it is plausible to perform a measurement at cryogenic temperature with a spin polarized atomic ensemble. Unfortunately the atom number of the spin polarized ensemble was insufficient at that time.

The background gas collision shift at room temperature was determined to $-3.8(4) \cdot 10^{-18}$ based on the shortest lifetime measured of 7.8(4)s. At cryogenic temperature the lifetime was determined to 14.6(22)s which corresponds to frequency shift of $-2.1(4) \cdot 10^{-18}$. The difference in the resulting frequency shift of whether cryogenic or room temperature operation is about $1.7 \cdot 10^{-18}$ and is added in the clocks uncertainty budget in Tab. 3.4.

The large discrepancy in the frequency shifts at the two different operating temperatures requires mandatory measurements of the lifetime, especially when changing from one operational temperature to the other.

For future evaluation of the background gas collisional shift by measuring the lifetime in the optical lattice, a protocol on how to treat the two-body losses and what their origin is must be worked out. Otherwise it may become a significant contribution in the clocks total uncertainty.

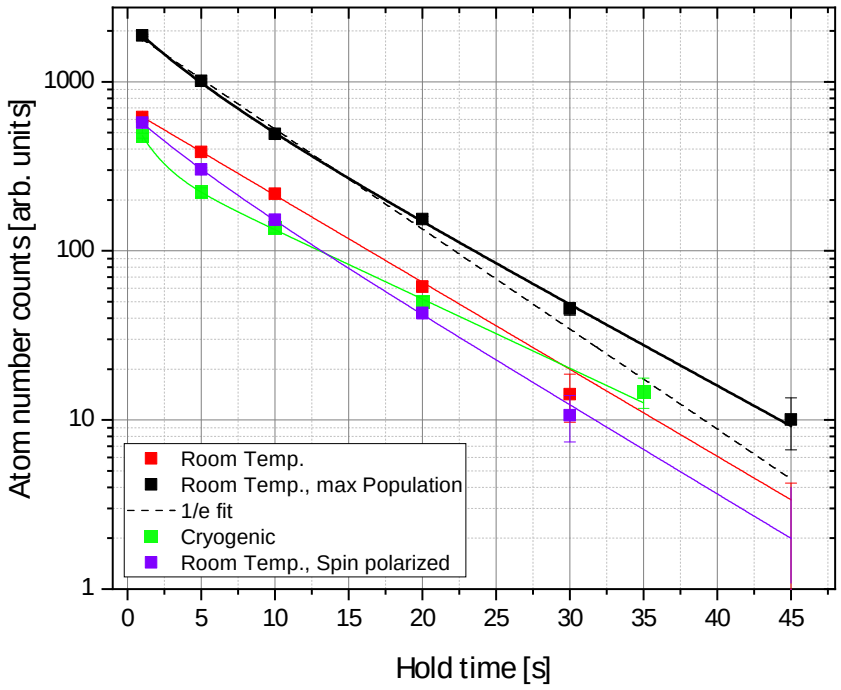

Figure 3.27.: Population of atoms trapped in the optical lattice as a function of holding time. The development of the atom number is expected to follow a 1/e decay over time, which is clearly not the case for most of the measurements (black, green, purple). Such measurements suffer from an additional loss where the origin is unclear. The measurements performed at a cryostat temperature equal to room temperature (dots in black, red, purple where black data points are fitted by a 1/e fit function shown as dotted line). The solid lines are fits using Eq. 3.31 to obtain τ and a. From the measurements a lifetime is derived of approx. 7.8(4)s for room temperature operation and 14.6(22)s at cryogenic temperature. The vacuum pressure in the chamber during the measurements was about $5 \cdot 10^{-10}$ mbar measured with the vacuum meter.

3.5.5. Sideband spectroscopy

To determine the lattice light shift and its uncertainty, the axial T_z and radial T_r temperature of the atoms trapped in the optical lattice must be determined. They can be estimated by sideband spectroscopy on the ${}^1\mathrm{S}_0 - {}^3\mathrm{P}_0$ clock transition. The evaluation is based on the model developed in [39] and is described in Sec. 2.3. Sideband spectroscopy in Sr3 is performed at the spectroscopy lattice depth. Hereby an axial frequency of approx. $\nu_z = 61\,\mathrm{kHz}$ was found. (red curve in Fig. 3.28) which corresponds to a lattice potential depth of approx. $U = (\nu_z/2\nu_{rec})^2 = 76E_{rec}$. From the model in [39] one obtains an axial temperature of $T_z = 5.2\,\mu\mathrm{K}$ and a radial temperature of $T_r = 8.7\,\mu\mathrm{K}$.To reduce the temperature further, a technique called "spilling" (Sec. 2.5) was used. Here the potential depth is lowered adiabatically to approx. $22E_{rec}$ for 40 ms and subsequently ramped to the spectroscopy depth. Atoms occupying a vibrational state of $v_z \leq 2$ and therefore have a high temperature become untrapped due to the low potential depth during "spilling". This results in lower temperature of the remaining ensemble. This was verified in an additional measurement (blue curve in Fig. 3.28) where a temperatures of about $T_z = 2.2\,\mu\mathrm{K}$ and $T_r = 4.5\,\mu\mathrm{K}$ have been determined. The same measurement was performed at the deep lattice depth in the magic wavelength characterization measurements. The axial and radial temperatures at the deep lattice potential T_z' and T_r' are relevant parameters in the evaluation of the lattice light shift. From such a sideband spectroscopy measurements one finds $T_z' = 5.2\,\mu\mathrm{K}$ and $T_r' = 5.8\,\mu\mathrm{K}$ as well as an axial frequency of approx. $\nu_z' = 86\,\mathrm{kHz}$ which corresponds to a potential depth of $U' = (\nu_z/2\nu_{rec})^2 = 148E_{rec}$

Compared to the results obtained without "spilling' the lattice light shift changes from $15.6(212)\cdot 10^{-18}$ to $-3.7(20)\cdot 10^{-18}$ which is a huge improvement in its uncertainty. Further use of "spilling" to even lower potential depths e.g. of approx. $10E_{rec}$ leads to even lower temperatures of $T_z = 0.9\,\mu\mathrm{K}$ and $T_r = 2.9\,\mu\mathrm{K}$ which results in a lattice light shift of $-3.4(26)\cdot 10^{-18}$. The uncertainty thereof is now dominated by the large uncertainty of the differential E2/M1 coefficient α^{qm} our group uses which stems from how we account for the large discrepancy in the reported values published in [51,53,55]. This will be discussed below in more detail. Unfortunately "spilling" to a potential depths of approx. $10E_{rec}$ reduces the number of atoms too severe for clock operation. Other techniques are required to reduce the atoms temperature such as sideband cooling. Axial sideband cooling has been investigated recently and successfully tested in our group, but is beyond the scope

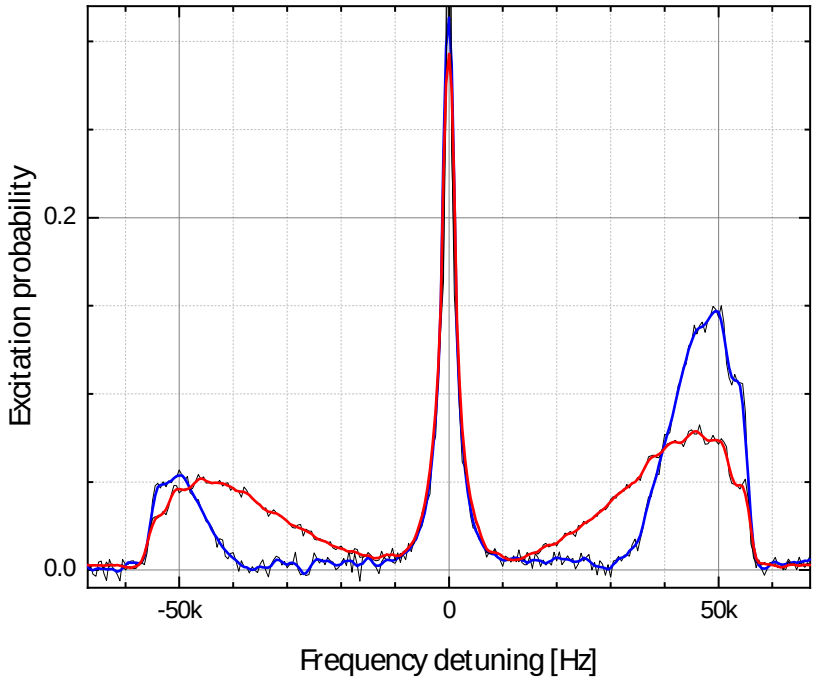

Figure 3.28.: Longitudinal sideband spectroscopy on the $^1S_0 - {}^3P_0$ clock transition without (red) and with (blue) "spilling" (described in the text) the atoms before spectroscopy. The "spilling" technique reduces the temperatures from $T_z = 5.2\,\mu K$, $T_r = 8.7\,\mu K$ to about $T_z = 2.6\,\mu K$, $T_r = 5.8\,\mu K$ and greatly improves the lattice light shift uncertainty to about $2 \cdot 10^{-18}$.

of this work.

3.5.6. Lattice light shift

To determine the effective detuning from the "operational magic wavelength", several interleaved measurement have been performed. The lattice potential depth during spectroscopy was altered between approx. $U_0' = 122\ E_{rec}$ (deep lattice) and approx. $U_0 = 64\ E_{rec}$ (shallow lattice) in the two interrogation cycles. This type of measurements are commonly called magic wavelength (MWL) measurements. For frequency stabilization the lattice laser was locked to the frequency comb at a constant offset frequency. Throughout December 2020 and February 2021 several magic wavelength measurements haven been performed where the clock was operated at either room temperature or cryogenic. Fig. 3.29 shows the measured frequency shifts. Except for one measurement they agree within $7 \cdot 10^{-18}$ with day-to-day variations of typically well below that level. Combining all the measurement performed with the clock operated at room temperature (red shaded area) the total measurement duration reaches approx. 60 h. The average light shift obtained from this extended dataset is about $+1.6 \cdot 10^{-18}$ as seen as the first red dot in Fig. 3.29. The total Allan deviation of the combined data set is depicted in Fig. 3.30 showing an instability of $2.1 \cdot 10^{-16}\ /\sqrt{\tau}$. This leads to a statistical measurement uncertainty of $4.5 \cdot 10^{-19}$. Following the evaluation of the "operational magic wavelength" protocol described in [53] the lattice light shift at its operational depth of about $U_0 = 64\ E_{rec}$ is calculated to $-3.8(20) \cdot 10^{-18}$ and added to the clocks uncertainty budget. The required axial/radial temperatures for the determination of the light shift have been presented in the previous section (Sec. 3.5.5).

MWL measurements have also been performed at cryogenic operation. Here from the two measurements performed, as seen in Fig. 3.29 in the blue shaded area, an average light shift of $8.4(22) \cdot 10^{-18}$ was obtained (red dot in between the two measurements). The two measurement results obtained are in marginal agreement within their uncertainty. Although the are covered within the scatter of the frequency shift results obtained at room temperature their weighted average values (red dots) differ significantly and are not in agreement within a 3σ uncertainty.

The discrepancy among the average results may be due to a lack of measurements performed at cryogenic temperature. Nevertheless there are potential circumstances under which the lattice light shift can be different among the two operational temperatures which is investigated in the following.

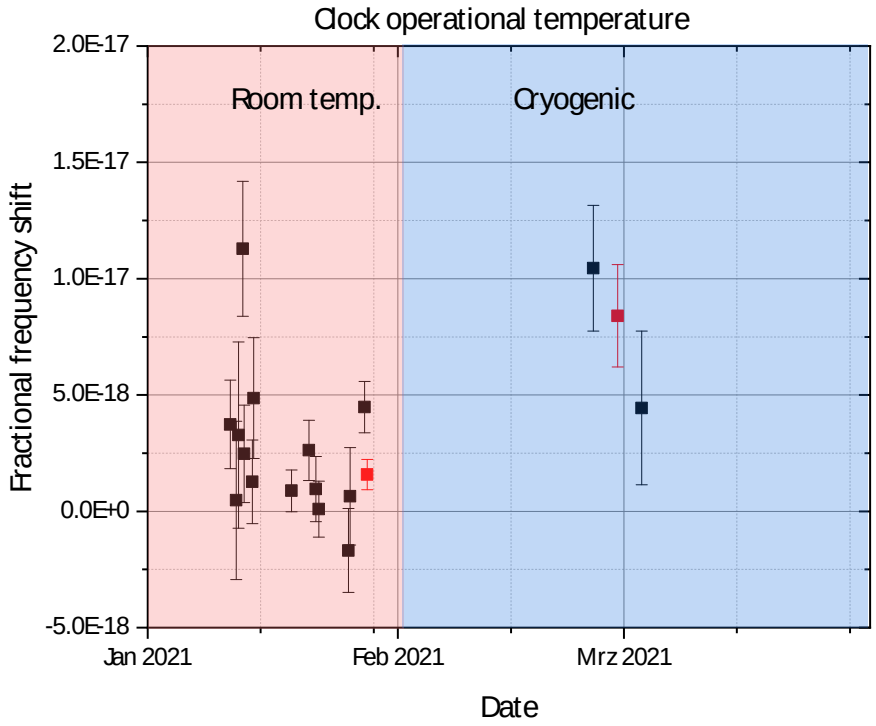

Figure 3.29.: Time evolution of the frequency shift obtained in magic wavelength measurements. The optical lattice was operated near the magic wavelength with the potential depth alternating between $U_0' = 122\ E_{rec}$ (deep) and $U_0 = 64\ E_{rec}$ (shallow). Its frequency has not been changed throughout all measurements. The measurements have been performed with the clock being operated at room temperature (red shaded area) and cryogenic temperature (blue shaded area). Red data point represent the average frequency shift for either room temperature- or cryogenic clock operational temperature. Uncertainties are given by the total Allan deviation.

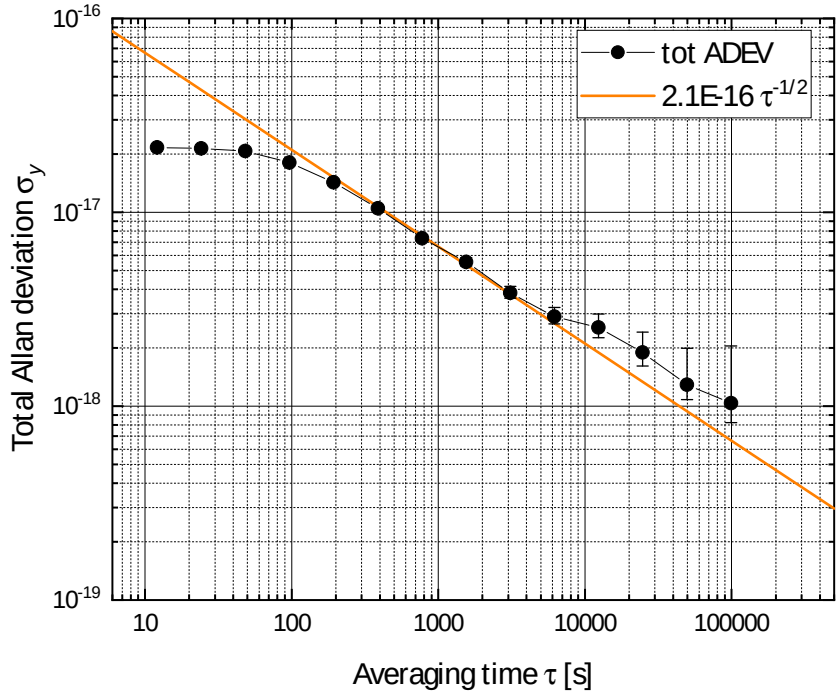

Figure 3.30.: Total Allan deviation of the magic wavelength measurements performed in January/February 2021 where the clock was operated at room temperature. The total measurement duration sums up to approx. 60 h with an instability of approx. $2.1 \cdot 10^{-16}$ $1/\sqrt{\tau}$. The average light shift of the extended dataset is $1.6 \cdot 10^{-18}$ with a statistical uncertainty of $4.5 \cdot 10^{-19}$.

When operating the cryostat at cryogenic temperature, stress induced birefringence in the windows attached to the cryostat may occur due to the difference in thermal expansion coefficients of the copper/indium/N-BK7 material combination (CTE = 17/44/7·10^{-6}/K). In Sr3 a polarizing beam splitter (PBS) with an extinction ratio of 1:10000 is installed behind the fiber that delivers the light from the Ti:Sa lattice laser to the vacuum chamber. This ensures best linear polarization which is ideally aligned along the bias magnetic field direction applied during spectroscopy. Nevertheless uncontrolled changes of the lattice polarization can lead to significant frequency shifts.

Considering the electric dipole (E1) interaction as described in [51], the frequency shift $\Delta\nu^{E1}$ can be decomposed into scalar ($\Delta\nu^{sc}$), vector ($\Delta\nu^{vec}$) and tensor ($\Delta\nu^{ten}$) shift contributions where $\Delta\nu^{vec}$ and $\Delta\nu^{ten}$ are sensitive to the lattice polarization. The vector shift vanishes if at least one of the following conditions are met: i) the lattice beam polarization is perfectly linear, or ii) the bias magnetic field direction is perfectly orthogonal to the lattice beam propagation direction. Therefore such conditions are favorable operational parameters for clock operation. In fact those ideal conditions are difficult to fulfill. In a typical magic wavelenght measurement performed with Sr3 so far, a differential vector shift $\delta\nu^{vec}$ between the two interrogation cycles have always been observed. The vector shift dependents linear on the lattice potential depth U_0. Thus in a MWL measurement it appears as a difference in magnetic field splitting B_{split} of the Zeeman components used for spectroscopy ($m_F \pm 9/2$ in this case) between the two interrogation cycles. In the following the vector shift is determined by $\delta\nu^{vec} = B_{split}(U_0') - B_{split}(U_0)$.

The MWL-measurement at cryogenic temperature on the 25$^{\text{th}}$ of February (Fig. 3.29, was performed during the cooldown of the cryostat and did not have had stable temperature conditions as seen in Fig. 3.31. The cryostats inner shield temperature was declining from $-135\,^{\circ}$C to about $-170\,^{\circ}$C in approx. 4.5 h. Over the course of the measurement the differential vector shift $\delta\nu^{vec}$ changed from about 100 mHz to -250 mHz between the two cycles of the interleaved measurement with a change in sign at a temperature of about 133 K.

While operating the cryostat at stable room temperature conditions, the differential vector shift was observed to be always negative (red shaded area in the upper panel of Fig. 3.31). At cryogenic clock operation however (blue shaded area in Fig. 3.31), the

vector shift turned positive. This indicates a change in the orientation between the lattice polarization and the bias magnetic field.

Beneficial about the vector shift is, that during clock interrogation of the $m_F \pm 9/2$ Zeeman substates it cancels similar to the linear Zeeman shift. Nevertheless the observed change of the vector shift induced by the cryostats temperature does imply non stable behavior either of the lattice polarization or of the bias magnetic field orientation. The latter is very unlikely since the magnetic field generating coils are mounted outside the vacuum chamber and therefore their temperature is not affected by the cryostats temperature. A variation of the lattice polarization is most likely originated by temperature dependent mechanical stress induced birefringence of the windows attached to the cryostat.

In contrast variations in the tensor shift $\Delta\nu^{ten}$ cannot be observed in the running experiment like the vector shift. But it can also be subject to a frequency shift on the clock transition. For common orientations of a linear polarized lattice either perpendicular or parallel to the bias magnetic field, $\Delta\nu^{ten}$ is always non zero. Typically $\Delta\nu^{sc}$ is adjusted by the lattice frequency such that it balances $\Delta\nu^{ten}$ to $\Delta\nu^{sc} + \Delta\nu^{ten} = 0$. This operating condition where $\Delta\nu^{E1} = 0$ is called the "Stark-cancellation wavelength".

Following up on the idea that an uncontrolled change in the angle between the lattice polarization and the bias magnetic field can cause an unnoticed frequency shift, lets discuss a gedankenexperiment. Assuming the lattice polarization to be ideally linear but the angle to the bias magnetic field vector free of choice. As already discussed the deviation in the measured frequency shifts of the MWL measurements between room temperature- and cryogenic operation (red squares in Fig. 3.29) is about $7 \cdot 10^{-18}$. The difference in the potential depth between the two cycles is hereby about 58 E_{rec}. An equal light shift exclusively originated from the tensor shift contribution, would require a change in the angle between the linear polarization of the lattice and the bias magnetic field from 0° to about 5° at the typical spectroscopy potential depth of 76 E_{rec}. As already mentioned, stress induced birefringence is likely to happen when optical elements are changing its temperature which are bonded to materials with different thermal expansion coefficients which is the case here[12]. Here, for simplicity it is further assumed that the change in angle due to stress induced birefringence is induced by such windows attached to the cryostat, that the lattice passes before impinging the atoms, (Fig. 3.9) only. After the lattice light

[12]Thermal expansion coefficients of the copper/indium/BK7 combination is 17/44/7 $\cdot 10^{-6}$/K

is retro reflected it double passing these windows. This effectively doubles the angle but it happens behind the atoms so the tensor shift results from the single angle only.

A change in the lattice polarization's angle will affect the transmission of the retro reflected light passing through the PBS that is mounted after the lattice fiber (Fig. 3.2). After double passing the birefringent element(s) the transmission would remain at $\cos^2(2 \cdot 5°) = 0.97$ which is likely to be undetected during clock operation. The power stabilization loop of the lattice laser will compensated the power drop which increases the in optical power delivered to the atoms and raising the potential by about $1.45E_{rec}$. This translates to an increase in the axial sideband frequency of well below 1 kHz for the common lattice potential of about $76E_{rec}$. This variation is too small to be detected by sideband spectroscopy. To compensate the change in the tensor shift with an equal but opposite in sign scalar contribution, the lattice frequency requires to be adapted by about 2 MHz. In conclusion regular characterization measurements are compulsory to verify that the total lattice light shift have not changed, especially when the operational temperature of the clock is changed. Regarding this it is not a surprise that the last measurement in Fig. 3.31 shows a significant different differential vector shift as those observed at room temperature.

Treatment of the E2/M1 polarizability and outlook

Unfortunately there is a huge discrepancy in the value of the E2/M1 polarizability α^{qm} published in recent literature[13]. To attribute this discrepancy the weighted mean values are applied leading to $\alpha^{qm}/h = -369.5(\pm 456.8)$ µHz. The uncertainty is given by the standard error of the weighted mean. Unfortunately its uncertainty $u(\alpha^{qm})$ dramatically increases by approx. an order of magnitude compared to the most recent value published in [53].

Neglecting the present conflict and evaluating the light shift in Sr3 based upon the value presented in [53] one can expect a fractional light shift near zero. But the uncertainty will be larger as before due to the current axial state population distribution. Since the atoms occupy higher axial states this is currently limiting the lattice light shift uncertainty (besides the mentioned inconsistency in α^{qm}). By reducing the higher axial

[13]Values have been published in [44, 51, 53, 55]. An overview is given in Fig. 5 in [53]

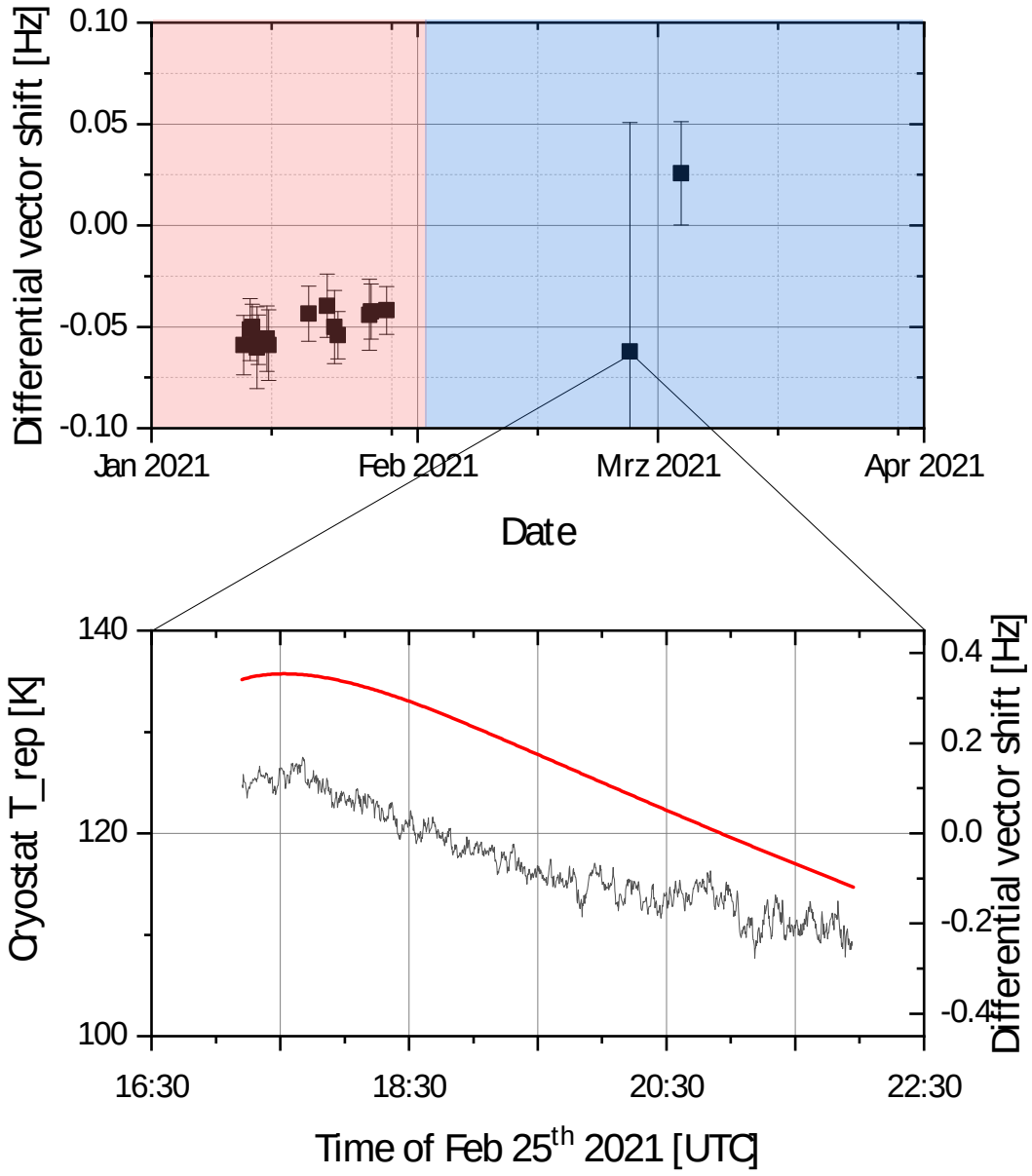

Figure 3.31.: Upper Fig.: Measured differential vector shifts $\delta\nu^{vec}$ during magic wavelength interleaved measurements for either room temperature (red shaded region) or cryogenic operation (blue shaded). The potential depth in the two cycles was altered between U_0 and U_0'. Lower Fig.: Throughout the measurement the temperature of the cryostats inner shield (red line) was radically changed by about $-25\,\mathrm{K}$. The differential vector shift between the two interleaved cycles of the magic wavelength measurement reveal a similar course. It changes by about $-350\,\mathrm{mHz}$ and even changes sign.

state population (e.g. by sideband cooling) controlling of the light shift uncertainty below the 10^{-18} level is possible.

3.5.7. Density shift

As described in Sec. 3.5.7 the density of atoms trapped in the optical lattice is subject to a frequency shift. To investigate the effect of density related frequency shift an interleaved measurement was performed with different number of atoms among the two cycles. During loading into the blue MOT the optical shutter blocking the Zeeman slower beam was closed after alternating duration. This effectively varies the loading time from the decelerated atomic beam into the blue MOT and thus the number of trapped atoms. Other systematic effects are equal in both cycles and therefore common mode rejected. Typically the difference in the number of atoms was about a factor of 2. The number of trapped atoms was related to the arbitrary unit counts that the experimental control program generates from the output voltage of the PMT. It has not been calibrated to the number of atoms yet but is linear proportional to it. With 400..600 counts in the low-atom-number cycle, the measurement was performed at a deep lattice potential of about 122 E_{rec} during spectroscopy thus maximizing the number of atoms and therefore the measurements lever arm. Similar to the lattice light shift measurement several density shift measurements have been performed and combined into one data set to reduce the uncertainty. Here a zero compatible frequency shift of $-4.5(65) \cdot 10^{-19}$ (few minus many counts) was found which corresponds to a fractional shift of $1.2(19) \cdot 10^{-21}$/count. The typical lattice depth during spectroscopy is about half the depth of that the density shift measurement was performed with. As an upper limit the values above are used where a higher atomic density is expected than in the shallow lattice that is commonly used for spectroscopy. For lattice configurations that provoke density shifts much more than in our experiment, zero compatible density shifts have been reported at lattice depth of more than $1000E_r$ [53] underlining the assumption state above as valid.

3.5.8. Other sources of frequency shifts

Frequency shifts on the clock transition can also arise due to effects such as line pulling, imperfect switching of the clock light due to non ideal switching characteristics of the clock

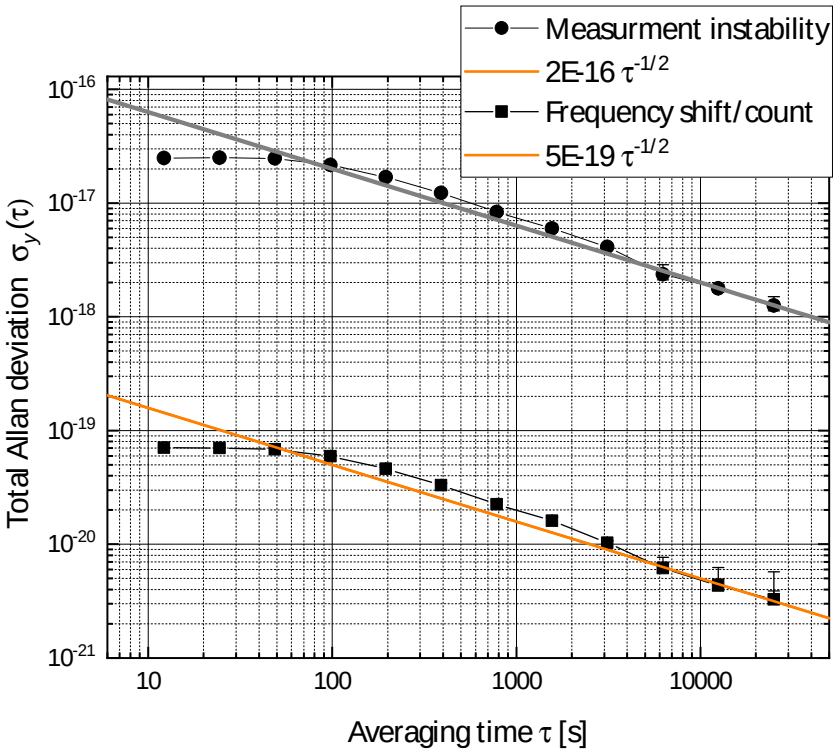

Figure 3.32.: Instability of the density shift measurement (black dots) and the frequency shift normalized to one count (black squares). The corresponding instabilities are $2 \cdot 10^{-16}/\sqrt{\tau}$ and $5 \cdot 10^{-19}/\sqrt{\tau}$. The density shift found is $-4.5(65) \cdot 10^{-19}$ from which the density shift coefficient is determined to be $1.2(19) \cdot 10^{-21}$/count.

AOM, lock error of the electronic servo or optical path length error. Typically these effects contribute to a negligible level to the total clock uncertainty and are therefore summed up as "other". For completeness these effects are discussed briefly in the following.

3.5.9. Line pulling effect

The line pulling effect arises from either unwanted excitation of neighboring Zeeman sublevels ($m_F = \pm 7/2$) or by $\sigma\pm$ transitions caused by imperfect polarization of the clock laser as discussed in 2.6.6. During spectroscopy the frequency splitting of the outermost $m_F = \pm 9/2$ Zeeman sublevels is approx. 560 Hz corresponding to a frequency separation[14] of approx. 62.2 Hz to neighboring m_F states. The typical line width of the clock transition used during spectroscopy is approx. 1.14 Hz which corresponds to a separation of the states of approx. 55 line widths. This is sufficient far detuned to no excite the neighboring $m_F = \pm 7/2$ states. Additionally we do not observe population of those states of more than 5% after spin polarizing the ensemble (Fig.3.33). The subsequent purification step (discussed in Sec. 2.5) reduces such parasitic population even further. From this we conclude a negligible frequency shift contribution from $m_F = \pm 7/2 - m'_F = \pm 7/2$ transitions due to population of neighboring Zeeman states.

Additionally coherent excitation via $\sigma\pm$-transitions can also cause a frequency shift. At the splitting of the magnetic sublevels given above the ${}^3\mathrm{P}_0, m_F = \pm 9/2 \; - \; {}^1\mathrm{S}_0, m'_F = \pm 7/2$-$\sigma^-$ transition is expected at a frequency detuning of ± 650 Hz. A frequency scan covering the possible $\sigma^\pm$ transitions of the outer stretched states does not show any significant population (Fig. 3.33) that may indicate a mentioned $\sigma\pm$-transition. Therefore the line pulling effect is attributed an uncertainty of 10^{-20} which makes its frequency shift contribution negligible.

3.5.10. Tunneling

In a horizontal optical lattice arrangement adjacent lattice sites are degenerate. This allows trapped atoms to tunnel between the lattice sites that causes a frequency shift [40]. In a pure horizontal lattice the frequency shift is at the order of the bandwidth.

[14] Neglecting the quadratic Zeeman effect

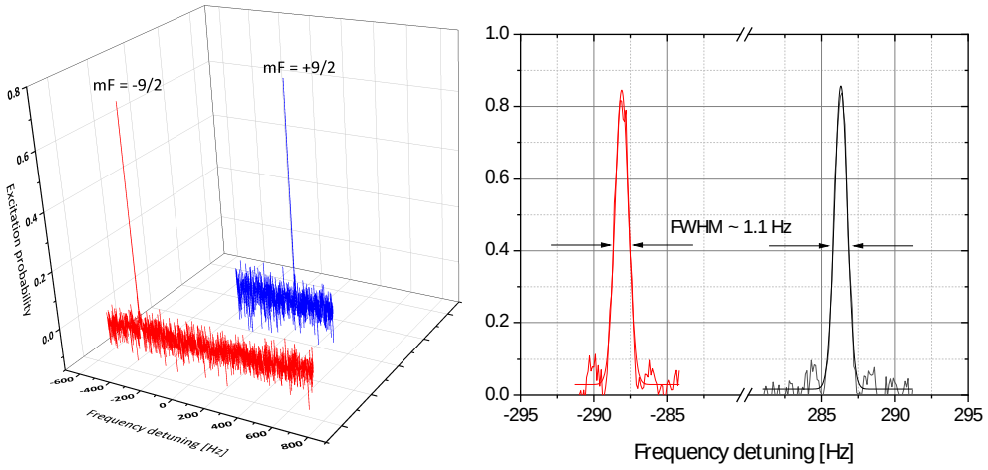

Figure 3.33.: Left: Frequency scans over the $m_F = \pm 9/2$ clock transition of a spin polarized ensemble. Neither excitation in a neighboring m_F sublevel are observed nor any σ transition ($m_F = 9/2 - m_F = 7/2$). This observation justifies a neglecting frequency shift contribution due to the line pulling effect. Right: Detailed plot of the observed lineshape for the $m_F = \pm 9/2$ stretched magnetic sublevels of the $^1S_0 - ^3P_0$ clock transitions. At a Rabi π-pulse probing duration of 700 ms, a Fourier limited linewidth of about 1.1 Hz was observed. Both plots were recorded with active pulse tube cooler to study the influence of its vibration on the spectroscopy signal. Still good excitation probabilities of more than 80% are observed.

For example in a pure horizontal lattice of depth $90E_r$ the tunneling frequency shift is about 5 mHz or $1 \cdot 10^{-17}$. To suppress intersite tunneling, adjacent lattice sites can be shifted in energy by a constant acceleration which can be Earth's gravity. In this way the atoms become strongly localized to a single lattice site which suppresses tunneling induced frequency shifts. For a vertical lattice used in Sr3 the frequency shift is zero since there simply is no tunneling possible at timescales of the probing duration.

Other frequency shifts

Frequency shifts due to technical imperfections such as the optical path length fluctuations and the clocks servo lock error must also be considered. They have already been discussed in Sec. 2.6.6 where the servo error uncertainty was updated with latest observed second order drift rates of the ultra stable silicon cavity. The optical path length error as well as the AOM efficiency uncertainty contribution due to imperfect switching behavior have been adapted from the uncertainty budget of Sr1. Since no major changes regarding those systems have been done, it is justified to adapt those values.

3.6. Preliminary uncertainty budget

All frequency shifts and uncertainties that are known either from measurements or from technical sources are listed in the clocks uncertainty budget in Tab. 3.4. The uncertainty budget of Sr3 is the result of the analysis of the investigated systematic frequency shifts presented in the previous sections. The frequency shift and total uncertainty, are given for two operational temperatures where operation at cryogenic temperatures leads to the lowest uncertainty possible at the moment. As we learned in Sec. 3.5.3 (Fig. 3.25 in particular) reducing the temperature of the cryostat below $-60\,^{\circ}\mathrm{C}$ does improve the BBR uncertainty further at the current stage of the experiment. To improve the BBR uncertainty further, the cryogenic beam shutter are necessary.

Apart from that the two largest contributions of uncertainty are stemming from the lattice and the BBR shift from the oven. The latter will drop out automatically when the cryogenic beam shutters are installed.

The lattice light shift uncertainty of about $2 \cdot 10^{-18}$ is stemming from the residual temperature of the atoms. As discussed in Sec. 3.5.6 the large uncertainty on the multi polar shift coefficient α^{qm} prevents uncertainties below about $1 \cdot 10^{-18}$ even with much colder atoms.

Compared to its predecessor Sr1, Sr3 offers a significant lower uncertainty. Due to the better temperature homogeneity the new apparatus allows the reduced BBR shift uncertainty was reduced significantly. The systematic uncertainty gets even lower when operating at cryogenic temperature. Installing the missing atomic beam shutters will reduce the corresponding uncertainty contribution to below $3 \cdot 10^{-19}$.

Effect	Fractional frequency shift / 10^{-18}	Uncertainty / 10^{-18}
Lattice light	-3.73	2.03
Tunneling	0.00	0.00
Probe light	-0.02	0.02
Second-order Zeeman	-187.2	0.44
Cold collisions	-0.37	0.61
dc Stark	-1.79	0.36
BBR, oven	-0.08	1.17
Other	0.00	0.2
Cryogenic operation		
Ambient	-31.30	0.21
Atom injection tube	-11.02	0.95
Windows	-0.09	0.09
Background gas collisions	-2.05	0.37
Room temperature operation		
Ambient	-4759.05	2.21
Atom injection tube	-0.13	0.30
Background gas collisions	-3.85	0.43
Total cryogenic operation	-239.5	2.73
Total room temperature operation	-4956.24	3.43

Table 3.4.: Preliminary uncertainty budget of Sr3 when operated at approx. 80 K or at room temperature. At either temperature Sr3 surpassed an uncertainty of $4 \cdot 10^{-18}$. At room temperature operation the uncertainty of Sr3 is limited by the contribution of the black body radiation shift closely followed by the contribution of the lattice light shift (details in text) that becomes the leading uncertainty contribution at cryogenic temperatures. Frequency shifts included in "Other" are line pulling effect, error of the electronic servo loop, optical path length error and the AOM efficiency.

4. Robust laser breadboards

Operating an optical clock based on atomic transitions requires several laser system for preparation and spectroscopy. For Sr-lattice clock Sr3 describe in this work, six lasers are required to address the relevant transitions. To enable long uninterrupted periods of operation all laser system must be reliable. Especially operation in the field e.g. in transportable [72, 92–94] or space born optical clocks [95, 96] the requirements on laser systems are more stringent compared to those operated in a well controlled environment such as a state-of-the-art laboratory. In the Sr1 clock a complex and fault-prone laser cooling system consisting of three separate diode lasers was operated for the red MOT [59]. A frequency stabilized ECDL master laser was injection-locked into a diode laser for power amplification at the $^1\mathrm{S}_0, F = 9/2 - {}^3\mathrm{P}_1, F' = 11/2$ cooling transition at 689 nm. A third ECDL was phase-locked to the master laser at an offset frequency of about 1.46 GHz to address the $^1\mathrm{S}_0, F = 9/2 - {}^3\mathrm{P}_1, F' = 9/2$ "stirring" frequency. About once per day this lock tended to fail. Additionally the setup required frequent realignment due to the long free space beam paths and the many optics that were required.

As a test bed for PTB's transportable optical clock, a new design based on commercially available laser systems and a fiber coupled EOM has been developed described in [34]. In the following the principle and benefits of the new setup will be discussed as well as the main results. In the new system the ECDL is operated at the $^1\mathrm{S}_0, F = 9/2 - {}^3\mathrm{P}_1, F' = 9/2$ "stirring" frequency and locked to the same reference cavity as the previous system. The $F' = 9/2 - F' = 11/2$ frequency difference is provided by a first order sideband generated in an EOM driven by a radio frequency input. One of the sidebands is addressing the $^1\mathrm{S}_0, F = 9/2 - {}^3\mathrm{P}_1, F' = 11/2$ cooling transition. This approach reduces the complexity dramatically compared to the previous system. The separate "stirring" laser and its fault-prone phase lock to the master laser are no longer required. After the fiber coupled EOM the light is amplified by a tapered amplifier system (TOPTICA

BoosTA) and feed into the custom made beam distribution board where the light for the red MOT and the spin polarization can be switched on demand. For spin polarization the atomic ensemble into either of the $m_F = \pm 9/2$ stretched magnetic substates. Also its footprint and weight is greatly lower than its predecessor. The previous optical free space setup required space of a few square meters. Now the footprint is reduced to below $1\,\mathrm{m}^2$ with the potential of being further miniaturized e.g. by using integrated optics. The weight reduction is predominantly achieved by less required laser drivers of the separate "stirring" laser. More details of the setup can be found in [34].

Characterization of the sidebands

The ratio of the carrier and sideband frequencies as a function of applied voltage on the EOM is related to the square of the Bessel functions of order n $[J_n(U)]^2$. In the previous system the ratio of optical power between the "stirring" and the cooling laser was 1:2. This corresponds to a modulation index of app. $\beta = 1.7$ considering the ratio of the amplitudes of the carrier and the first order sideband as can be seen in Fig. 4.1.

To characterize the sideband amplitudes as a function of RF drive power a scanning Fabry-Pérot with a free spectral range of 3 GHz was used. The sideband amplitudes are than measured with an oscilloscope. At a modulation frequency of 1.46 GHz the amplitudes of the carrier and the first four sidebands as a function of the EOMs drive RF power are measured and plotted in Fig. 4.1. An U_π of 4.8 V was found where U_π is the EOM's half-wave voltage at the given modulation frequency. This is slightly higher than the specification of 3.5 V. The deviation is attributed to the far off operating conditions compared to those of the specification provided by the manufacturer (center wavelength = 705 nm, modulation frequency = 1 kHz). The RF-power of the EOM is controlled by an amplified tabletop signal generator (Marconi 2024) that can produce any modulation index that is relevant for the experiment, without getting close to its damage threshold of app. $\beta = 13$. To characterize its ability to laser cool Sr the atoms are loaded into the optical lattice and their temperature estimated by performing sideband spectroscopy (Sec. 2.3). The system was first used and characterized in Sr1 that has a nearly horizontal lattice. The radial and axial temperatures was measured to be $T_{r,Sr1} \approx T_{z,Sr1} \approx 2\,\mu\mathrm{K}$ without "spilling" (Sec. 2.5) of the atoms that occupy higher axial vibrational states.

When operated in the vertical optical lattice of the new Sr3 system, a modulation

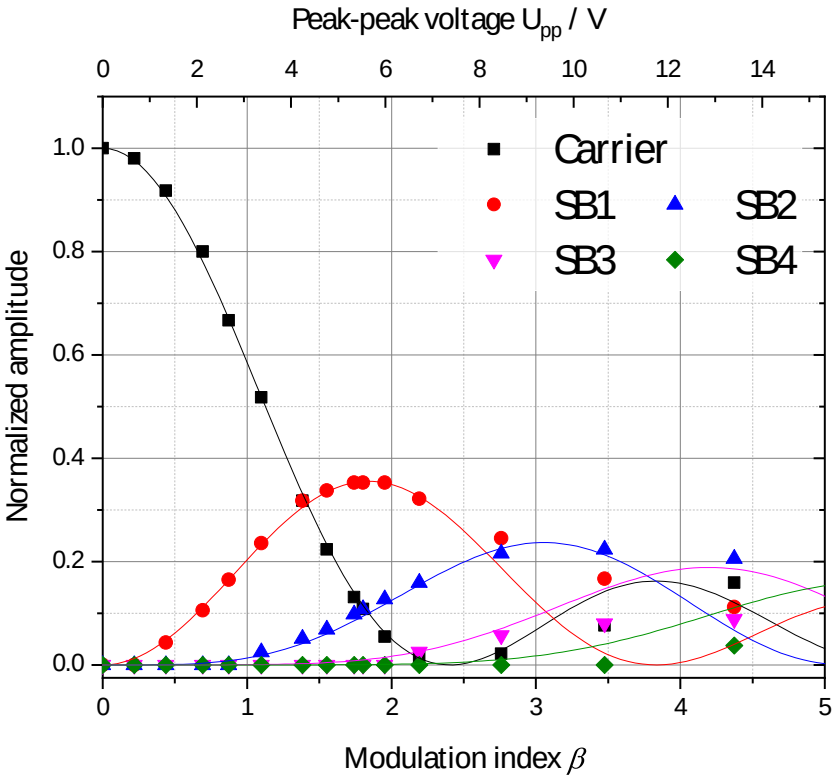

Figure 4.1.: Normalized single sided sideband amplitudes (colored) with respect to the carrier frequency (black) as a function of the modulation index β. Measured data are represented by dots and the solid lines represent the Bessel functions $J_0..J_4$. Graph taken from [34] with minor modifications.

index of app. $\beta = 1.4$ provided best results in terms of maximum number of trapped atoms. However, sideband spectroscopy revealed that the temperature of the atoms is higher compared to those mentioned above in Sr1. With a sideband spectroscopy measurement described in Sec. 2.3 and following the model developed in [39] the axial and radial temperatures measured in the shallow lattice in Sr3, have been found to be $T_{z,\mathrm{Sr3}} \approx 5.2\,\mathrm{mK}$ and $T_{r,\mathrm{Sr3}} \approx 8.7\,\mu\mathrm{K}$ under similar conditions. Only after using "spilling" to a potential depth of app. 22 E_{rec} the temperature of the atoms is sufficiently low and the lattice light shift uncertainty contribution gets minimal as discussed in Sec. 3.5.6.

After "spilling" the temperature of the atoms reduce to approx. $T'_{r,\mathrm{Sr3}} = 2.9\,\mu\mathrm{K}$ and $T'_{z,\mathrm{Sr3}} = 0.9\,\mu\mathrm{K}$. Overall the cooling performance in the axial direction after "spilling" is comparable to that in Sr1, where an axial temperature of ($T'_{z,\mathrm{Sr1}} \geq 1\,\mu\mathrm{K}$ was published in [62]. The "spilling" depth applied there was similar to that in Sr3. In contrast the radial temperature of the atoms is significantly higher in Sr3 compared to Sr1 ($T'_{r,\mathrm{Sr1}} \approx 2\,\mu\mathrm{K}$). The reason is not clear and has not been investigated in detail yet. It may be possible that the arrangement of the MOT beams in Sr3 compared to Sr1 is less efficient for cooling in the radial direction. Due to a fiber cluster used it is not possible to change the ratio in optical power among the three MOT beams. As a result there is an imbalance in power of approximately 1:1.5:3.7 during the red MOT phases along the a:b:c axis. Here the a-axis is pointing along the bias magnetic field, b and c are the diagonal MOT beams as seen in Fig. 3.1. That mismatch in optical power especially along the diagonal MOT beams may be the reason for the lower radial cooling efficiency of the atoms. To verify this theory the optical power ratio must be changed which has not been tested yet.

The two clocks (Sr1 first, and then implemented into Sr3) were operated with the new cooling system for several years now. No substantial degradation in optical power have been observed yet, despite operating the system continuously during several measurement campaigns that span over several weeks. Realignment of optical components is required only once in a blue moon. For our transportable optical clock the requirements on the laser system's weight and size are more stringent. Additionally its heat dissipation must be considered which is rather irrelevant for the lab-based system. The transportable optical clock has installed a similar laser cooling system that provided the described benefits. Although the predecessor system in the transportable clock was not as bulky as the lab-based system, the concept relying on three separate lasers was the same. The new laser cooling system still offers a reduction in size and mass that strongly matters for

the transportable clock Sr2. Additionally the separate but now needles “stirring” laser including its control electronics, set free valuable space and reduce the mass of the trailer.

5. Lattice induced photon scattering

As described in Sec. 2.7 the instability of a clock is one of its key performance factors, desired to be as low as possible. One of the strategies to improve a single clocks instability is to improve the clocks duty cycle by increasing the probing duration (by keeping the preparation time unchanged or decreased). Since the development of ultra stable lasers is ongoing and coherence times of up to several tens of seconds have been reported [17] an increase of probing duration to gain in clock instability is a logical consequence. However when atoms are trapped in the optical lattice, several loss mechanism can occur e.g. collisions with the background gas. Apart from that atoms prepared in the $^3\mathrm{P}_0$ excited state experience different scattering channels as the $^1\mathrm{S}_0$ ground state atoms. It can be observed as an additional decay rate where atoms emerge from $^3\mathrm{P}_0$ to the $^1\mathrm{S}_0$ ground state. The scattering process depends on the number of photons and therefore scales with the lattice potential depth. It is attributed to different types of off-resonant scattering induced by the intense optical lattice [97]. This chapter describes the photon scattering processes, the characterization measurements and discusses the consequences for clock operation.

5.1. Scattering processes

The scattering of photons can be separated into two different ones. Inelastic Rayleigh scattering [98] that leaves the internal electric atomic state unchanged and elastic Raman scattering that changes the atoms state. For Raman scattering, atoms in the $^3\mathrm{P}_0$ state will enter the $^3\mathrm{P}_J$ manifold predominantly via the intermediate $(5s6s)^3\mathrm{S}_1$ state due to lattice photon scattering. When they end in the long living $^3\mathrm{P}_2$ state they are shelved and lost for any kind of clock relevant operation. Atoms scattered into $^3\mathrm{P}_1$ state ($\tau = 21\,\mu\mathrm{s}$) will quickly decay into the ground state. In Fig. 5.1 the dominant scattering processes are

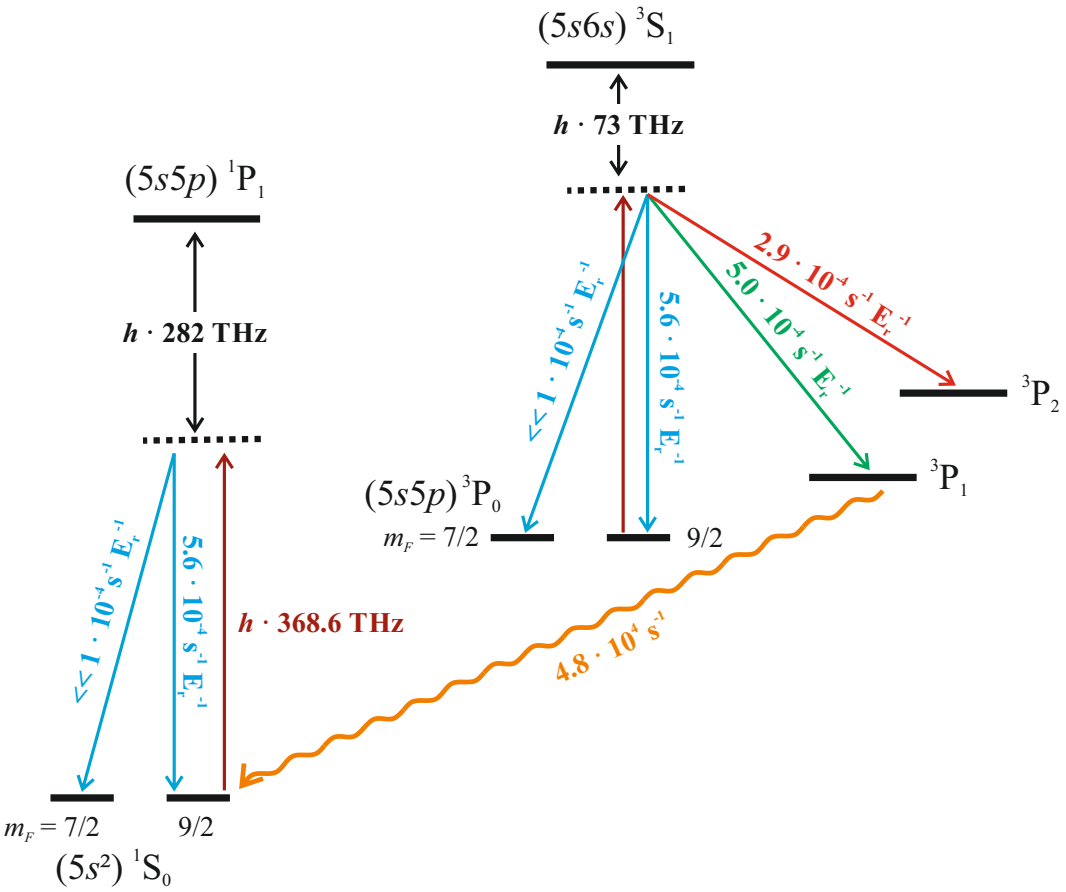

Figure 5.1.: Schematics of the photon scattering and branching ratios induced by the magic wavelength optical lattice near 368.6 THz in the $m_F = 9/2$ magnetic substate of ground- and excited state. The dominant scattering channels are depicted by colored arrows together with their decay rates normalized to the lattice potential depth in recoil energy E_r. The natural decay from $^3P_1$ to the $^1S_0$ ground state is shown in orange.

shown emerging from either the $^1S_0$ state or the $^3P_0$ state. Determining the off-resonant scattering rate $\Gamma_{i\to f}$ of an atom from its initial state i to a final state f for incoming linear polarized light is done by Kramers-Heisenberg formula leading to a relation that is proportional to the Einstein coefficient A_{ki}. A detailed theoretical treatment was done in our group and can be found in [97]. The population dynamics among the involved states of the hyperfine structure are described by a pair of coupled rate equations. In Fig. 5.2 the analytic solution of the rate equations (dashed and solid lines) fits well to the experimental data proving the theory to agree excellent with the experimental results.

5.2. Measurements of the decay rates

The measurement has been performed in Sr1 similar to a lifetime measurement described in Sec. 3.5.4 but with the atoms being prepared in the $^3P_0$ excited state. The atoms are cooled to a temperature of $T \approx 2\,\mu K$ by the two stage MOT (Sec. 2.1) and loaded into the optical lattice. To remove atoms from the trap that occupy axial vibrational states $n_z > 1$ "spilling" was used for 40 ms (Sec. 2.5). Subsequently the ensemble was spin polarized to enhance the population in the $m_F = 9/2$ stretched magnetic substate. Atoms in magnetic substates other than that are removed by the "clean-up" sequence (Sec. 2.5) that also puts the atoms in the desired $3P_0$ excited state. The sample is than kept for a variable hold time t_h of up to 25 s in the optical lattice. Such a series of measurements were performed at five different lattice depths. Subsequently the atoms state is read out by the detection sequence. For each hold time at the individual lattice depth, a sample size of app. 30 to 40 measurements was collected. From that the average number of ground- (N_g) and excited state atoms (N_e) is determined. To account for long term atom number fluctuation throughout the measurement the population was normalized to the average count number found in the measurement series at $t_h = 1\,s$. This reference measurement was performed before and after each series of measurement. It is to be mentioned that the state detection cannot resolve magnetic substates or hyperfine levels of a certain ^3P_J state nor distinguish between atoms in the states $^3P_0$ and $^3P_2$ due to the repumping process. Thus Rayleigh and Raman scattering into the $^3P_2$ state cannot be investigated experimentally and are treated theoretically. To compare the results to the observed $^3P_0 - {}^1S_0$ decay an additional measurement where the atoms are prepared in the $^1S_0$ ground state has been performed as reference. The experimental results are shown in Fig. 5.2. Comparing the decay rates reveals a clear decay $^3P_0 - {}^1S_0$ that increases for deeper lattice potentials.

From the measurement a decay rate of

$$\gamma_L = 556(15) \cdot 10^{-6} s^{-1} E_r^{-1}$$

due to off resonant inelastic scattering of the lattice laser is inferred. The loss rate due to other sources such as spontaneous decay was found to be

$$\Gamma_0 = 5.2(12) \cdot 10^{-3} s^{-1}$$

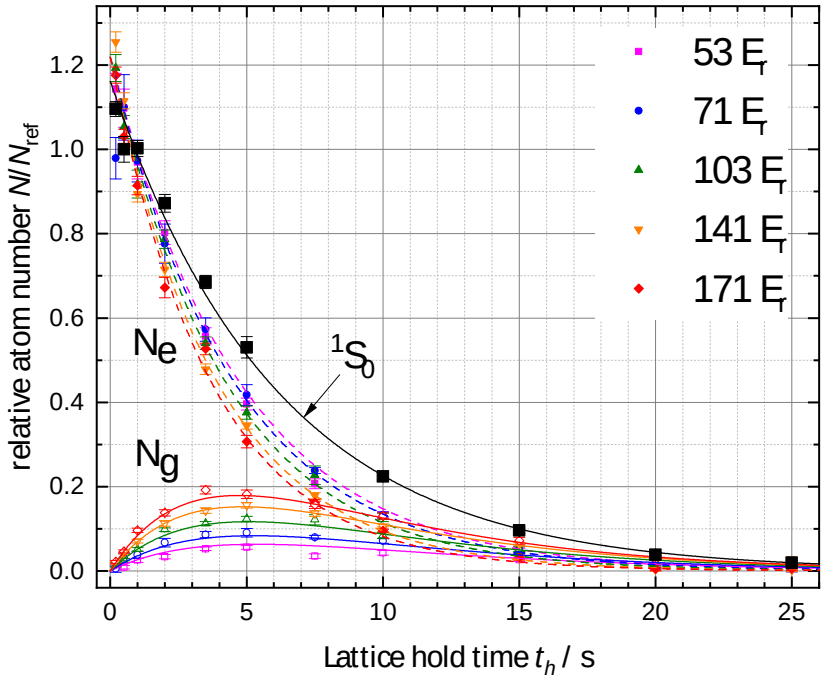

Figure 5.2.: Measured population dynamics of atoms initially prepared in the $^3P_{0,2}$ state as a function of holding time t_h (colored data). For reference the decay rate for atoms prepared in the ground state (black points) is show and clearly revealing a potential depth depending loss of excited state atoms. The lines are fits originate from the rate equations from [97].

5.3. Effects on lattice clocks

The described off-resonant scattering processes of the magic wavelength optical lattice is affecting clock operation in several ways. The good news first: Systematic frequency shifts from either Ramsey- or Raman scattering are expected to occur. Rayleigh scattering appears not to change the electronic state of the atom. But it is in discussion weather it influences the coherence of the atomic superposition state. As discussed in [99, 100] inelastic scattering dampens the coherence if the scattering amplitudes of the involved states differ. The scattering amplitudes are proportional to the differential dynamic polarizability. For a magic wavelength lattice this difference is zero by definition. Therefore, Rayleigh scattering in our experiment will not degrade atomic coherence on a relevant scale.

The two Raman scattering processes are more subtle. They result in decoherence of the atomic superposition state and depopulation of the $^3P_0$ excited state. This degrades the fringe contrast in Ramsey spectroscopy and results in a degraded clock stability. In a Rabi spectroscopy experiment the transition lineshape is broadened but remains symmetric effectively causing no frequency shift. Additionally atoms that have been scattered into either $^1S_0$ or $^3P_2$ are still being detected resulting in a noise contribution of the detected population. Avoiding this for the $^3P_2$ state requires a different repumping process that allows to distinguish between atoms in in $^3P_0$ and $^3P_2$ e.g. by selective repumping on the $^3P_0 - {}^3D_1$ transition as demonstrated in ytterbium lattice clocks [101, 102].

The growth of population in the $^1S_0$ state induced by the photon scattering process, is highly sensitive to clock laser radiation since it is in resonance. As calculations in [97] show, atoms predominantly return to the $m_F = \pm 9/2$ state with similar consequences as discussed above. The result is degraded clock stability due to loss of fringe contrast (Ramsey spectroscopy) or the lineshape is modified but remaining symmetric (Rabi spectroscopy) and not causing a systematic frequency shift. Considering the branching ratios of all possible transitions, the atoms can decay to the $^1S_0$ ground state into the $m_F = \pm 7/2$ and $m_F = \pm 5/2$ Zeeman magnetic sublevel. As discussed in Sec. 3.5.8 population in Zeeman sublevels other than $m_F = \pm 9/2$ gives rise to the line pulling effect. But due to symmetry reasons it only affects the frequency splitting of the Zeeman substates and not the transitions center frequency.

5.4. First direct lifetime measurement of the $^3P_0$ state

From the data obtained from the measurements, the lattice intensity independent loss rate Γ_0 has been determined. It includes spontaneous decay of the $^3P_0 - {}^1S_0$ clock transition from which the lifetime of the $^3P_0$ state can be calculated. The dominant contribution in Γ_0 is from optical pumping on the $^3P_0 - {}^3D_1$ transition due to blackbody radiation. The pumped atoms end up in the $^3P_1$ state and spontaneously decay to the ground state. By estimating the BBR-induced quenching rate [103] and the branching ratio of the spontaneous decay of the $^3D_1 - {}^3P_J$ transitions one can express Γ_0 as the sum of a BBR induced loss rate and spontaneous decay from the upper clock state. One

finds a spontaneous decay rate of $\Gamma_s = 3.0\,(13) \cdot 10^{-3}\mathrm{s}^{-1}$ corresponding to a lifetime of $\tau(^3P_0) = 330\,(140)$s. This result is within marginal agreement of 2σ with the values published in [25, 44]. Nevertheless is represents the first ever published experimental determination of the $^3P_0$ state lifetime.

6. Absolute frequency measurement

In 2019 several units of the International System of Units (SI) have been revised and are now based upon fundamental constants. However this was not the case for the most precisely measurable unit the Second. It was last defined in 1967 by the Bureau International des Poids et Mesures (BIPM) as 9 192 631 770 periods of the radiation corresponding to the transition between the two hyperfine levels of the unperturbed ground state of the ^{133}Cs atom[1]. Modern optical clocks either based on optical lattice clocks or single ion clocks have surpassed the systematic uncertainty of the fountain clocks by orders of magnitude that raises the discussions on a redefinition of the Second for which the BIPM released several requirements[2]. One is the determination of the clocks frequency with a fractional uncertainty of below $3 \cdot 10^{-16}$ by comparing its frequency to a Cs primary standard. In this chapter I will present the results of the absolute frequency of ^{87}Sr $(5s^2)^1\mathrm{S}_0 \rightarrow (5s5p)^3\mathrm{P}_0$ transition in Sr1 and the new cryogenic clock Sr3. The measurements with Sr1 were performed from 2017 to 2019 against PTB's primary frequency standards, the cesium fountain clocks CSF1 and CSF2. The measured frequency yield in a new record with respect to the uncertainty of the average frequency of $1.5 \cdot 10^{-16}$ and have been published in [8].

Frequency standards

The frequency standards involved, are PTB's primary frequency standards, the cesium fountain clocks CSF1 and CSF2 where the absolute frequency of Sr1 and Sr3 has been determined with.

The CSF1/2 clocks are contributing data regularly to steer the International atomic Time (TAI). Therefore their specific mode of operation is denoted "primary frequency standard" (PFS) that allows the highest clock accuracy of about $u_{sys,\mathrm{CSF1/2}} = 1.3 -$

[1] www.BIPM.org

[2] (https://www.bipm.org/utils/en/img/CCTF-roadmap.jpg)

$2.3 \cdot 10^{-16}$. The instability of the fountain clocks is about three orders of magnitude worse compared to state of the art lattice clocks. Their individual instability is $\sigma_{y,\mathrm{CSF1}} = 3.3 \cdot 10^{-13}/\sqrt{\tau}$ and $\sigma_{y,\mathrm{CSF2}} = 1.6 \cdot 10^{-13}/\sqrt{\tau}$. A detailed description of the Cs clocks was published in [13].

The Sr1 clock was described in many previous publications [9, 59, 62, 70]. Since the latest evaluation in [9] it now features a more stringent evaluation on the BBR shift resulting from the strontium oven with a fractional frequency uncertainty of about $1.5 \cdot 10^{-17}$ as described in [8]. Also the protocol for the determination of the lattice induced frequency shift, now follows the "operational magic wavelenght" [53] protocol described in Sec. 2.6.3 for Sr1 and Sr3.

The strontium clocks feature in principle two mode of operation. The already described interleaved measurement for self evaluation and the single cycle single-cycle operation where the measurement cycle repeats after four interrogations. Sr1 was operated most of the time mostly for self-evaluation then in single-cycle operation since it was not primarily intended to gather data for absolute frequency measurement.

In single-cycle operation, the systematic uncertainty of Sr1 is slightly higher than it is during interleaved measurements. Due to a second of waiting time after each clock interrogation, the time average thermal load on the MOT coils and therefore their temperature is lower compared to an interleave measurement where no waiting time is included. This reduces the BBR shift uncertainty in single cycle operation. In self-evaluation operation this is not a problem since it is common mode in both cycles of the interleaved measurement. But for frequency comparisons the higher thermal load on the coils degrades the uncertainty by about $1 \cdot 10^{-17}$. The systematic uncertainty of Sr1 was not exceeding $u_{sys} = 3 \cdot 10^{-17}$ [8] for any of the individual measurements.

The instability of Sr1 and Sr3 is described in Sec. 3.3. The lock of the clock laser to an ultra stable crystalline Si cavity operated at cryogenic temperature [17] greatly improved the clock instability. Taken into account the introduced dead time of 1 s the clock instability is slightly degraded to about $2 \cdot 10^{-16}/\sqrt{\tau}$.

Measurement time intervals

For the CSF1/2 clocks only such uptimes have been considered when they were operating in PFS-mode to ensure the highest available accuracy. Measurement data from Sr1 was

obtained mainly from measurement campaigns or from various self evaluation measurements. From the latter the measurement duration is typically at the order of a few hours, sometimes a day and include gaps where the clock was not locked to the atoms. With respect to the instability of CSF1/2, the statistical uncertainty of such measurements would not be sufficient. To bridge down times of the Sr clock the technique described in [9] was applied where a Hydrogen Maser (H-maser) was used as a flywheel oscillator. Compared to the Cs clocks, H-masers have are lower frequency instability on timescales of below 10^5s. They are highly reliable and continuously operated. By using the flywheel oscillator technique the up-time of the Sr clock enlarges from 59 days to about 120 days but restrict the bridgeable gaps in downtime to be smaller than 1 day.

Evaluation

To compare the Sr clocks against either CSF1/2 microwave clocks, the optical frequency of the Sr clocklaser is converted into the radio frequency domain via a frequency comb. Preferably the signal is transported among the buildings in the optical domain via phase stabilized optical fibers rather than cable guided radio frequency signal where noise cancellation is not possible. Active fiber noise cancellation [64] eliminates environmental noise such as vibrations or acoustic noise acting on the optical fiber and allows to deliver phase stable light. Therefore the optical to radio frequency conversion was preferred to be performed as close as possible to the fountain clocks.

To benefit from the Maser as a flywheel oscillator a noise model was created based on a long measurement of the Sr1 clock against the respective H-maser as a reference. At PTB several Maser (VREMYA-CH VCH-1003M) are continuously providing the radio frequency reference. It offers a stability better than those of the Cs fountain clocks on timescales of up to 10^5s. This allows to bridge downtimes in the optical lattice clocks availability of up to 1 day. The Masers noise model obtained from long term measurements take into account its white frequency noise, white phase noise and flicker floor noise contribution that is converted into the corresponding spectral power densities relying on Parseval´s theorem. From weighting functions $g_i(t)$ that represent the uptimes of the individual clock, an uncertainty related to the extrapolation u_{ext} can be described as in [9]. This approach is insensitive to the masers linear drift, but only if the centers of gravity of both weighting functions coincide. For some of the measurements in [8] the center of gravity deviates by a few hours, but due to the small maser drift of $1.1 \cdot 10^{-16}$/day, this contribution is negligible.

Measurement results with Sr1

Form the measurement data an absolute frequency of Sr1 can be determined against against the individual Cs fountain clock. The statistical uncertainty of Sr1 and the individual fountain clock are treated as uncorrelated as well as the extrapolation uncertainty u_{ext}. One finds weighted average frequency values of $\nu_{\mathrm{Sr1,CSF1}} = 429\,228\,004\,229\,872.92(11)$ Hz and $\nu_{\mathrm{Sr1,CSF2}} = 429\,228\,004\,229\,873.05(8)$ Hz with respect to CSF1/2. This results in a weighted mean absolute frequency of $\nu_{\mathrm{Sr1}} = 429\,228\,004\,229\,873.00(7)$ Hz. Here the systematic uncertainty of the individual fountains was treated uncorrelated. For time windows where both fountains have been operated, u_{ext} introduces a correlation between the systematic uncertainties of the fountains. This contribution is small enough to be neglected.

Further use of the dataset can be made to test the validity of the Einstein equivalence principle (EEP). A violation of it could manifest itself as a drift or modulation of the Sr/Cs frequency ratio which can be caused by e.g. a temporal variation of fundamental constants such as the proton-electron mass ratio μ or their coupling to a gravitational potential such as the Sun's.

A potential violation of the EEP was investigated by analyzing the dataset for periodic variations of the Sr/Cs frequency ratio with a periodicity of the anomalistic year. The findings are compatible with zero thus no violation of the EEP was found [8]. This is in agreement with the results of [104,105]. Furthermore a more stringent coupling parameter for the coupling of the Sr/Cs frequency ratio to the proton-electron mass ratio of $k_\mu = 35(590) \cdot 10^{-9}$ was found. In the consequence a temporal variation $\dot{\mu}/\mu = -6.9(6.5) \cdot 10^{-17}$ was found. This value is in agreement with the one published in [106]. Further details can be found in [8].

Absolute frequency measurement of Sr3

The absolute frequency of Sr3 has also been measured in the same way as described above. During characterization of the clock several interleaved measurements were performed with a frequency shift in the 10^{-18} range among the two clock cycles such as magic wavelength measurements or density shift measurements. In Fig. **??** the result of the absolute frequency of Sr3 is shown. Considering the systematic uncertainty of the fountain clocks as uncorrelated a weighted average frequency of $\nu_{\mathrm{Sr3}} =$

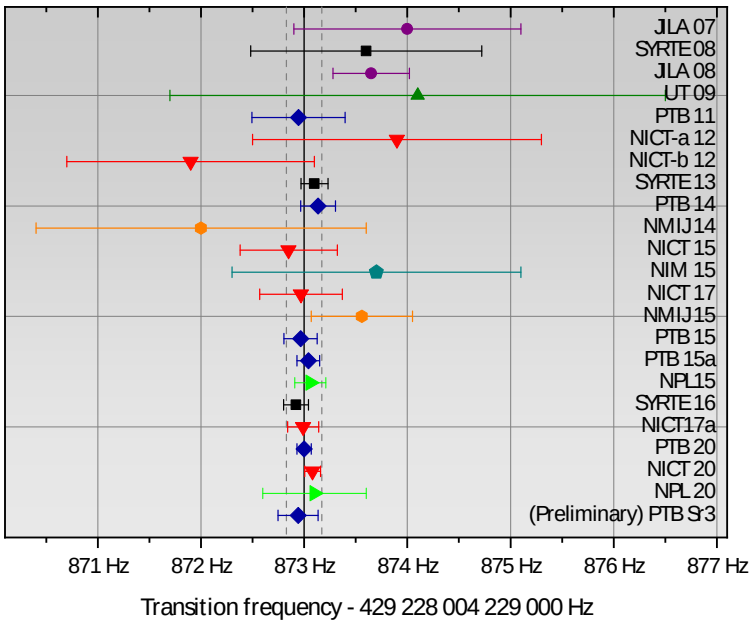

Figure 6.1.: Overview of reported absolute frequency of the ^{87}Sr $^{1}S_0 - {}^{3}P_0$ clock transition frequency from several research institutes since the first recommendation of the CIPM in 2006. The vertical black line indicates the current recommendation of ...873.0(2)Hz with the uncertainty as dashed vertical lines. The reported absolute frequencies are from: JILA 07 [107], SYRTE 08 [108], JILA 08 [109], UT 09 [110], PTB 11 [59], NICT-a 12 [111], NICT-b 12 [112], SYRTE 13 [54], PTB 14 [62], NMIJ 14 [113], NICT 15 [114], NIM 15 [115], NICT 17 [116], NMIJ 15 [117], PTB 15 [9], PTB 15 a [9], SYRTE 16 [118], NPL 15 [61], NICT 17a [119], PTB 20 [8], NICT 20 [120], NPL 20 [121].

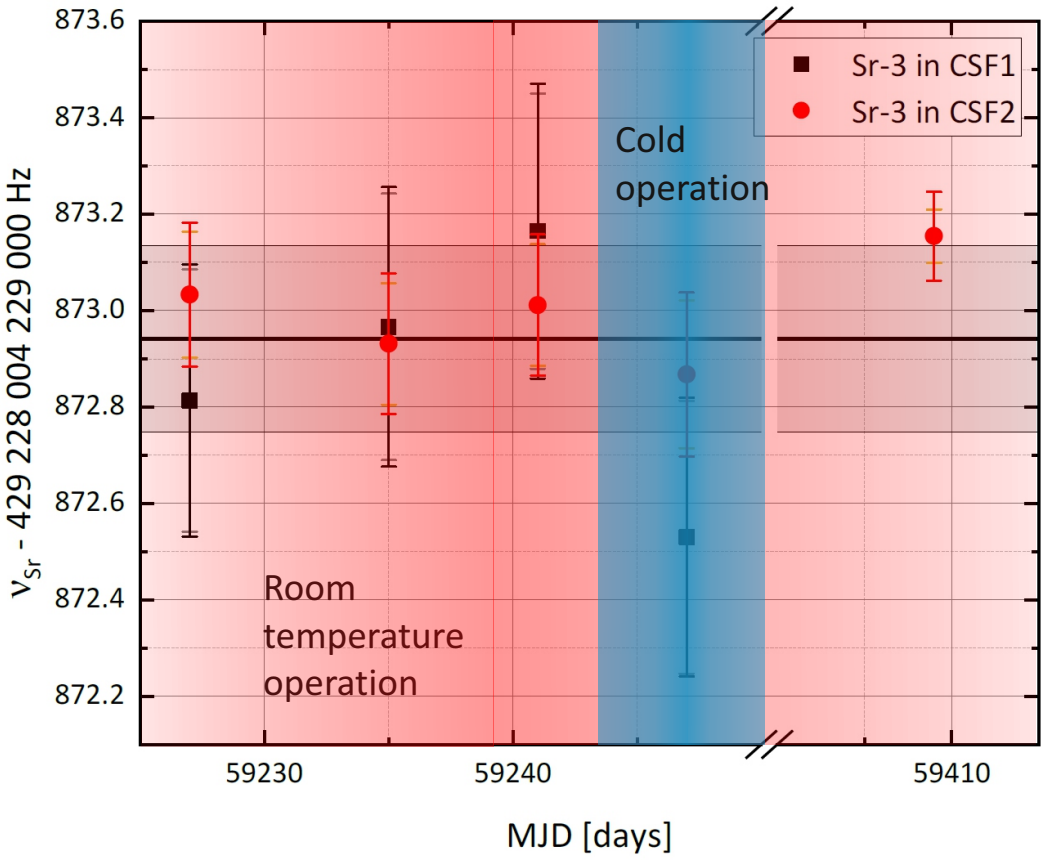

Figure 6.2.: Measurement of the absolute frequency of Sr3 with PTBs CSF1/2 microwave clocks. The average of the measured frequencies of 429 228 004 229 872.94(19) Hz is within the recommendation of the BIPM for ^{87}Sr and in agreement with the measured frequency of Sr1.

429 288 004 229 872.94(19) Hz is obtained. The result can be seen in comparison to other published values in Fig. 6.1. It is in agreement with recent absolute frequency measured with Sr1 (PTB 20 in Fig. 6.1), the current recommendation by the BIPM and many others published by other research institutes. The measurement labeled "cold operation" was supposed to take part during cooldown from room temperature to app. 80 K. Unfortunately the number of atoms decreased rapidly during cooldown for an unknown reason. A final temperature of −16 °C was reached before clock operation failed.

Further analysis e.g. to validate the EEP have not been performed yet since the dataset is quite short and does not even cover a full period of the anomalistic year.

7. Frequency ratio of PTB's ^{87}Sr lattice clock and ^{171}Yb^{+} single-ion clock

As seen in the previous chapter, the knowledge in the absolute frequency of the strontium optical lattice clock is typically limited by the accuracy of today's primary frequency standards realized by ^{133}Cs fountain clocks. State of the art optical atomic clocks have outperformed the cesium fountain clocks by two orders of magnitude in accuracy and instability which is why the International Committee for Weights and Measures (BIPM) have announced several atomic transitions [122] as Secondary Representations of the Second (SRS) [123]. The most accurate absolute frequency of an optical frequency standard reported to date is of the $^2S_{1/2}-^2F_{7/2}$ electric octupole (E3) transition in ^{171}Ytterbium$^+$ [124] with a fractional uncertainty of $1.3 \cdot 10^{-16}$. Compared to the determination of the absolute frequency of the $^1S_0 - {}^3P_0$ transition in neutral ^{87}Sr of $1.5 \cdot 10^{-16}$ described in Sec. 6, the measurement uncertainty is slightly larger but comparable. Both clocks share the problem of being limited in achieving lower measurement uncertainties of their absolute frequencies by the ^{133}Cs clocks. For instance the systematic uncertainty of Sr1 from self evaluation is reported an order of magnitude lower ($1.5 \cdot 10^{-17}$ [8]). Similar holds true for the Yb$^+$ clock of a reported systematic uncertainty of $2.7 \cdot 10^{-18}$ [10]. However direct comparisons of optical transition frequencies is free of such a limitation since the determination of a frequency ratio ν_a/ν_b is a universal dimensionless quantity and the accuracy of the Cs clocks drops out.

Within the BIPMs road map towards a redefinition of the second based on an optical transition, the measurement of at least 5 optical frequency standards is requested. Each ratio measurement is at least twice to be performed by independent labs and must be in agreement within $\Delta\nu/\nu < 5 \cdot 10^{-18}$. Additionally direct comparison of optical clocks is a useful tool in fundamental research when it comes to applications such as chronometric

leveling [125, 126], the search for dark matter [71] or the search for variations of fundamental constants [5, 127]. The frequency ratios determined by different institutes can be compared to evaluate local clock performance. Moreover pairwise ratios between three or more clocks allow reproducibility tests for laboratories that have access to only one pair of clocks. In this chapter the results of a series of frequency ratio measurement between PTB's ^{171}Yb$^+$ single-ion clock and the Sr-lattice clock Sr1 as well as first measurements performed with Sr3 is presented.

Setup

The setup used for the evaluation of the frequency ratios of the individual Sr clock (Sr1 or Sr3) and the Yb$^+$ clock is well described in [10]. Here only a brief summary is given. The three clocks are operated separately in two different buildings on the PTB compound. To compare their transition frequencies, two optical frequency combs (each in every building) are used. On every individual comb an rf-beat signal is generated by the corresponding local oscillator of 194 THz (Sr clock location) and 344 THz (Yb$^+$ clock location). To enable a phase coherent link among the combs, a transfer laser at 194 THz is send from the Sr-comb to the Yb$^+$ comb. A second transfer in opposite direction is used to evaluate the link performance. All optical fiber paths that are relevant for the determination of the frequency ratio are actively stabilized. All frequencies relevant for the evaluation of the ratio $\rho = \nu_{\mathrm{Yb}^+}/\nu_{\mathrm{Sr}}$ are counted by dead time free counters. The frequency ratio is determined by analyzing the rf-beat signals created at the individual combs with respect to the transfer link lasers frequency.

For a detailed description of the Yb$^+$ and Sr1 clock the reader may refer to [10]. The description of Sr3 is found in this manuscript.

The gravitational redshift between the clocks was determined in a series of leveling measurements and corrected for Sr1 and Yb$^+$. The redshift correction for Sr3 was based upon a measured height difference to Sr1 which is assumed to be accurate to the 1 cm level or $1 \cdot 10^{-17}/\rho$ in fractional units.

Frequency ratio, Sr1

Yb$^+$/Sr1 frequency ratio measurements range from 2013 to 2019. Each measurement is attributed an uncertainty u_{ratio}

$$u_{\mathrm{ratio}} = \sqrt{(u^2_{\mathrm{sys,Sr}} + u^2_{\mathrm{sys,Yb^+}})\rho^2 + u^2_{\mathrm{stat}}} \tag{7.1}$$

consisting of the systematic clock uncertainties $u_{\mathrm{sys},(\mathrm{Sr},\mathrm{Yb}^+)}$, the statistical uncertainty u_{stat} and the frequency ratio $\rho = \nu(\mathrm{Yb}^+)/\nu(\mathrm{Sr}) \approx 1.495991619$. The short therm scatter of the ratio measurements was typically at the order of a few 10^{-17}. But on longer timescales of about half a year, variations in the frequency ratio at the order of about $1 \cdot 10{-}16$ have been observed which are beyond any of the clocks claimed 1-σ systematic uncertainty. The reason remained unclear although detailed investigations on all the frequency sensitive and relevant components have been performed (optical clocks, fiber links, frequency combs). The origin of the discrepancy is either due to an error in the evaluation of at least one systematic frequency shift or resulting from a yet unknown systematic effect. From the computed Allan deviations of the individual ratio measurements, no significant deviation from white frequency noise is observed[15]. In contrast for the full dataset long-term scatter is larger than expected from the uncertainties of the individual measurements. For a data set where the results are normally distribution one would expect to find a reduced chi-square of χ^2_{red} of 1. However for the whole dataset of the ratio measurements one finds a reduced chi-square $\chi^2_{\mathrm{red}} = 1.9$ with respect to the total uncertainties. This indicates that the long therm scatter observed in the dataset is beyond uncertainties of the individual measurements

To attribute for the variations in the frequency ratio, a constant "dark-uncertainty" u_{d} is introduced. To meet the requirement of a reduced chi-square of $\chi^2_{\mathrm{red}} = 1$ for the entire data set one finds a "dark-uncertainty" of $u_{\mathrm{d},\mathrm{Yb}^+,\mathrm{Sr1}} = 18 \cdot 10^{-18} \cdot \rho$.

In the process a weighted mean frequency ratio of ${}^{171}\nu_{\mathrm{Yb}^+}/{}^{87}\nu_{\mathrm{Sr1}} = 1.495\,991\,618\,544\,900\,537(38)$ from the whole dataset has been determined. This is one of the lowest reported uncertainties reported so for the comparison of different clock species. Compared to other reported non inter-species frequency ratios reported in [4, 96, 128–132] only the one in [132] has a lower uncertainty.

Frequency ratio, Sr3

As Sr3 started measurement operation, frequency ratio measurements against the Yb^+ clock were performed in the same way as described with Sr1. The total uncertainty of the frequency ratio measurements undoubtedly benefits from the lower systematic uncertainty of Sr3 (Tab. 3.4). For example consider a measurement with a statistical uncertainty of $u_{\mathrm{stat}} = 10 \cdot 10^{-18}$, $u_{\mathrm{sys,Sr1}} = 15 \cdot 10^{-18}$ and $u_{\mathrm{sys},\mathrm{Yb}^+} = 3.2 \cdot 10^{-18}$ result in a total measure-

[15] Beyond the servo attack time

ment uncertainty of $u_{\mathrm{ratio,Yb^+/Sr1}} = 25 \cdot 10^{-18}$ (Eq. 7.1). By exchanging the systematic uncertainty of Sr1 by that of Sr3 of $u_{\mathrm{sys,Sr1}} = 3.5 \cdot 10^{-18}$ the uncertainty in the ratio reduces by more than a factor of two to $u_{\mathrm{ratio,Yb^+/Sr3}} = 12 \cdot 10^{-18}$ for the same statistical uncertainty of the dataset.

In 2021, ratio measurement data was collected spanning for about half a year. The individual results of the frequency ratio measurements can be seen in Fig. 7.1. The measurements at MJD 59270 was performed with Sr3 operated at cryogenic temperature, all others at room temperature. Sr3 was operated mostly in self evaluation mode running MWL measurements mostly to uncover potential variations in the lattice lightshift. Only the last measurement was performed in single cycle operation. For Sr3 the two different modes of operation do not affect the systematic uncertainty compared to Sr1 where the effect was significant. As seen in Fig. **??** the Yb$^+$/Sr3 ratios are significantly higher compared to those obtained from the Sr1/Yb$^+$ frequency ratio and are not in agreement within the 1-σ uncertainty. The reason is yet unclear. Following the same evaluation method as for the Yb$^+$/Sr1 ratio yields in a frequency ratio of $^{171}\nu_{\mathrm{Yb^+}}/^{87}\nu_{\mathrm{Sr3}} = 1.495\,991\,618\,544\,900\,658(22)$ including a "dark uncertainty" of $u_{\mathrm{d,Yb^+,Sr3}} = 13 \cdot 10^{-18} \cdot \rho$. However the original dataset without the "dark uncertainty" is not statistically well behaved which is indicated by a reduced chi-square of $\chi^2_{\mathrm{red}} = 4$. When restricting the reduced chi-square to $\chi^2_{\mathrm{red}} = 1$ and allowing a contribution from the "dark uncertainty" in the same way as for the evaluation of the dataset obtained with Sr1, one finds the value reported above which is about $5 \cdot 10^{-18} \cdot \rho$ lower than $u_{\mathrm{d,Yb^+,Sr1}} \cdot \rho$.

The measurements at MJD 59408 and 59411 (cycles in Fig.7.1) have been performed with significantly hotter atoms ($T'_z = 5\,\mu\mathrm{K}$ instead of about $T_z = 1\,\mu\mathrm{K}$ in the optical lattice). From the higher temperature a frequency shift of about $+3 \cdot 10^{-18}$ is expected. After correcting for the higher atomic temperature using the evaluation method describe in this manuscript, the measured frequency ratio is in good agreement with the others.

Conclusion

The presented average Yb$^+$/Sr3 frequency ratio is in clear disagreement to those measurements performed with Sr1. The difference in the average $^{171}\nu_{\mathrm{Yb^+}}/^{87}\nu_{\mathrm{Sr}}$ ratios is about $\delta\rho = \frac{^{171}\nu_{\mathrm{Yb^+}}}{^{87}\nu_{\mathrm{Sr1}}} - \frac{^{171}\nu_{\mathrm{Yb^+}}}{^{87}\nu_{\mathrm{Sr3}}} = 12 \cdot 10^{-17}$ which is not covered by the combined systematic uncertainty of the involved clocks.

Hypothetically, considering the output frequency of the $^{171}\nu_{\mathrm{Yb}^+}$ single ion clock as constant and stable over all times for reference, the discrepancy in the average frequency ratios would then exclusively be caused from a frequency difference between Sr1 and Sr3. The different frequency ratios translates to a difference in the frequency of the Sr clocks to $\Delta\nu_{\mathrm{Sr1-Sr3}} = \nu_{\mathrm{Sr1}} - \nu_{\mathrm{Sr3}} = \delta\rho/\rho = 8 \cdot 10^{-17}$. This is far beyond the systematic uncertainty of any of the two Sr clocks. In fact this is more than a factor of 5 larger than the systematic uncertainty of Sr1 ($1.5 \cdot 10^{-17}$) and more than an order of magnitude apart from that of Sr3. Still the cause of such a large frequency shift is unknown. From the measurements of the absolute frequency presented in the previous chapter (Cha. 6) the average frequency difference between Sr1 and Sr3 can be calculated. The average frequencies found for the two clocks differ by about 60 mHz or $\Delta\nu_{\mathrm{Sr1-Sr3}} = 1.4(7) \cdot 10^{-16}$ which covers the deviation seen in the different frequency ratios against the Yb^+ clock. But the measurement of the absolute frequencies is not accurate enough. Furthermore the absolute frequencies of Sr1 and Sr3 are in agreement within the measurement uncertainty. Concluding that Sr1 and Sr3 produce different output frequencies after correcting for the known systematic frequency shifts, can only be seen as an indication not as a proof. The "dark uncertainty" of $u_{\mathrm{d,Yb}^+,\mathrm{Sr3}} = 13 \cdot 10^{-18} \cdot \rho$ found in the Yb^+/Sr3 ratio, is also larger than any of the clocks systematic uncertainty. This indicates that a similar long-term effect as in the Yb^+/Sr1 ratio measurements occur. As Sr3 is based uppon an entirely new vacuum system and but still a "dark uncertainty" is present, one can argue to exclude the Sr3 vacuum system as a potential source of it. We have not found a distinct source for the different frequency ratios in the involved systems. No uncorrected frequency shift was found. This underlines even more the necessity of regular frequency comparison measurements of optical clocks over longer periods of time.

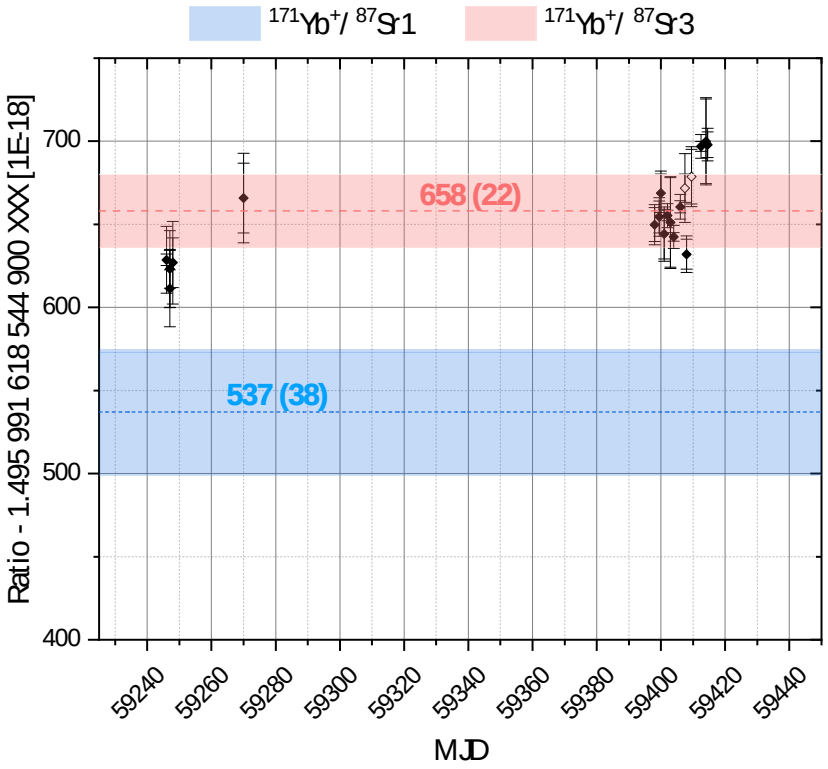

Figure 7.1.: First frequency ratio measurements between PTB's new Sr3 clock and the on campus Yb^{+} single Ion clock throughout the first half of 2021. The Yb^{+} clock is the same as Sr1 was compared to in [10]. The blue dashed line and shaded area illustrate the Yb^{+}/Sr1 ratio and 1-σ uncertainty obtained in [10]. The measured Yb^{+}/Sr3 ratios (black dots) are significantly higher and yield in a weighted mean of 1.495 991 618 544 900 658(22) (red). The reason remains unclear and will be investigated. Two measurements were performed with significantly hotter atoms in Sr3 (black open circles).

8. Summary and outlook

8.1. Summary

In this work the setup of the new cryogenic Sr-lattice clock, Sr3 was described in detail. The experiment was successfully operated from decelerating the atoms in the atomic beam by using a Zeeman slower, capturing and cooling them in the two different MOT stages and transfer to the vertical optical lattice. Preparation of the atomic ensemble for spectroscopy in the outermost $m_F = \pm 9/2$ magnetic sublevels of the $^3\mathrm{P}_0$ upper clock state was demonstrated. Finally, Fourier limited transition linewidth on the $^1\mathrm{S}_0 - {}^3\mathrm{P}_0$ clock transition was achieved at both operational temperatures, ambient- and cryogenic temperature of the cryostat and clock operation was demonstrated. It was found that the vibrations induced by the pulse tube cooler do not pose a limitation for clock operation. Its key ability to operate at either room temperature or cryogenic temperature of about 80 K has been demonstrated. Operating Sr3 at either temperature reduces the black-body radiation frequency shift uncertainty by more than a factor of 5 compared to its predecessor system Sr1. In addition a full characterization of all relevant systematic effects causing frequency shifts on the clock transition has been presented and finalized in a complete uncertainty budget in Tab. 3.4. Furthermore first measurements of the absolute frequency of Sr3 have been presented (Sec. 6) in addition to the long therm measurements performed with Sr1 that have been published in [8]. The absolute frequency obtained with Sr3 are in agreement with previous publications from our group (Fig.6.1) and meet the recommendation by the BIPM [69]. In addition measurements of the frequency ratio of both Sr1 or Sr3 with the on campus ^{171}Ytterbium single Ion clock have been performed. These measurements are spanning over several years with Sr1 and were published in [10]. First measurements of the Yb^+/Sr3 frequency ratio revealed a significant different ratio compared to the Yb^+/Sr1 frequency ratio. On average a deviation of about $12 \cdot 10^{-17}$ was

found. The discrepancy in the average Yb^+/Sr1 and Yb^+/Sr3 ratios is far beyond any of the involved clocks systematic uncertainty. The origin of the large deviation is unclear and under future investigation.

8.2. Outlook

To improve the Sr3 system further in its systematic uncertainty to the level of $1 \cdot 10^{-18}$ and below the uncertainty of several effects must me reduced. In the following some approaches will be discussed to minimize the uncertainty of the leading contributions in the Sr3 uncertainty budget presented in Sec. 3.6.

Installing the atomic beam shutters

As already discussed the open apertures that are required for loading Sr atoms into the MOT an uncertainty contribution by intruding BBR of about $1 \cdot 10^{-18}$ is present during cryogenic operation. Installing the rotateable shutters to suppress the influence of BBR during spectroscopy will reduce this contribution drastically. The remaining uncertainty is predicted to be at the level of below $1 \cdot 10^{-19}$. Hereby it is assumed that the shutters reach a temperature of 130 K as a computer simulation predicts for a cryostat temperature of 80 K. This would reduce the total systematic uncertainty of Sr3 to about $1.9 \cdot 10^{-18}$.

Reducing the lattice lightshift uncertainty

As the lattice lightshift is the leading uncertainty contribution during cryogenic operation its reduction poses a big leap in reducing Sr3's total uncertainty. In detail the uncertainty arises due to the axial temperature of the atoms in the lattice ($T_z = 2\,\mu\text{K}/(5\,\mu\text{K})$ in the shallow/deep lattice) although spilling is already in use. Recently preliminary tests of axial sideband cooling were performed on Sr3 in combination to spilling. The axial temperature was reduced significantly. Using the model described in [53] the lattice lightshift uncertainty does not react as hoped for. To further reduce the uncertainty better knowledge of the E2M1 lightsift coefficient α^{qm} is required. At present its uncertainty is fairly large to attribute the discrepancy in published values as discussed in Sec. 2.6.3 and 3.5.6. Without solving this issue it will be fairly difficult to surpass a systematic uncertainty of 10^{-18} even with shallow lattices.

Further reduction of measurement uncertainty

Two further uncertainty contributions arise from the statistical uncertainties of interleaved measurements in the characterization of the BBR shift from the oven and the collisional frequency shift. Extending the measurement duration will also reduce the uncertainties on these contributions.

Improving the vacuum pressure

To date the vacuum pressure at the 10^{-10}mbar level in the main chamber. During operation it gets degraded by app. a factor of two when the oven has reached its typical operation temperature of about 500 °C. An additional differential pumping stage between the oven and the Zeeman slower can help to prevent vacuum pressure increase in the main chamber which will have a positive effect on the atoms lifetime in the optical lattice. An increase in lifetime will reduce the background collisional frequency shift and uncertainty.

Further Yb^+/Sr frequency ratio measurements

Since the discrepancy in the Yb^+/Sr frequency ratio is yet unsolved and not covered in magnitude by any of the clocks systematic uncertainty further measurements should to be conducted. It is yet unclear whether there is an unknown systematic effect acting any of the involved clocks. Adding another clock at comparable level of systematic uncertainty (low 10^{-17} or below) might reveal if a single clock causes variations in the frequency ratio.

Regular contributions to TAI

As the clock is operated frequently its output frequency data can be used to contribute to TAI regularly which is an additional requirement by the BIPM's road map towards a redefinition of the second.

A. Appendix

A.1. Abbreviations

Sr	Strontium
Yb	Ytterbium
MOT	Magneto-optical trapp
H-maser	Hydrogen maser
NMI	National Metrology Institute
PTB	Physikalisch-Technische Bundesanstalt
BIPM	Bureau International des Poids et Mesures
TAI	International Atomic Time
GPS	Global Positioning System
TTL	Transistor–transistor logic
CSF	Cesium fountain clock
BBR	Black-body radiation
AOM	Acousto-optic modulator

Table A.1.: Table of abbreviations used in this work.

A.2. Sources for Fig. 1.1

Microwave clocks / Year	Frac. unc.	Description	Source
1955	1.06E-10	Essen's Clock	[133]
1991	5E-15	First Cs fountain clocks	[134]
1995	–	SYRTE preliminary	[135]
1998	7E-15	PTB CS1	[136]
1999	1.8E-15	NIST F1	[137]
2001	1.2E-15	PTB CSF1	[138]
2001	1.1E-15	–	[139]
2002	8E-16	PTB CSF1	[140]
2002	9.9E-16	NIST F1	[137]
2005	5.3E-16	NIST F1	[141]
2005	3.3E-16	NIST F1	[142, 143]
2006	8E-16	IEN CSF 1	[144]
2010	3.4E-16	NIST F1	[145]
2010	4E-16	NPL-CsF1	[146]
2012	4.1E-16	PTB CSF2	[147]
2013	2.6E-16	SYRTE FO2	[54]
2014	1E-16	NIST-F2	[12]
2018	1.71E-16	PTB CSF2	[13]
Optical clocks / Year	**Frac. unc.**	**Species**	**Source**
1996	1E-12	Ca	[148]
1997	3.4E-13	H	[149]
2000	1.8E-14	H	[150]
2001	9.5E-15	Hg+	[151]
2003	1E-15	Hg+	[152]
2004	3.4E-15	Sr+	[153]
2006	9.1E-16	Hg+	[154]
2008	2.3E-17	Al+	[4]
2008	1.9E-17	Hg+	[4]
2008	1.5E-16	Sr	[155]
2009	4.5E-16	Yb+	[156]
2009	3.4E-16	Yb	[102]
2010	8.6E-18	Al+	[157]
2011	7E-17	Yb+ (E3)	[158]
2012	2E-17	Sr+	[159]
2013	3E-17	Sr	[62]
2014	6E-18	Sr	[88]
2014	3E-18	Yb+ (E3)	PTB unpublished
2015	2E-18	Sr	[44]
2016	3E-18	Yb+	[160]
2016	1.7E-16	Hg	[161]
2018	1.4E-18	Yb	[162]
2019	9.5E-19	Al+	[163]
2019	2E-18	Sr	[47]
2021	3E-18	Ca+	[164]
2021	2.7E-18	Sr	This work

A.3. Assembly of Pt100 sensors at the cryostat

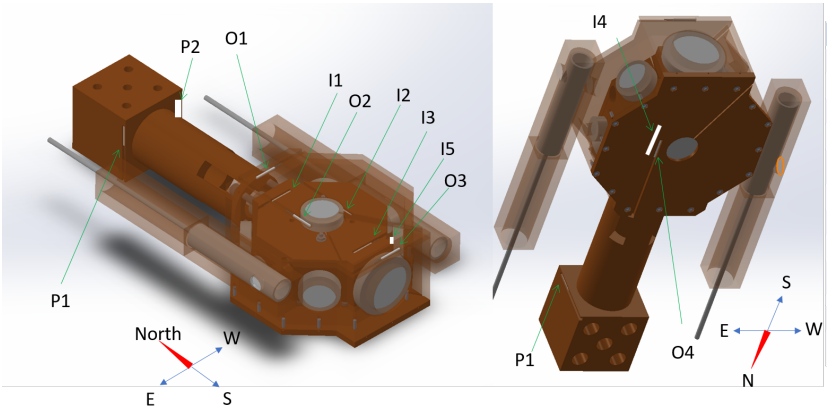

Label	Description	Sensor #
P1	Pylon	RS (293-8480)
O1	OuterShield (north)	8
O2	OuterShield (east)	6
O3	OuterShield (south)	9
O4	Outer Shield Lid (east)	10
I1	InnerShield (north)	1
I2	InnerShield (west)	2
I3	InnerShield (south)	3
I4	InnerShield Lid (east)	4
P2	Pylon Auxiliary	7
I5	InnerShield Auxiliary (south)	5

Figure A.1.: Pt100 Sensor positions at the cryostat.

A.4. Assembly of the electrodes in the cryostat

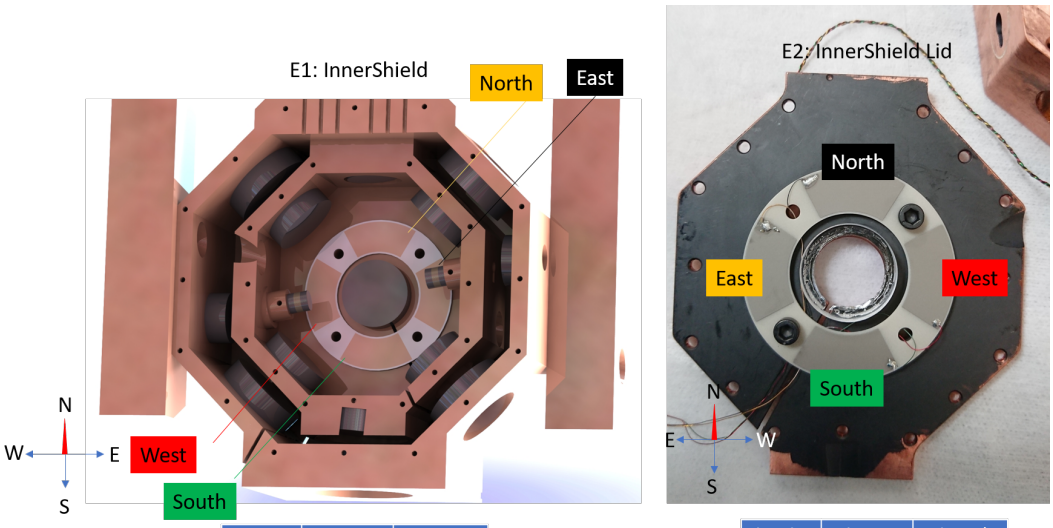

Electrode	Pad	Resistance* / Ohm
E1	North	8.7
E1	East	8.5
E1	South	8.7
E1	West	9.0

*Measured from connetor Pin to the farest spot on the ceramic Pad

Measured with Voltcraft VC 220 Handheld Multimeter

Electrode	Pad	Resistance / Ohm
E2 (Lid)	North	9.3
E2 (Lid)	East	9.2
E2 (Lid)	South	9.2
E2 (Lid)	West	9.5

Figure A.2.: Assembly and electrical connection of electrodes installed inside the inner shield of the cryostat.

A.5. Pin assignment

Port Alfa (upper)

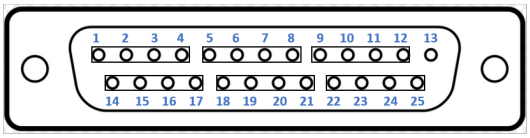

Pin#	Sensor#	Color	Pin#	Sensor#	Color
1	4	Black	14	E1	North (Gold)
2	4	Gold	15	E1	East (Black)
3	4	Red	16	E1	South (Green)
4	4	Green	17	E1	West (Red)
5	3	Black	18	1	Black
6	3	Gold	19	1	Gold
7	3	Red	20	1	Red
8	3	Green	21	1	Green
9	5	Black	22	9	Black
10	5	Gold	23	9	Gold
11	5	Red	24	9	Red
12	5	Green	25	9	Green
13					

Port Bravo (lower)

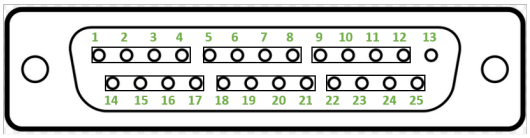

Pin#	Sensor#	Color	Pin#	Sensor#	Color
1	10	Black	14	8	Black
2	10	Gold	15	8	Gold
3	10	Red	16	8	Red
4	10	Green	17	8	Green
5	6	Black	18	RS	Black
6	6	Gold	19	RS	Gold
7	6	Red	20	RS	Red
8	6	Green	21	RS	Green
9	2	Black	22	E2 (Lid)	North (Black)
10	2	Gold	23	E2 (Lid)	East (Gold)
11	2	Red	24	E2 (Lid)	South (Green)
12	2	Green	25	E2 (Lid)	West (Red)
13					

Figure A.3.: Pin assignment of the Pt100 Sensors and the electrodes installed at the cryostat.

A.6. Uncertainty contribution of the missing cryogenic beam shutters

The uncertainty of the frequency shift contribution due to the missing cryogenic beam shutters discussed in Sec. 3.2.6 is given by Gaussian error propagation:

$$u(\Delta\nu_{AIT}) = 2\sqrt{(\Omega\ \Omega_{eff,mean}\ u(\Delta\nu_{ext}))^2 + (-\Omega\ \Omega_{eff,mean}\ u(\Delta\nu_{int}))^2 + \left(\frac{\Delta\nu_{AIT}}{\Omega}\ u(\Omega)\right)^2 + \left(\frac{\Delta\nu_{AIT}}{\Omega_{eff,mean}}\ u(\Omega_{eff,mean})\right)^2} \quad \text{(A.1)}$$

A.7. DC-Stark shift evaluation

A.7.1. Constructing the coordinate system

To calculate the angles between the different field vectors a set of three geometrically independent base vectors $\hat{e}_1$, $\hat{e}_2$ and $\hat{e}_3$ must be constructed. In this case the base vectors are NOT orthogonal since they originate from the non orthogonal arrangement of the fields the electrodes produce. The derivation of the base vectors can be found in the appendix

The direction "ANBS" is chosen as reference for the first base vector

$$\hat{e}_1 = \begin{pmatrix} 1 \\ 0 \\ 0 \end{pmatrix}$$

Here the angle between the applied electric fields on "ANBS" and "ASBN" (denoted $\sphericalangle\text{ANBS, ASBN}$) is denoted as α in Eq. 3.20. The second unit vector is defined as

$$\hat{e}_2 = \begin{pmatrix} \cos(\alpha) \\ \sin(\alpha) \\ 0 \end{pmatrix}$$

Constituting of the third base vector $\hat{e}_3$ is more complicated. To shorten its expression the following definition is introduced

$$\hat{e}_3 = \begin{pmatrix} a \\ b \\ c \end{pmatrix}$$

with

$$a = \hat{e}_1\hat{e}_3 = \cos(\beta) = \begin{pmatrix}1\\0\\0\end{pmatrix}\begin{pmatrix}a\\b\\c\end{pmatrix} \tag{A.2}$$

the first parameter a is found wit β being the angle $\sphericalangle ANBS, AEBW$. Proceeding analogously with b

$$\hat{e}_2\hat{e}_3 = \begin{pmatrix}\cos(\alpha)\\\sin(\alpha)\\0\end{pmatrix}\begin{pmatrix}a\\b\\c\end{pmatrix} = a\ \cos(\alpha) + b\ \sin(\alpha) \equiv \cos(\Gamma) \tag{A.3}$$

$$b = \frac{\cos(\gamma) - \cos(\beta)\cos(\alpha)}{\sin(\alpha)} \tag{A.4}$$

and c with Γ the angle $\sphericalangle ASBN, AEBW$. Since the angles between $\hat{e}_3$ and $\hat{e}_1(\hat{e}_2)$ are known and its length must be one, the components a, b, c can be derived using the following equations:

$$a^2 + b^2 + c^2 = 1 \tag{A.5}$$

$$|c| = \sqrt{1 - a^2 - b^2} = \sqrt{1 - \cos^2(\beta) - \frac{\left[\cos(\gamma) - \cos(\beta)\cos(\alpha)\right]^2}{\sin^2(\alpha)}} \tag{A.6}$$

From the quantity of interest $\vec{E}_{bgr}$ the projections onto the applied fields' direction is known so far. To determine its magnitude a set of parameters similar to the previous ones is chosen

$$\vec{E}_{bgr} = \begin{pmatrix}a'\\b'\\c'\end{pmatrix} \tag{A.7}$$

with $\vec{E}_{bgr} \cdot \hat{e}_i = E_i$.

Together with $E_i = -\sqrt{-A_i}(-B_i)$ where E_i is proportional to the square root of the measured frequency shift. The parabola fit parameter A_i is always negative.

Defining the electric field component along our base vectors $\vec{E}_{bgr}\ \hat{e}_i = E_i$ the parameters

$$\vec{E}_{bgr}\hat{e}_1 = a' = E_1 \tag{A.8}$$

$$\vec{E}_{bgr}\hat{e}_2 = E_2 = \begin{pmatrix}a'\\b'\\c'\end{pmatrix}\begin{pmatrix}\cos(\alpha)\\\sin(\alpha)\\0\end{pmatrix} = a'\cos(\alpha) + b'\sin(\alpha) \tag{A.9}$$

$$b' = \frac{E_2 - a'\cos(\alpha)}{\sin(\alpha)} \tag{A.10}$$

$$\vec{E}_{bgr}\hat{e}_3 = E_3 = \begin{pmatrix} a' \\ b' \\ c' \end{pmatrix} \begin{pmatrix} a \\ b \\ c \end{pmatrix} = a'a_3 + b'b_3 + c'c_3 \tag{A.11}$$

hence

$$c' = \frac{E_3 - a'a_3 - b'b_3}{c_3} \tag{A.12}$$

As mentioned in the previous section defining $\hat{e}_1$ along the "ANBS" direction, the projection of the other base vectors to it is calculated. The final frequency shift $\Delta\nu_{\mathrm{dcStark}}$ is the quadratic sum of the squares of the fieldvectors E_1, E_2 and E_3. E_3 allows for a consistency check when replacing the corresponding parameters of direction "AEBW" with those of direction "AWBE", denoting E_3'.

$$\Delta\nu_{\mathrm{dcStark}} = -\left(E_1^2 + E_2^2 + E_3^2\right) \tag{A.13}$$

A.7.2. DC-Stark shift uncertainty evaluation

Calculation of the uncertainty of the angle α:

$$\delta\cos(\alpha) = \sqrt{\left(-\frac{1}{\sqrt{\tilde{A}A}\,\tilde{U}U}\cdot\sigma(\partial\Delta\nu)\right)^2 + \left(2\frac{\partial\Delta\nu}{2\sqrt{\tilde{A}^3A}\,\tilde{U}U}\cdot\delta\tilde{A}\right)^2 + \left(2\frac{\partial\Delta\nu}{\sqrt{\tilde{A}A}\,\tilde{U}^2U}\cdot\delta\tilde{U}\right)^2} \tag{A.14}$$

Uncertainties of the vectors

$$\delta\hat{e}_{1,a} = \delta\hat{e}_{1,b} = \delta\hat{e}_{1,c} = \delta\hat{e}_{2,c} = 0 \tag{A.15}$$

$$\delta\hat{e}_{2,a} = \sqrt{\left(-\sin(\sphericalangle_{\mathrm{ANBS,\ ASBN}})\cdot\delta(\sphericalangle_{\mathrm{ANBS,\ ASBN}})\right)^2} \tag{A.16}$$

$$\delta\hat{e}_{2,b} = \sqrt{\left(\cos(\sphericalangle_{\mathrm{ANBS,\ ASBN}})\cdot\delta(\sphericalangle_{\mathrm{ANBS,\ ASBN}})\right)^2} \tag{A.17}$$

$$\delta\hat{e}_{3,a} = \sqrt{\left(-\sin(\sphericalangle_{\mathrm{ANBS,\ AEBW}})\cdot\delta(\sphericalangle_{\mathrm{ANBS,\ AEBW}})\right)^2} \tag{A.18}$$

$$\delta\hat{e}_{3,b} = \sqrt{\left(-\sin(\sphericalangle_{\text{ASBN, AEBW}}) \cdot \delta(\sphericalangle_{\text{ASBN, AEBW}})\right)^2 + \left(\frac{\cos(\sphericalangle_{\text{ANBS, AEBW}})}{\sin^2(\sphericalangle_{\text{ANBS,ASBN}})} \cdot \delta(\sphericalangle_{\text{ANBS,ASBN}})\right)^2 + \left(\frac{\sin(\sphericalangle_{\text{ANBS, AEBW}})}{\tan(\sphericalangle_{\text{ANBS, ASBN}})} \cdot \delta(\sphericalangle_{\text{ANBS, AEBW}})\right)^2} \tag{A.19}$$

$$\delta\hat{e}_{3,c} = \sqrt{\left(-\frac{\hat{e}_{3,a}}{\hat{e}_{3,c}} \cdot \delta\hat{e}_{3,a}\right)^2 + \left(-\frac{\hat{e}_{3,b}}{\hat{e}_{3,c}} \cdot \delta\hat{e}_{3,b}\right)^2} \tag{A.20}$$

The determination of the uncertainties of the vector $\hat{e}_3'$ used for consistency check is carried out analog to $\hat{e}_3$ simply by replacing the parameters involving the direction "AEBW" with the corresponding parameters of the direction "AWBE".

The error on the field vector follows the same approach but is more complicated for directions other than "ASBN" since the expressions are long-drawn-out. The full derivatives of the GEP for equations A.9 and A.11 are given in the appendix. Again some therms insignificantly contribute to the error and are neglected, simplifying the expressions to

$$\delta E_2 = \sqrt{\left(\frac{1}{\hat{e}_{2,b}} \cdot \delta(\sqrt{\Upsilon} E_{0,\parallel,\text{ASBN}})\right)^2 + \left(\frac{\hat{e}_{2,a} E_1 - \sqrt{\Upsilon} E_{0,\parallel,\text{ASBN}}}{(\hat{e}_{2,b})^2} \cdot \delta\hat{e}_{2,b}\right)^2 + \left(-\frac{E_1}{\hat{e}_{2,b}} \cdot \delta\hat{e}_{2,a}\right)^2 + \left(-\frac{\hat{e}_{2,a}}{\hat{e}_{2,b}} \cdot \delta E_1\right)^2} \tag{A.21}$$

$$\delta E_3 = \sqrt{\left(\frac{1}{\hat{e}_{3,c}} \cdot \delta(\sqrt{\Upsilon} E_{0,\parallel,\text{AEBW}})\right)^2 + \left(\frac{E_1\hat{e}_{3,a} + E_2\hat{e}_{3,a} - \sqrt{\Upsilon} E_{0,\parallel,\text{AEBW}}}{\hat{e}_{3,c}} \cdot \delta\hat{e}_{3,c}\right)^2 + \left(-\frac{\hat{e}_{3,a}}{\hat{e}_{3,c}} \cdot \delta E_1\right)^2 + \left(-\frac{E_1}{\hat{e}_{3,c}} \cdot \delta\hat{e}_{3,a}\right)^2 + \left(-\frac{\hat{e}_{3,b}}{\hat{e}_{3,c}} \cdot \delta E_2\right)^2 + \left(-\frac{E_2}{\hat{e}_{3,c}} \cdot \delta\hat{e}_{3,b}\right)^2} \tag{A.22}$$

Roman Schwarz Date of birth 31.01.1985 in Lübeck
Married, 2 children

CV

2004	Abitur
2011	FH-Diplom
2012 - 2015	RnD Engineer Coherent LaserSystems GmbH & Co. KG.
2015 - 2022	PhD student at PTB

Acknowledgements

Throughout the time working on this thesis I have received a great deal of support and assistance. I express my gratitude to those who working with me and to those who gave their supported.

I thank my supervisor Christian Lisdat for making this work possible by offering me a position. I appreciated his passion for working in science and the time we spent in the lab bringing Sr3 to life.

Sören Dörscher who always had an open ear when it came to difficult questions and promptly had good ideas on hand and Sofia Herbers for endless exchange of present time information. I really enjoyed working with you. Thank you for your support and for critically reviewing this manuscript.

Ali Al-Masoudi, Stefan Vogt, Silvio Koller, Jacopo Grotti, Chetan Vishwakarma, Ingo Nosske, Tim Lücke, Jay Sandip Mangaonkar, Evgenij Pachomow, Veit Dahlke, Nina Meyer, Florian Krause, Chun Yu Ma, Daniele Nicolodi, Andreas Noack Erik Benkler, Christian Grebing, Thomas Legero, Tobias Ohlendorf, Jialian Yu, Dan Matei, Robin Weyrich, Alexander Kuhl, Sebastian Koke, Thomas Waterholter, Jingxian Ji, Jaffar Kadum, Atif Shehzad, Sebastian Häfner, Andre Uhde, Mandy Rindermann, Klemens Budin, Patrik Knigge, Andreas Koczwara, Mattias Misera, Marion Wengel, Susanne Ehrenpfordt, Ute Krüger, Birgit Ohlendorf, Uwe Sterr, Gesine Grosche and Harald Schnatz.

Special thanks to Wolfgang Ertmer who attended as referee during my PhD defense and Klemens Hammerer as the head of the board.

Last but not least, I thank my beloved family for always giving me tremendous support through difficult times. Thank you Liam, Neo and Anne!

Bibliography

[1] A. Derevianko and M. Pospelov. Hunting for topological dark matter with atomic clocks. *Nature Physics*, 10:933–936, 2014.

[2] Asimina Arvanitaki, Junwu Huang, and Ken Van Tilburg. Searching for dilaton dark matter with atomic clocks. *Phys. Rev. D*, 91:015015, Jan 2015.

[3] E. Peik, B. Lipphardt, H. Schnatz, T. Schneider, Chr. Tamm, and S. G. Karshenboim. Limit on the present temporal variation of the fine structure constant. *Phys. Rev. Lett.*, 93:170801, 2004.

[4] T. Rosenband, D. B. Hume, P. O. Schmidt, C. W. Chou, A. Brusch, L. Lorini, W. H. Oskay, R. E. Drullinger, T. M. Fortier, J. E. Stalnaker, S. A. Diddams, W. C. Swann, N. R. Newbury, W. M. Itano, D. J. Wineland, and J. C. Bergquist. Frequency ratio of Al^+ and Hg^+ single-ion optical clocks; metrology at the 17th decimal place. *Science*, 319:1808–1812, 2008.

[5] N. Huntemann, B. Lipphardt, Chr. Tamm, V. Gerginov, S. Weyers, and E. Peik. Improved limit on a temporal variation of m_p/m_e from comparisons of Yb^+ and Cs atomic clocks. *Phys. Rev. Lett.*, 113:210802, 2014.

[6] Christian Sanner, Nils Huntemann, Richard Lange, Christian Tamm, Ekkehard Peik, Marianna S. Safronova, and Sergey G. Porsev. Optical clock comparison test of Lorentz symmetry. *Nature*, 567:204–208, 2019.

[7] Arne Bjerhammar. On a relativistic geodesy. *Bulletin Géodésique*, 59:207–220, 1985.

[8] R. Schwarz, S. Dörscher, A. Al-Masoudi, E. Benkler, T. Legero, U. Sterr, S. Weyers, J. Rahm, B. Lipphardt, and C. Lisdat. Long term measurement of the ^{87}Sr clock frequency at the limit of primary Cs clocks. *Phys. Rev. Research*, 2:033242, Aug 2020.

[9] C. Grebing, A. Al-Masoudi, S. Dörscher, S. Häfner, V. Gerginov, S. Weyers, B. Lipphardt, F. Riehle, U. Sterr, and C. Lisdat. Realization of a timescale with an accurate optical lattice clock. *Optica*, 3:563–569, 2016.

[10] Sören Dörscher, Nils Huntemann, Roman Schwarz, Richard Lange, Erik Benkler, Burghard Lipphardt, Uwe Sterr, Ekkehard Peik, and Christian Lisdat. Optical frequency ratio of a $^{171}Yb^+$ single-ion clock and a ^{87}Sr lattice clock. *Metrologia*, 58:015005, 2021.

[11] L. Essen and J. V. L. Parry. The caesium frequency standard. In *NPL News*, volume 65. National Physics Laboratory, Teddington, UK, September 1955.

[12] S. R. Jefferts, T. P. Heavner, T. E. Parker, J. H. Shirley, E. A. Donley, N. Ashby, F. Levi, D. Calonico, and G. A. Costanzo. High-accuracy measurement of the blackbody radiation frequency shift of the ground-state hyperfine transition in ^{133}Cs. *Phys. Rev. Lett.*, 112:050801, Feb 2014.

[13] S. Weyers, V. Gerginov, M. Kazda, J. Rahm, B. Lipphardt, G. Dobrev, and K. Gibble. Advances in the accuracy, stability, and reliability of the PTB primary fountain clocks. *Metrologia*, 55(6):789–805, 2018.

[14] BIPM. Recommended values of standard frequencies. online at https://www.bipm.org/en/publications/mises-en-pratique/standard-frequencies.html, Page last updated: 30 November 2018.

[15] R. W. P. Drever, J. L. Hall, F. V. Kowalski, J. Hough, G. M. Ford, A. J. Munley, and H. Ward. Laser phase and frequency stabilization using an optical resonator. *Appl. Phys. B*, 31:97–105, 1983.

[16] Sebastian Häfner, Stephan Falke, Christian Grebing, Stefan Vogt, Thomas Legero, Mikko Merimaa, Christian Lisdat, and Uwe Sterr. 8×10^{-17} fractional laser frequency instability with a long room-temperature cavity. *Opt. Lett.*, 40:2112–2115, 2015.

[17] D. G. Matei, T. Legero, S. Häfner, C. Grebing, R. Weyrich, W. Zhang, L. Sonderhouse, J. M. Robinson, J. Ye, F. Riehle, and U. Sterr. 1.5 μm lasers with sub-10 mHz linewidth. *Phys. Rev. Lett.*, 118:263202, 2017.

[18] Jörn Stenger, Harald Schnatz, Christian Tamm, and Harald R. Telle. Ultra-precise measurement of optical frequency ratios. *Phys. Rev. Lett.*, 88:073601, 2002.

[19] Erik Benkler, Burghard Lipphardt, Thomas Puppe, Rafał Wilk, Felix Rohde, and Uwe Sterr. End-to-end topology for fiber comb based optical frequency transfer at the 10^{-21} level. *Opt. Express*, 27(25):36886–36902, dec 2019. also see erratum: [165].

[20] Joint Committee for Guides in Metrology (JCGM). *International vocabulary of metrology – Basic and general concepts and associated terms (VIM).* 3 edition.

[21] D. W. Allan. Statistics of atomic frequency standards. *Proc. IEEE*, 54:221–230, 1966.

[22] J. A. Barnes, A. R. Chi, L. S. Cutler, D. J. Healey, D. B. Leeson, T. E. McGunigal, J. A. Mullan, W. L. Smith, R. L. Sydnor, R. F. C. Vessot, and G. M. R. Winkler. Characterization of frequency stability. *IEEE Trans. Instrum. Meas.*, IM-20:105–120, 1971. see corrections in NIST TN-1337 [166].

[23] J. R. Vig. Quartz crystal oscillators and resonators. http://www.ieee-uffc.org/fc, October 1999. SLCET-TR-88-1 (Rev. 8.3.9).

[24] Hidetoshi Katori. Spectroscopy of strontium atoms in the Lamb-Dicke confinement. In P. Gill, editor, *Proceedings of the Sixth Symposium on Frequency Standards and Metrology, 9–14 September 2001, St. Andrews, Scotland*, pages 323–330, Singapore, 2002. World Scientific.

[25] Juan A. Muniz, Dylan J. Young, Julia R. K. Cline, and James K. Thompson. Cavity-QED measurements of the ^{87}Sr millihertz optical clock transition and determination of its natural linewidth. *Phys. Rev. Research*, 3:023152, May 2021.

[26] Bruno Sanguinetti, Enrico Pomarico, Pavel Sekatski, Hugo Zbinden, and Nicolas Gisin. Quantum cloning for absolute radiometry. *Phys. Rev. Lett.*, 105:080503, 2010.

[27] A. V. Taichenachev, V. I. Yudin, C. W. Oates, C. W. Hoyt, Z. W. Barber, and L. Hollberg. Magnetic field-induced spectroscopy of forbidden optical transitions with application to lattice-based optical atomic clocks. *Phys. Rev. Lett.*, 96:083001, 2006.

[28] Stefano Origlia. *A high-performance bosonic optical lattice clock*. PhD thesis, Faculty of Mathematics and Natural Sciences at the Heinrich-Heine-Universität Düsseldorf, 2018.

[29] Ian R. Hill, Yuri B. Ovchinnikov, Elizabeth M. Bridge, Anne E. Curtis, Sean Donnellan, and Patrick Gill. A simple, configurable, permanent magnet Zeeman slower for Sr. In *European Frequency and Time Forum (EFTF), 2012*, pages 545–549. IEEE, 2012.

[30] Stefan Vogt, Sebastian Häfner, Jacopo Grotti, Silvio Koller, Ali Al-Masoudi, Uwe Sterr, and Christian Lisdat. A transportable optical lattice clock. *J. Phys.: Conf. Ser.*, 723:012020, 2016.

[31] Harold J. Metcalf and Peter van der Straten. *Laser Cooling and Trapping*. Springer, New York, Berlin, Heidelberg, 1999.

[32] Yuri B. Ovchinnikov. A Zeeman slower based on magnetic dipoles. *Opt. Commun.*, 276:261–267, 2007.

[33] Stefan Vogt. *Eine transportable optische Gitteruhr basierend auf Strontium*. PhD thesis, QUEST-Leibniz-Forschungsschule der Universität Hannover, 2015.

[34] Roman Schwarz, Sören Dörscher, Ali Al-Masoudi, Stefan Vogt, Ye Li, and Christian Lisdat. A compact and robust cooling laser system for an optical strontium lattice clock. *Rev. Sci. Instrum.*, 90(2):023109, 2019.

[35] Martin M. Boyd. *High Precision Spectroscopy of Strontium in an Optical Lattice: Towards a New Standard for Frequency and Time*. PhD thesis, Graduate School of the University of Colorado, 2007.

[36] Takashi Mukaiyama, Hidetoshi Katori, Tetsuya Ido, Ying Li, and Makoto Kuwata-Gonokami. Recoil-limited laser cooling of Sr atoms near the Fermi temperature. *Phys. Rev. Lett.*, 90(11):113002, 2003.

[37] Hidetoshi Katori, Koji Hashiguchi, E. Yu. Il'inova, and V. D. Ovsiannikov. Magic wavelength to make optical lattice clocks insensitive to atomic motion. *Phys. Rev. Lett.*, 103:153004, 2009.

[38] M. Takamoto, H. Katori, S. I. Marmo, V. D. Ovsiannikov, and V. G. Pal'chikov. Prospects for optical clocks with a blue-detuned lattice. *Phys. Rev. Lett.*, 102:063002, 2009.

[39] S. Blatt, J. W. Thomsen, G. K. Campbell, A. D. Ludlow, M. D. Swallows, M. J. Martin, M. M. Boyd, and J. Ye. Rabi spectroscopy and excitation inhomogeneity in a one-dimensional optical lattice clock. *Phys. Rev. A*, 80:052703, 2009.

[40] Pierre Lemonde and Peter Wolf. Optical lattice clock with atoms confined in a shallow trap. *Phys. Rev. A*, 72:033409, 2005.

[41] R. H. Dicke. The effect of collisions upon the Doppler width of spectral lines. *Phys. Rev.*, 89:472–473, 1953.

[42] Martin M. Boyd, Tanya Zelevinsky, Andrew D. Ludlow, Sebastian Blatt, Thomas Zanon-Willette, Seth M. Foreman, and Jun Ye. Nuclear spin effects in optical lattice clocks. *Phys. Rev. A*, 76:022510, 2007.

[43] G. John Dick. Local oscillator induced instabilities in trapped ion frequency standards. In *Proceedings of* 19^{th} *Annu. Precise Time and Time Interval Meeting, Redendo Beach, 1987*, pages 133–147, Washington, DC, 1988. U.S. Naval Observatory.

[44] T. L. Nicholson, S. L. Campbell, R. B. Hutson, G. E. Marti, B. J. Bloom, R. L. McNally, W. Zhang, M. D. Barrett, M. S. Safronova, G. F. Strouse, W. L. Tew, and J. Ye. Systematic evaluation of an atomic clock at 2×10^{-18} total uncertainty. *Nature Commun.*, 6:6896, 2015.

[45] Thomas Middelmann, Stephan Falke, Christian Lisdat, and Uwe Sterr. High accuracy correction of blackbody radiation shift in an optical lattice clock. *Phys. Rev. Lett.*, 109:263004, Dec 2012.

[46] Ch. Lisdat, S. Dörscher, I. Nosske, and U. Sterr. Blackbody radiation shift in strontium lattice clocks revisited. *Phys. Rev. Research*, 3:L042036, Dec 2021.

[47] Tobias Bothwell, Dhruv Kedar, Eric Oelker, John M. Robinson, Sarah L. Bromley, Weston L. Tew, Jun Ye, and Colin J. Kennedy. JILA SrI optical lattice clock with uncertainty of 2.0×10^{-18}. *Metrologia*, 56(6):065004, oct 2019.

[48] Evaluation of measurement data – guide to the expression of uncertainty in measurement. JCGM 100:2008, 2008.

[49] Masao Takamoto and Hidetoshi Katori. Spectroscopy of the $^1S_0 \rightarrow ^3P_0$ clock transition of ^{87}Sr in an optical lattice. *Phys. Rev. Lett.*, 91:223001, 2003.

[50] Kai Guo, Guangfu Wang, and Anpei Ye. Dipole polarizabilities and magic wavelengths for a Sr and Yb atomic optical lattice clock. *J. Phys. B: At. Mol. Phys.*, 43(13):135004, 2010.

[51] P. G. Westergaard, J. Lodewyck, L. Lorini, A. Lecallier, E. A. Burt, M. Zawada, J. Millo, and P. Lemonde. Lattice-induced frequency shifts in Sr optical lattice clocks at the 10^{-17} level. *Phys. Rev. Lett.*, 106:210801, 2011.

[52] Hidetoshi Katori, V. D. Ovsiannikov, S. I. Marmo, and V. G. Palchikov. Strategies for reducing the light shift in atomic clocks. *Phys. Rev. A*, 91:052503, 2015.

[53] Ichiro Ushijima, Masao Takamoto, and Hidetoshi Katori. Operational magic intensity for Sr optical lattice clocks. *Phys. Rev. Lett.*, 121:263202, Dec 2018.

[54] R. Le Targat, L. Lorini, Y. Le Coq, M. Zawada, J. Guéna, M. Abgrall, M. Gurov, P. Rosenbusch, D. G. Rovera, B. Nagórny, R. Gartman, P. G. Westergaard, M. E. Tobar, M. Lours, G. Santarelli, A. Clairon, S. Bize, P. Laurent, P. Lemonde, and J. Lodewyck. Experimental realization of an optical second with strontium lattice clocks. *Nature Commun.*, 4:2109, 2013.

[55] S.G. Porsev, M.S. Safronova, U.I. Safronova, and M.G. Kozlov. Multipolar polarizabilities and hyperpolarizabilities in the Sr optical lattice clock. *Phys. Rev. Lett.*, 120:063204, Feb 2018.

[56] V. D. Ovsiannikov, S. I. Marmo, V. G. Palchikov, and H. Katori. Higher-order effects on the precision of clocks of neutral atoms in optical lattices. *Phys. Rev. A*, 93:043420, Apr 2016.

[57] Ali Al-Masoudi. *A strontium lattice clock with reduced blackbody radiation shift.* PhD thesis, Leibniz Universität Hannover, 2016. online available at http://www.tib.uni-hannover.de.

[58] Philip G. Westergaard, Jérôme Lodewyck, and Pierre Lemonde. Minimizing the Dick effect in an optical lattice clock. *IEEE Trans. Ultrason. Ferroelectr. Freq. Control*, 57(3):623–628, 2010.

[59] St. Falke, H. Schnatz, J. S. R. Vellore Winfred, Th. Middelmann, St. Vogt, S. Weyers, B. Lipphardt, G. Grosche, F. Riehle, U. Sterr, and Ch. Lisdat. The ^{87}Sr optical frequency standard at PTB. *Metrologia*, 48:399–407, 2011.

[60] Benquan Lu, Xiaotong Lu, Jiguang Li, and Hong Chang. Theoretical calculation of the quadratic zeeman shift coefficient of the $^3P_0^o$ clock state for strontium optical lattice clock. *Chinese Physics B*, accepted paper, 2022.

[61] Richard Hobson. *An optical lattice clock with neutral strontium.* PhD thesis, Balliol College, University of Oxford, 2016.

[62] Stephan Falke, Nathan Lemke, Christian Grebing, Burghard Lipphardt, Stefan Weyers, Vladislav Gerginov, Nils Huntemann, Christian Hagemann, Ali Al-Masoudi, Sebastian Häfner, Stefan Vogt, Uwe Sterr, and Christian Lisdat. A strontium lattice clock with 3×10^{-17} inaccuracy and its frequency. *New J. Phys.*, 16:073023, 2014.

[63] Sebastian Häfner. *Ultrastabile Lasersysteme für Weltraum- und Boden-Anwendungen*. PhD thesis, Leibniz Universität Hannover, 2015.

[64] Stephan Falke, Mattias Misera, Uwe Sterr, and Christian Lisdat. Delivering pulsed and phase stable light to atoms of an optical clock. *Appl. Phys. B*, 107:301–311, 2012.

[65] Nikolaos K. Pavlis and Marc A. Weiss. The relativistic redshift with 3×10^{-17} uncertainty at NIST, Boulder, Colorado, USA. *Metrologia*, 40:66–73, 2003.

[66] C Voigt, H Denker, and L Timmen. Time-variable gravity potential components for optical clock comparisons and the definition of international time scales. *Metrologia*, 53(6):1365, 2016.

[67] Fritz Riehle, Carsten Degenhardt, Christian Lisdat, Guido Wilpers, Harald Schnatz, Tomas Binnewies, Hardo Stoehr, and Uwe Sterr. An optical frequency standard with cold and ultra-cold calcium atoms. In S. G. Karshenboim and E. Peik, editors, *Astrophysics, Clocks and Fundamental Constants*, volume 648 of *Lecture Notes in Physics*, pages 229–244. Springer, Berlin, Heidelberg, New York, 2004.

[68] W.J. Riley. Handbook of frequency stability analysis. NIST special publication 1065, NIST, 2008.

[69] Bureau International des Poids et Mesures. Recommended values of standard frequencies for applications including the practical realization of the metre and secondary representations of the definition of the second. Pavillon de Breteuil, F-92310 Sèvres, France. Approved by the CCTF in June 2017, File last updated August 2018.

[70] Ali Al-Masoudi, Sören Dörscher, Sebastian Häfner, Uwe Sterr, and Christian Lisdat. Noise and instability of an optical lattice clock. *Phys. Rev. A*, 92:063814, 2015.

[71] B. M. Roberts, P. Delva, A. Al-Masoudi, A. Amy-Klein, C. Bærentsen, C. F. A. Baynham, E. Benkler, S. Bilicki, W. Bowden, E. Cantin, E. A. Curtis, S. Dörscher, F. Frank, P. Gill, R. M. Godun, G. Grosche, A. Hees, I. R. Hill, R. Hobson, N. Huntemann, J. Kronjäger, S. Koke, A. Kuhl, R. Lange, T. Legero, B. Lipphardt, C. Lisdat, J. Lodewyck, O. Lopez, H. S. Margolis, H. Álvarez-Martínez, F. Meynadier, F. Ozimek, E. Peik, P.-E. Pottie, N. Quintin, R. Schwarz, C. Sanner, M. Schioppo, A. Silva, U. Sterr, Chr. Tamm, R. LeTargat, P. Tuckey, G. Vallet, T. Waterholter, D. Xu, and P. Wolf. Search for transient variations of the fine structure constant and dark matter using fiber-linked optical atomic clocks. *New J. Phys.*, 22:093010, Jul 2020.

[72] Jacopo Grotti, Silvio Koller, Stefan Vogt, Sebastian Häfner, Uwe Sterr, Christian Lisdat, Heiner Denker, Christian Voigt, Ludger Timmen, Antoine Rolland, Fred N. Baynes, Helen S. Margolis, Michel Zampaolo, Pierre Thoumany, Marco Pizzocaro, Benjamin Rauf, Filippo Bregolin, Anna Tampellini, Piero Barbieri, Massimo Zucco, Giovanni A. Costanzo, Cecilia Clivati, Filippo Levi, and Davide Calonico. Geodesy and metrology with a transportable optical clock. *Nature Physics*, 14:437–441, 2018.

[73] Jérôme Lodewyck, Philip G. Westergaard, and Pierre Lemonde. Nondestructive measurement of the transition probability in a sr optical lattice clock. *Phys. Rev. A*, 79:061401(R)–1–4, 2009.

[74] Richard Hobson, William Bowden, Alvise Vianello, Ian R. Hill, and Patrick Gill. Cavity-enhanced non-destructive detection of atoms for an optical lattice clock. *Opt. Express*, 27(26):37099–37110, Dec 2019.

[75] Ole Kock, Wei He, Dariusz Swierad, Lyndsie Smith, Joshua Hughes, Kai Bongs, and Yeshpal Singh. Laser controlled atom source for optical clocks. *Scientific Reports*, 6:37321, Nov 2016.

[76] Masami Yasuda, Takehiko Tanabe, Takumi Kobayashi, Daisuke Akamatsu, Takumi Sato, and Atsushi Hatakeyama. Laser-controlled cold ytterbium atom source for transportable optical clocks. *J. Phys. Soc. Jpn.*, 86(12):125001, 2017.

[77] V. Lebedev and D. M. Weld. Self-assembled Zeeman slower based on spherical permanent magnets. *J. Phys. B: At. Mol. Phys.*, 47:155003, 2014.

[78] J. Huckans, W. Dubosclard, E. Maréchal, O. Gorceix, B. Laburthe-Tolra, and M. Robert de Saint-Vincent. Note on the reflectance of mirrors exposed to a strontium beam. arXiv:1802.08499 [physics.atom-ph], Feb. 2018.

[79] Ichiro Ushijima, Masao Takamoto, Manoj Das, Takuya Ohkubo, and Hidetoshi Katori. Cryogenic optical lattice clocks. *Nature Photonics*, 9:185–189, 2015.

[80] K. Beloy, N. Hinkley, N. B. Phillips, J. A. Sherman, M. Schioppo, J. Lehman, A. Feldman, L. M. Hanssen, C. W. Oates, and A. D. Ludlow. An atomic clock with 1×10^{-18} room-temperature blackbody Stark uncertainty. *Phys. Rev. Lett.*, 113:260801, Dec 2014.

[81] Thomas Middelmann, Stephan Falke, Christian Lisdat, and Uwe Sterr. Long range transport of ultra cold atoms in a far-detuned one-dimensional optical lattice. *New J. Phys.*, 14:073020, April 2012.

[82] Mira Naftaly and Robert E. Miles. Terahertz time-domain spectroscopy for material characterization. *Proc. IEEE*, 95:1658–1665, 2007.

[83] H Preston-Thomas. The international temperature scale of 1990 (its-90). *Metrologia*, 27(1):3–10, 1990. see erratum its90a,for T-T90 also see [167].

[84] Moustafa Abdel-Hafiz, Piotr Ablewski, Ali Al-Masoudi, Héctor Álvarez Martínez, Petr Balling, Geoffrey Barwood, Erik Benkler, Marcin Bober, Mateusz Borkowski, William Bowden, Roman Ciuryło, Hubert Cybulski, Alexandre Didier, Miroslav Doležal, Sören Dörscher, Stephan Falke, Rachel M. Godun, Ramiz Hamid, Ian R. Hill, Richard Hobson, Nils Huntemann, Yann Le Coq, Rodolphe Le Targat, Thomas Legero, Thomas Lindvall, Christian Lisdat, Jérôme Lodewyck, Helen S. Margolis, Tanja E. Mehlstäubler, Ekkehard Peik, Lennart Pelzer, Marco Pizzocaro, Benjamin Rauf, Antoine Rolland, Nils Scharnhorst, Marco Schioppo, Piet O. Schmidt, Roman Schwarz, Çağrı Şenel, Nicolas Spethmann, Uwe Sterr, Christian Tamm, Jan W. Thomsen, Alvise Vianello, and Michał Zawada. Guidelines for developing optical clocks with 10^{-18} fractional frequency uncertainty. arXiv:1906.11495 [physics.atom-ph], 2019.

[85] Guide to the expression of uncertainty in measurement. ISO/TAG 4. Published by ISO, 1993 (corrected and reprinted, 1995) in the name of the BIPM, IEC, IFCC, ISO, UPAC, IUPAP and OIML, 1995. ISBN number: 92-67-10188-9, 1995.

[86] Harald R. Telle. Private Mitteilungen, 2002.

[87] E. Oelker, R. B. Hutson, C. J. Kennedy, L. Sonderhouse, T. Bothwell, A. Goban, D. Kedar, C. Sanner, J. M. Robinson, G. E. Marti, D. G. Matei, T. Legero, M. Giunta, R. Holzwarth, F. Riehle, U. Sterr, and J. Ye. Demonstration of 4.8×10^{-17} stability at 1 s for two independent optical clocks. *Nature Photonics*, 13:714–719, 2019.

[88] B. J. Bloom, T. L. Nicholson, J. R. Williams, S. L. Campbell, M. Bishof, X. Zhang, W. Zhang, S. L. Bromley, and J. Ye. An optical lattice clock with accuracy and stability at the 10^{-18} level. *Nature*, 506:71–75, 2014.

[89] Jerôme Lodewyck, Michal Zawada, Luca Lorini, Mikhail Gurov, and Pierre Lemonde. Observation and cancellation of a perturbing dc Stark shift in strontium optical lattice clocks. *IEEE Trans. Ultrason. Ferroelectr. Freq. Control*, 59:411, 08 2012.

[90] Kurt Gibble. Scattering of cold atom coherences by hot atoms: Frequency shifts from background gas collisions. *Phys. Rev. Lett.*, 110:180802, 2013.

[91] B. X. R. Alves, Y. Foucault, G. Vallet, and J. Lodewyck. Background gas collision frequency shift on lattice-trapped strontium atoms. In *2019 Joint Conference of the IEEE International Frequency Control Symposium and European Frequency and Time Forum (EFTF/IFC)*, pages 1–2, Orlando, FL, USA, 2019. IEEE.

[92] Timur Abbasov, Konstantin Makarenko, Ivan Sherstov, Mikhail Axenov, Ilya Zalivako, Ilya Semerikov, Ksenia Khabarova, Nikolay Kolachevsky, Sergey Chepurov, Alexei Taichenachev, Sergey Bagaev, and Anton Tausenev. Compact transportable $^{171}Yb^{+}$ single-ion optical fully automated clock with $4.9 \cdot 10^{16}$ relative instability. arXiv:2010.15244 [physics.ins-det], Oct 2020. The paper has several serious issues

in the 'Results and discussion' part, and should be withdrawn for time until the issues are fully corrected, subm. to Photonics.

[93] Yao Huang, Huaqing Zhang, Baolin Zhang, Yanmei Hao, Hua Guan, Mengyan Zeng, Qunfeng Chen, Yige Lin, Yuzhuo Wang, Shiying Cao, Kun Liang, Fang Fang, Zhanjun Fang, Tianchu Li, and Kelin Gao. Geopotential measurement with a robust, transportable Ca^+ optical clock. *Phys. Rev. A*, 102:050802, Nov 2020.

[94] Noriaki Ohmae, Masao Takamoto, Yosuke Takahashi, Motohide Kokubun, Kuniya Araki, Andrew Hinton, Ichiro Ushijima, Takashi Muramatsu, Tetsuo Furumiya, Yuya Sakai, Naoji Moriya, Naohiro Kamiya, Kazuaki Fujii, Ryuya Muramatsu, Toshihiro Shiimado, and Hidetoshi Katori. Transportable strontium optical lattice clocks operated outside laboratory at the level of 10^{-18} uncertainty. *Adv. Quantum Technol.*, early view(n/a):2100015, 2021.

[95] Philippe Laurent, Didier Massonnet, Luigi Cacciapuoti, and Christophe Salomon. The ACES/PHARAO space mission. *C. R. Physique*, 16(5):540–552, 2015. The measurement of time / La mesure du temps.

[96] Stefano Origlia, Mysore Srinivas Pramod, Stephan Schiller, Yeshpal Singh, Kai Bongs, Roman Schwarz, Ali Al-Masoudi, Sören Dörscher, Sofia Herbers, Sebastian Häfner, Uwe Sterr, and Christian Lisdat. Towards an optical clock for space: Compact, high-performance optical lattice clock based on bosonic atoms. *Phys. Rev. A*, 98:053443, 2018.

[97] Sören Dörscher, Roman Schwarz, Ali Al-Masoudi, Stephan Falke, Uwe Sterr, and Christian Lisdat. Lattice-induced photon scattering in an optical lattice clock. *Phys. Rev. A*, 97:063419, Feb. 2018.

[98] B.H. Bransden and C.J. Joachain. *Physics of Atoms and Molecules*. Pearson Education. Prentice Hall, 2003.

[99] M. J. Martin, M. Bishof, M. D. Swallows, X. Zhang, C. Benko, J. von Stecher, A. V. Gorshkov, A. M. Rey, and Jun Ye. A quantum many-body spin system in an optical lattice clock. *Science*, 341:632–636, 2013.

[100] H. Uys, M. J. Biercuk, A. P. VanDevender, C. Ospelkaus, D. Meiser, R. Ozeri, and J. J. Bollinger. Decoherence due to elastic Rayleigh scattering. *Phys. Rev. Lett.*, 105:200401, 2010.

[101] Zeb Barber. *Ytterbium Optical Lattice Clock*. PhD thesis, University of Colorado, 2007.

[102] N. D. Lemke, A. D. Ludlow, Z. W. Barber, T. M. Fortier, S. A. Diddams, Y. Jiang, S. R. Jefferts, T. P. Heavner, T. E. Parker, and C. W. Oates. Spin-1/2 optical lattice clock. *Phys. Rev. Lett.*, 103:063001, 2009.

[103] Masami Yasuda and Hidetoshi Katori. Lifetime measurement of the $^3P_2$ metastable state of strontium atoms. *Phys. Rev. Lett.*, 92(15):153004, 2004.

[104] Neil Ashby, Thomas E. Parker, and Bijunath R. Patla. A null test of general relativity based on a long-term comparison of atomic transition frequencies. *Nature Physics*, 14:822 – 826, 2018.

[105] V. A. Dzuba and V. V. Flambaum. Limits on gravitational Einstein equivalence principle violation from monitoring atomic clock frequencies during a year. *Phys. Rev. D*, 95:015019, Jan 2017.

[106] W. F. McGrew, X. Zhang, H. Leopardi, R. J. Fasano, D. Nicolodi, K. Beloy, J. Yao, J. A. Sherman, S. A. Schäffer, J. Savory, R. C. Brown, S. Römisch, C. W. Oates, T. E. Parker, T. M. Fortier, and A. D. Ludlow. Towards the optical second: verifying optical clocks at the SI limit. *Optica*, 6(4):448–454, Apr 2019.

[107] Martin M. Boyd, Andrew D. Ludlow, Sebastian Blatt, Seth M. Foreman, Tetsuya Ido, Tanya Zelevinsky, and Jun Ye. ^{87}Sr lattice clock with inaccuracy below 10^{-15}. *Phys. Rev. Lett.*, 98:083002, 2007.

[108] X. Baillard, M. Fouché, R. Le Targat, P. G. Westergaard, A. Lecallier, F. Chapelet, M. Abgrall, G. D. Rovera, P. Laurent, P. Rosenbusch, S. Bize, G. Santarelli, A. Clairon, P. Lemonde, G. Grosche, B. Lipphardt, and H. Schnatz. An optical lattice clock with spin-polarized ^{87}Sr atoms. *Eur. Phys. J. D*, 48:11–17, 2008.

[109] Gretchen K. Campbell, Andrew D. Ludlow, Sebastian Blatt, Jan W. Thomsen, Michael J. Martin, Marcio H. G. de Miranda, Tanya Zelevinsky, Martin M. Boyd, Jun Ye, Scott A. Diddams, Thomas P. Heavner, Thomas E. Parker, and Steven R. Jefferts. The absolute frequency of the ^{87}Sr optical clock transition. *Metrologia*, 45:539–548, 2008.

[110] F.-L. Hong, M. Musha, M. Takamoto, H. Inaba, S. Yanagimachi, A. Takamizawa, K. Watabe, T. Ikegami, M. Imae, Y. Fujii, M. Amemiya, K. Nakagawa, K. Ueda, and H. Katori. Measuring the frequency of a Sr optical lattice clock using a 120 km coherent optical transfer. *Opt. Lett.*, 34:692–694, 2009.

[111] Atsushi Yamaguchi, Nobuyasu Shiga, Shigeo Nagano, Ying Li, Hiroshi Ishijima, Hidekazu Hachisu, Motohiro Kumagai, and Tetsuya Ido. Stability transfer between two clock lasers operating at different wavelengths for absolute frequency measurement of clock transition in ^{87}Sr. *Appl. Phys. Express*, 5:022701, 2012.

[112] Kensuke Matsubara, Hidekazu Hachisu, Ying Li, Shigeo Nagano, Clayton Locke, Asahiko Nohgami, Masatoshi Kajita, Kazuhiro Hayasaka, Tetsuya Ido, and Mizuhiko Hosokawa. Direct comparison of a Ca^+ single-ion clock against a Sr lattice clock to verify the absolute frequency measurement. *Opt. Express*, 20:22034, 2012.

[113] Daisuke Akamatsu, Hajime Inaba, Kazumoto Hosaka, Masami Yasuda, Atsushi Onae, Tomonari Suzuyama, Masaki Amemiya, and Feng-Lei Hong. Spectroscopy and frequency measurement of the ^{87}Sr clock transition by laser linewidth transfer using an optical frequency comb. *Appl. Phys. Express*, 7:012401, 2014.

[114] Hidekazu Hachisu and Tetsuya Ido. Intermittent optical frequency measurements to reduce the dead time uncertainty of frequency link. *Jpn. J. Appl. Phys.*, 54:112401, 2015.

[115] Yi-Ge Lin, Qiang Wang, Ye Li, Fei Meng, Bai-Ke Lin, Er-Jun Zang, Zhen Sun, Fang Fang, Tian-Chu Li, and Zhan-Jun Fang. First evaluation and frequency measurement of the strontium optical lattice clock at NIM. *Chin. Phys. Lett.*, 32:090601, 2015.

[116] Hidekazu Hachisu, Gérard Petit, and Tetsuya Ido. Absolute frequency measurement with uncertainty below 1×10^{-15} using International Atomic Time. *Appl. Phys. B*, 123:34, 2017.

[117] Takehiko Tanabe, Daisuke Akamatsu, Takumi Kobayashi, Akifumi Takamizawa, Shinya Yanagimachi, Takeshi Ikegami, Tomonari Suzuyama, Hajime Inaba, Sho Okubo, Masami Yasuda, Feng-Lei Hong, Atsushi Onae, and Kazumoto Hosaka. Improved frequency measurement of the $^1S_0$-$^3P_0$ clock transition in ^{87}Sr using a Cs fountain clock as a transfer oscillator. *J. Phys. Soc. Jpn.*, 84:115002, 2015.

[118] Jérôme Lodewyck, Sławomir Bilicki, Eva Bookjans, Jean-Luc Robyr, Chunyan Shi, Grégoire Vallet, Rodolphe Le Targat, Daniele Nicolodi, Yann Le Coq, Jocelyne Guéna, Michel Abgrall, Peter Rosenbusch, and Sébastien Bize. Optical to microwave clock frequency ratios with a nearly continuous strontium optical lattice clock. *Metrologia*, 53(4):1123, 2016.

[119] Hidekazu Hachisu, Gérard Petit, Fumimaru Nakagawa, Yuko Hanado, and Tetsuya Ido. SI-traceable measurement of an optical frequency at the low 10^{-16} level without a local primary standard. *Opt. Express*, 25(8):8511–8523, Apr 2017.

[120] Nils Nemitz, Tadahiro Gotoh, Fumimaru Nakagawa, Hiroyuki Ito, Yuko Hanado, Tetsuya Ido, and Hidekazu Hachisu. Absolute frequency of ^{87}Sr at 1.8×10^{-16} uncertainty by reference to remote Primary Frequency Standards. *Metrologia*, Oct 2020. Accepted Manuscript.

[121] Richard Hobson, William Bowden, Alissa Silva, Charles F. A. Baynham, Helen S. Margolis, Patrick E. G. Baird, Patrick Gill, and Ian R. Hill. A strontium optical lattice clock with 1×10^{-17} uncertainty and measurement of its absolute frequency. *Metrologia*, 57:065026, 2020.

[122] Fritz Riehle, Patrick Gill, Felicitas Arias, and Lennart Robertsson. The CIPM list of recommended frequency standard values: guidelines and procedures. *Metrologia*, 55(2):188–200, 2018.

[123] Recommendation CCTF1 (2004): Secondary representations of the second, report of the 16th meeting of the CCTF (April 2004), 2004. www.bipm.org/utils/common/pdf/CCTF16.pdf.

[124] R. Lange, N. Huntemann, J. M. Rahm, C. Sanner, H. Shao, B. Lipphardt, Chr. Tamm, S. Weyers, and E. Peik. Improved limits for violations of local position invariance from atomic clock comparisons. *Phys. Rev. Lett.*, 126:011102, Jan 2021.

[125] Masao Takamoto, Ichiro Ushijima, Noriaki Ohmae, Toshihiro Yahagi, Kensuke Kokado, Hisaaki Shinkai, and Hidetoshi Katori. Test of general relativity by a pair of transportable optical lattice clocks. *Nature Photonics*, 14:411–415, 2020.

[126] C. Lisdat, G. Grosche, N. Quintin, C. Shi, S.M.F. Raupach, C. Grebing, D. Nicolodi, F. Stefani, A. Al-Masoudi, S. Dörscher, S. Häfner, J.-L. Robyr, N. Chiodo, S. Bilicki, E. Bookjans, A. Koczwara, S. Koke, A. Kuhl, F. Wiotte, F. Meynadier, E. Camisard, M. Abgrall, M. Lours, T. Legero, H. Schnatz, U. Sterr, H. Denker, C. Chardonnet, Y. Le Coq, G. Santarelli, A. Amy-Klein, R. Le Targat, J. Lodewyck, O. Lopez, and P.-E. Pottie. A clock network for geodesy and fundamental science. *Nature Commun.*, 7:12443, 2016.

[127] R. M. Godun, P. B. R. Nisbet-Jones, J. M. Jones, S. A. King, L. A. M. Johnson, H. S. Margolis, K. Szymaniec, S. N. Lea, K. Bongs, and P. Gill. Frequency ratio of two optical clock transitions in $^{171}Yb^{+}$ and constraints on the time-variation of fundamental constants. *Phys. Rev. Lett.*, 113:210801, Nov 2014.

[128] Noriaki Ohmae, Filippo Bregolin, Nils Nemitz, and Hidetoshi Katori. Direct measurement of the frequency ratio for Hg and Yb optical lattice clocks and closure of the Hg/Yb/Sr loop. *Opt. Express*, 28(10):15112–15121, May 2020.

[129] Masao Takamoto, Ichiro Ushijima, Manoj Das, Nils Nemitz, Takuya Ohkubo, Kazuhiro Yamanaka, Noriaki Ohmae, Tetsushi Takano, Tomoya Akatsuka, Atsushi Yamaguchi, and Hidetoshi Katori. Frequency ratios of Sr, Yb, and Hg based optical lattice clocks and their applications. *C. R. Physique*, 16(0):489–498, 2015. Special Issue: The measurement of time / La mesure du temps.

[130] Kazuhiro Yamanaka, Noriaki Ohmae, Ichiro Ushijima, Masao Takamoto, and Hidetoshi Katori. Frequency ratio of ^{199}Hg and ^{87}Sr optical lattice clocks beyond the SI limit. *Phys. Rev. Lett.*, 114:230801, Jun 2015.

[131] Nils Nemitz, Takuya Ohkubo, Masao Takamoto, Ichiro Ushijima, Manoj Das, Noriaki Ohmae, and Hidetoshi Katori. Frequency ratio of Yb and Sr clocks with 5×10^{-17} uncertainty at 150 s averaging time. *Nature Photonics*, 10:258–261, 2016.

[132] Kyle Beloy, Martha I. Bodine, Tobias Bothwell, Samuel M. Brewer, Sarah L. Bromley, Jwo-Sy Chen, Jean-Daniel Deschênes, Scott A. Diddams, Robert J. Fasano, Tara M. Fortier, Youssef S. Hassan, David B. Hume, Dhruv Kedar, Colin J. Kennedy, Isaac Khader, Amanda Koepke, David R. Leibrandt, Holly Leopardi, Andrew D. Ludlow, William F. McGrew, William R. Milner, Nathan R. Newbury, Daniele Nicolodi, Eric Oelker, Thomas E. Parker, John M. Robinson, Stefania Romisch, Stefan A. Schäffer, Jeffrey A. Sherman, Laura C. Sinclair, Lindsay Sonderhouse, William C. Swann, Jian Yao, Jun Ye, Xiaogang Zhang, and Boulder Atomic

Clock Optical Network (BACON) Collaboration*. Frequency ratio measurements at 18-digit accuracy using an optical clock network. *Nature*, 591(7851):564–569, 2021.

[133] L. Essen and J. V. L. Parry. An atomic standard of frequency and time interval: A caesium resonator. *Nature*, 176:280–282, 1955.

[134] A. Clairon, C. Salomon, S. Guellati, and W. D. Phillips. Ramsey resonance in a Zacharias fountain. *Europhys. Lett.*, 16:165–170, 1991.

[135] A. Clairon, P. Laurent, G. Santarelli, S. Ghezali, S.N. Lea, and M. Bahoura. A cesium fountain frequency standard: preliminary results. *IEEE Trans. Instrum. Meas.*, 44:128–131, 1995.

[136] A. Bauch, B. Fischer, T. Heindorff, and R. Schröder. Performance of the PTB reconstructed primary clock CS1 and an estimate of its current uncertainty. *Metrologia*, 35:829–845, 1998.

[137] S. R. Jefferts, T. P. Heavner, J. Shirley, and T. E. Parker. Systematic frequency shifts and quantum projection noise in NIST-F1. In P. Gill, editor, *Frequency Standards and Metrology, Proceedings of the Sixth Symposium*, pages 72–79, Singapore, 2002. World Scientific.

[138] S. Weyers, U. Hübner, R. Schröder, Chr. Tamm, and A. Bauch. Uncertainty evaluation of the atomic caesium fountain CSF1 of the PTB. *Metrologia*, 38:343–352, 2001.

[139] Andreas Bauch. Caesium atomic clocks: Function, performance and applications. *Meas. Sci. Technol.*, 14:1159–1173, 2003.

[140] S. Weyers, A. Bauch, R. Schröder, and Chr. Tamm. The atomic caesium fountain CSF1 of PTB. In P. Gill, editor, *Frequency Standards and Metrology, Proceedings of the Sixth Symposium*, pages 64–71, Singapore, 2002. World Scientific.

[141] S. R. Jefferts, J. H. Shirley, N. Ashby, E. A. Burt, and G. J. Dick. Power dependence of distributed cavity phase-induced frequency biases in atomic fountain frequency standards. *IEEE Trans. Ultrason. Ferroelectr. Freq. Control*, 52(12):2314 – 2321, 2005.

[142] T E Parker, S R Jefferts, T P Heavner, and E A Donley. Operation of the NIST-F1 caesium fountain primary frequency standard with a maser ensemble, including the impact of frequency transfer noise. *Metrologia*, 42(5):423–430, 2005.

[143] Thomas E Parker. Long-term comparison of caesium fountain primary frequency standards. *Metrologia*, 47(1):1–10, 2010.

[144] F. Levi, D. Calonico, L. Lorini, and A. Godone. IEN-CsF1 primary frequency standard at INRIM: accuracy evaluation and TAI calibrations. *Metrologia*, 43(6):545–555, 2006.

[145] T. P. Heavner, S. R. Jefferts, E. A. Donley, J. H. Shirley, and T. E. Parker. NIST-F1: recent improvements and accuracy evaluations. *Metrologia*, 42:411–422, 2005.

[146] Krzysztof Szymaniec, Sang Eon Park, Giuseppe Marra, and Witold Chałupczak. First accuracy evaluation of the NPL-CsF2 primary frequency standard. *Metrologia*, 47:363, 2010.

[147] S. Weyers, V. Gerginov, N. Nemitz, R. Li, and K. Gibble. Distributed cavity phase frequency shifts of the caesium fountain PTB-CSF2. *Metrologia*, 49:82–87, 2012.

[148] H. Schnatz, B. Lipphardt, J. Helmcke, F. Riehle, and G. Zinner. First phase-coherent frequency measurement of visible radiation. *Phys. Rev. Lett.*, 76:18–21, 1996.

[149] Th. Udem, A. Huber, B. Gross, J. Reichert, M. Prevedelli, M. Weitz, and T. W. Hänsch. Phase-coherent measurement of the hydrogen 1S–2S transition frequency with an optical frequency interval divider chain. *Phys. Rev. Lett.*, 79:2646–2649, 1997.

[150] M. Niering, R. Holzwarth, J. Reichert, P. Pokasov, Th. Udem, M. Weitz, T. W. Hänsch, P. Lemonde, G. Santarelli, M. Abgrall, P. Laurent, C. Salomon, and A. Clairon. Measurement of the hydrogen 1S – 2S transition frequency by phase coherent comparison with a microwave cesium fountain clock. *Phys. Rev. Lett.*, 84:5496–5499, 2000.

[151] Leo Hollberg, Chris W. Oates, E. Anne Curtis, Eugene N. Ivanov, Scott A. Diddams, Thomas Udem, Hugh G. Robinson, James C. Bergquist, Robert J. Rafac, Wayne M. Itano, Robert E. Drullinger, and D. J. Wineland. Optical frequency standards and measurements. *IEEE J. Quantum Electron.*, 37:1502–1513, 2001.

[152] S. Bize, S. A. Diddams, U. Tanaka, C. E. Tanner, W. H. Oskay, R. E. Drullinger, T. E. Parker, T. P. Heavner, S. R. Jefferts, L. Hollberg, W. M. Itano, and J. C. Bergquist. Testing the stability of fundamental constants with the $^{199}Hg^{+}$ single-ion optical clock. *Phys. Rev. Lett.*, 90:150802, 2003.

[153] H. S. Margolis, G. P. Barwood, G. Huang, H. A. Klein, S. N. Lea, K. Szymaniec, and P. Gill. Hertz-level measurement of the optical clock frequency in a single $^{88}Sr^{+}$ ion. *Science*, 306:1355–1358, 2004.

[154] W. H. Oskay, S. A. Diddams, E. A. Donley, T. M. Fortier, T. P. Heavner, L. Hollberg, W. M. Itano, S. R. Jefferts, M. J. Delaney, K. Kim, F. Levi, T. E. Parker, and J. C. Bergquist. Single-atom optical clock with high accuracy. *Phys. Rev. Lett.*, 97:020801, 2006.

[155] A. D. Ludlow, T. Zelevinsky, G. K. Campbell, S. Blatt, M. M. Boyd, M. H. G. de Miranda, M. J. Martin, J. W. Thomsen, S. M. Foreman, Jun Ye, T. M. Fortier, J. E. Stalnaker, S. A. Diddams, Y. Le Coq, Z. W. Barber, N. Poli, N. D. Lemke, K. M. Beck, and C. W. Oates. Sr lattice clock at 1×10^{-16} fractional uncertainty by remote optical evaluation with a Ca clock. *Science*, 319:1805–1808, 2008.

[156] Chr. Tamm, S. Weyers, B. Lipphardt, and E. Peik. Stray-field induced quadrupole shift and absolute frequency of the 688 THz $^{171}Yb^{+}$ single-ion optical frequency standard. *Phys. Rev. A*, 80:043403, 2009.

[157] C. W. Chou, D. B. Hume, J. C. J. Koelemeij, D. J. Wineland, and T. Rosenband. Frequency comparison of two high-accuracy Al^{+} optical clocks. *Phys. Rev. Lett.*, 104:070802, 2010.

[158] David Hunger, Stephan Camerer, Maria Korppi, Andreas Jöckel, Theodor W. Hänsch, and Philipp Treutlein. Coupling ultracold atoms to mechanical oscillators. arXiv:1103.1820v1 [quant-ph], Mar. 2011. Preprint submitted to Comptes Rendus.

[159] Alan A. Madej, Pierre Dubé, Zichao Zhu, John E. Bernard, and Marina Gertsvolf. $^{88}Sr^{+}$ 445-THz single ion reference at the 10^{-17} level via control and cancellation of systematic uncertainties and its measurement against the SI second. *Phys. Rev. Lett.*, 109:203002, Nov 2012.

[160] N. Huntemann, C. Sanner, B. Lipphardt, Chr. Tamm, and E. Peik. Single-ion atomic clock with 3×10^{-18} systematic uncertainty. *Phys. Rev. Lett.*, 116:063001, Feb 2016.

[161] R. Tyumenev, M. Favier, S. Bilicki, E. Bookjans, R. Le Targat, J. Lodewyck, D Nicolodi, Y. Le Coq, M. Abgrall, J. Guéna, L. De Sarlo, and S. Bize. Comparing a mercury optical lattice clock with microwave and optical frequency standards. *New J. Phys.*, 18:113002, 2016.

[162] W. F. McGrew, X. Zhang, R. J. Fasano, S. A. Schäffer, K. Beloy, D. Nicolodi, R. C. Brown, N. Hinkley, G. Milan, M. Schioppo, T. H. Yoon, and A. D. Ludlow. Atomic clock performance beyond the geodetic limit. *Nature*, 564:87–90, Nov. 2018.

[163] S. M. Brewer, J.-S. Chen, A. M. Hankin, E. R. Clements, C. W. Chou, D. J. Wineland, D. B. Hume, and D. R. Leibrandt. $^{27}Al^{+}$ quantum-logic clock with a systematic uncertainty below 10^{-18}. *Phys. Rev. Lett.*, 123:033201, 2019.

[164] Yao Huang, Baolin Zhang, Mengyan Zeng, Yanmei Hao, Huaqing Zhang, Hua Guan, Zheng Chen, Miao Wang, and Kelin Gao. A liquid nitrogen-cooled Ca^{+} optical clock with systematic uncertainty of 3×10^{-18}. arXiv:2103.08913 [physics.atom-ph], Mar 2021.

[165] Erik Benkler, Burghard Lipphardt, Thomas Puppe, Rafał Wilk, Felix Rohde, and Uwe Sterr. End-to-end topology for fiber comb based optical frequency transfer at the 10^{-21} level: erratum. *Opt. Express*, 28(10):15023–15024, 2020.

[166] D.B. Sullivan, D.W. Allan, D.A. Howe, and F.L. Walls. Characterization of clocks and oscillators. NIST tech. note 1337, NIST, U.S Department of Commerce, National Institute of Standards and Technology, March 1990. online available at http://tf.nist.gov/cgi-bin/showpubs.pl.

[167] J. Fischer, M. de Podesta, K. D. Hill, M. Moldover, L. Pitre, R. Rusby, P. Steur, O. Tamura, R. White, and L. Wolber. Present estimates of the differences between thermodynamic temperatures and the ITS-90. *Int. J. Thermophys.*, 32:12–25, 2011.